Polymer Additive Engineering of Organolead Halide Perovskites: Effect on Device Characteristics and Scalable Manufacturing

by

Avi Mathur

A thesis

presented to the University of Waterloo

in fulfillment of the

thesis requirement for the degree of

Doctor of Philosophy

in

Chemistry (Nanotechnology)

Waterloo, Ontario, Canada, 2022

Examining Committee Membership

The following served on the Examining Committee for this thesis. The decision of the Examining Committee is by majority vote.

External Examiner	Sylvain G. Cloutier Professor Department of Electrical Engineering École de Technologie Supérieure, Canada
Supervisor	Vivek Maheshwari Associate Professor Department of Chemistry University of Waterloo, Canada
Internal Members	Kam Tong Leung Professor Department of Chemistry University of Waterloo, Canada
	Derek Schipper Associate Professor Department of Chemistry University of Waterloo, Canada
Internal-external Member	Kevin P. Musselman Associate Professor Department of Mechanical and Mechatronics Engineering, University of Waterloo, Canada

Author's Declaration

This thesis consists of material all of which I authored or co-authored: see Statement of Contributions included in the thesis. This is a true copy of the thesis, including any required final revisions, as accepted by my examiners.

I understand that my thesis may be made electronically available to the public.

Statement of Contributions

This thesis consists of material from a collection of several journal articles that I have authored or co-authored and are either published or intended for publication, some of which resulted from collaboration with my colleagues in the Maheshwari group.

- Part of the content in Chapter 1 has been published in

Mathur, A., Fan, H., & Maheshwari, V. (2021). Organolead halide perovskites beyond solar cells: self-powered devices and the associated progress and challenges. *Mater. Adv.*, *2*(16), 5274-5299.

A. Mathur and H. Fan contributed equally to this work. A. Mathur and V. Maheshwari conceptualized the idea. A. Mathur and H. Fan carried out the investigation and performed the writing of the original draft of this review article. V. Maheshwari was responsible for the funding acquisition, providing resources, reviewing, and editing the original draft, and supervision.

- Part of the content in Chapter 2 has been published in

Mathur, A., & Maheshwari, V. (2022). Carbon monoxide induced self-doping in methylammonium lead iodide films and associated long-term degradation effects. *J. Mater. Chem. C*, 10(19), 7485-7493.

A. Mathur conducted the experiments including device fabrication, characterization, testing, and analysis of the results, and wrote the original draft of the manuscript. V. Maheshwari acquired funding, provided resources, reviewed, and edited the original draft, and supervised.

- Part of the content in Chapter 4 has been published in

Mathur, A., Li, A., & Maheshwari, V. (2021). Nanoscale Architecture of Polymer–Organolead Halide Perovskite Films and the Effect of Polymer Chain Mobility on Device Performance. *J. Phys. Chem. Lett*., 12(5), 1481-1489.

A. Mathur led experiments including device fabrication, characterization, and testing. A. Li assisted in device fabrication and testing. A. Mathur further analyzed and discussed the results and wrote the original draft of this article. V. Maheshwari was responsible for the funding acquisition, providing resources, reviewing, and editing the original draft, and supervision.

- Part of the content in Chapter 5 has been published in

Mathur, A., Fan, H., & Maheshwari, V. (2021). Soft Polymer-Organolead Halide Perovskite Films for Highly Stretchable and Durable Photodetectors with Pt-Au Nanochain-Based Electrodes. *ACS Appl. Mater. Interfaces*, 13(49), 58956–58965.

A. Mathur And H. Fan contributed equally to this work. A. Mathur and V. Maheshwari conceptualized the idea. A. Mathur and H. Fan conducted all the experiments, characterization, and device testing. All authors analyzed and discussed the results and contributed to the writing of the original draft of this article. V. Maheshwari was further responsible for the funding acquisition, providing resources, reviewing, and editing the original draft, and supervision.

- The content in Chapters 3 and 6 has not been published yet. However, it is in a near-verbatim state of what is intended for submission.

Abstract

Within the last decade, organolead halide perovskites such as methylammonium lead iodide ($MAPbI_3$), have established themselves as a promising material choice for developing highly efficient and cost-effective photosensitive devices ranging from solar cells to photodetectors, display devices, light-emitting diodes (LEDs), self-powered devices, sensors and beyond. Despite exhibiting impeccable electro-optical properties and ease of solution processibility, the instability of perovskite under an ambient atmosphere hinders their commercial viability. The key issue lies in the degradation of the perovskite material in presence of light, O_2, moisture, and high temperature, along with the migration of the constituent ions (especially MA^+ and I^- owing to their low activation energy) under an electrical field.

In addition to abundant gases such as oxygen, nitrogen, and carbon dioxide, the interaction with omnipresent gas such as carbon monoxide (CO) at the perovskite interface can critically affect the electro-optical and mechanical properties and stability of the resultant perovskite devices. It is observed that exposure to the CO environment can displace adsorbed O_2 and leads to a lowering of work function and induces self-doping in the $MAPbI_3$ film. Interaction with CO at the perovskite film interface leads to layer-by-layer depletion of the organic moiety leaving behind PbI_2 and this also softens the film over time. While long-duration exposure is detrimental to the electro-optical properties of the perovskite film, short exposure to the CO causes a 122% enhancement in the self-powered capacity of these films, which has significant implications for their applications in photodetectors, electrochemical cells, and sensors.

To address these instability issues, several strategies are being actively researched. These involve compositional engineering, the addition of interfacial layers, encapsulation of the entire device, or a combination of multiple of these. These strategies however mandate additional resources, and an inert atmosphere and may lead to an undesirable blue shift of the absorption spectrum hampering the feasibility of the device fabrication. Further, these fail at alleviating the internal degradation of perovskite caused by ion migration.

The stability issues in perovskites can be instead addressed by material engineering strategy, based on the specific chemical interaction of polymer additive with the perovskite precursors. Inspired by the direct interaction between organic molecules and inorganic moieties in biological and bio-inspired systems where the addition of organic molecules (primarily amino acids, DNA, and RNA) may alter

the crystallization kinetics, and crystal phase switching & orientation, morphology, and other structural properties of the inorganic-organic composite, lead iodide (PbI_2) facilitated in-situ cross-linking of PS chains in the perovskite precursor solution, is presented. The cation-π interaction between the MA^+ and long-order PS molecules at the grain boundaries and at interfaces facilitates the formation of a three-dimensional molecular network in the $MAPbI_3$ film with uniform morphology, enhanced grain size, mobility, and carrier lifetime with reduced ion migration, charge recombination, and dark currents.

Different polymer additives may inherently differ not only in terms of their affinity for water and conductivity but also in the interaction mechanism with the perovskite precursors owing to the difference in polarity. Hence, to understand which characteristics of the polymer might be more important for achieving stable perovskite-polymer composite films without compromising the device performance, the strong interaction capabilities of the hydrophilic polar polyethylene glycol (PEG) and hydrophobic non-polar PS polymers in a PEG-PS block co-polymer system have been utilized. Such an approach provides a better understanding of the effective contribution of each polymer counterpart when mixed alongside perovskite precursors. It is realized that while the presence of PS enhances the average grain size, the presence of merely PEG as an additive leads to enhanced heterogeneous nucleation which increases the density of grain boundaries and trap sites within the perovskite films and proves insufficient to reduce ionic conductivity. Further, the fabrication of ambient atmosphere stable perovskite films mandates the presence of hydrophobic PS chains.

It is observed that the integration of PS chains with organolead halide perovskite films, leading to enhanced stability and electro-optical performance, is critically affected by the molecular weight of chains. The molecular weight determines the mobility and volume of the chains, which affects the crystallization kinetics and, hence, perovskite grain size. The insulating nature of the PS chains is another critical factor that affects both ion migration and the conduction of electronic charges. The combined effect of these factors leads to optimal performance with the use of medium-length chains. A simple model integrating the two effects accurately fits the response of the polymer–perovskite composite. Further characterization results show that the polymer–perovskite films have a three-layer architecture consisting of nanoscale polymer-rich top and bottom layers. These combined results show that the optimization of performance in polymer–perovskite devices depends critically on the size of the chains due to their multiple effects on the perovskite matrix.

The rigid and brittle nature of $MAPbI_3$ polycrystalline films limits their application in stretchable devices due to rapid deterioration in performance on mechanical cycling. By incorporation of PS chains in the $MAPbI_3$ films, the mechanical modulus and the viscoelastic nature of the films are altered. Combining this with flexible nanochain electrodes, highly stretchable and stable perovskite devices have been fabricated. The resultant PS-$MAPbI_3$ photodetector exhibits ultralow dark currents ($\sim 10^{-11}$ A) and high light switching ratios ($\sim 10^3$) and maintains 75% of performance after 30 days. The viscoelastic nature and lower modulus of the polymer improve the energy dissipation in the polymer-$MAPbI_3$ devices; as a result, they maintain 52% of the device performance after 10000 stretching cycles at 50% strain. The difference in the mechanical behavior is observed in the failure mode of the two films. While rapid catastrophic cracking is observed in $MAPbI_3$ films, the intensity and size of such crack formation are highly limited in polymer-$MAPbI_3$ films, which prevents their failure.

The PS integration strategy provides a route for scalable manufacturing of perovskite films by utilizing the room-temperature blade coating technique. This serves the dual purpose of addressing the challenges of developing large area perovskite film-based devices which can survive in the ambient atmosphere without compromising on efficiency. It can thus pave the way for the cost-effective commercialization of perovskite-based electro-optical devices with a larger active area.

Overall, the findings of this research work highlight the ability to tune the characteristics of the perovskite-based photosensitive device and extend them beyond rigid substrates to realize stretchable devices by a single-step method of integrating a commodity scale polymer in the perovskite films. This work also provides a deep insight into the improved stability and architecture of perovskite-polymer hybrid films which will be of significant interest to the research community. Such a facile polymer additive strategy combined with an ambient atmosphere compatible blade coating technique will pave the way for the development of polymer-perovskite hybrid assembly for long-term device applications and their scalable manufacturing.

Acknowledgments

First, I would like to express my sincere gratitude to my advisor, Professor Vivek Maheshwari, for allowing me to conduct my doctoral research under his supervision and gain valuable experience at the University of Waterloo. I am deeply grateful to him for giving me freedom in choosing my Ph.D. research topic and for showing trust in my ability to work independently. His unbounded commitment and overwhelming support have enabled me to complete my Ph.D. thesis. I profusely thank him for his excellent guidance, encouragement, and endurance throughout my graduate study. His amicable nature will always be a pleasant memory in my life.

Besides my advisor, I would like to thank the rest of my thesis committee: Professor Kam Tong Leung, Professor Derek Schipper, and Professor Kevin P. Musselman for their encouragement, insightful comments, feedback, and excellent discussions during my doctoral research.

I am grateful to my fellow lab mates: Dr. Rohit Saraf, Dr. Hua Fan, Saikiran Khamgaonkar, and Mohamed Okasha for stimulating discussions and their continuous support. Special thanks to Alexander Li for assisting me in multiple research projects. I would also like to thank all my friends outside the University for making my stay in Waterloo a memorable one. I would like to thank Catherine Van Esch and Kim Rawson for all their administrative assistance and kindness.

I appreciate Dr. Joseph P. Thomas, Dr. Nina Heinig, Dr. Nathan Nelson-Fitzpatrick, and Dr. Sandra Gibson for helping me with materials characterization. This work would have not been possible without the utilization of the characterization facilities at WATLab and QNFCF. Special thanks to Vladimir Miskovic and Sarah Mark for helping me with the procurement of lab supplies, whenever in need. It would be unfair to not thank Hiruy Haile and Chris Kleven for their invaluable support throughout my Ph.D. journey.

Last but not the least, I owe more than thanks to my family members for their blessings, moral support, encouragement, and motivation.

Dedication

This thesis work is dedicated to my parents, Vinay Mathur and Shashi Kala Mathur, who have been a constant source of support and encouragement throughout my life and have always loved me unconditionally. Seeing them work hard to fulfill my career aspirations has served as my biggest motivation throughout my doctoral research endeavor.

Table of Contents

List of Figures

List of Tables

List of Abbreviations

AC	Alternating current
AFM	Atomic force microscope
AM	Air mass
AM-KPFM	Amplitude modulated kelvin potential force microscopy
BCP	Bathocuproine
CIGS	Copper indium gallium selenide
CO	Carbon monoxide
CPTA	2-(4-chlorophenylthio)triethylamine hydrochloride
DMF	N, N-dimethylformamide
DMSO	Dimethyl sulfoxide
DMT	Derjaguin-Muller-Toropov
DNA	Deoxyribonucleic acid
E_A	Activation energy
E_C	Critical field for tunneling
EDX	Energy-dispersive X-ray spectroscopy
EPA	Environmental protection agency
FA	Formamidinium
FE	Field emission
FF	Fill factor
FWHM	Full width at half maximum
GIXRD	Grazing incidence
HOPG	Highly oriented pyrolytic graphite
HRTEM	High-resolution transmission electron microscopy
ICSD	Inorganic crystal structure database
IEC	International Electrotechnical Commission
I_{sc}	Short-circuit current

ITO	Indium tin oxide
Jsc	Short-circuit current density
K_{IC}	Fracture toughness
KPFM	Kelvin potential force microscopy
LCOE	Levelized Cost of Energy
LED	Light-emitting diodes
Li-TSFI	Lithium bis(trifluoromethanesulfonyl)imide
MA	Methylammonium
MAI	Methylammonium iodide
$MAPbI_3$	Methylammonium lead iodide
NMP	N-methyl-2- pyrrolidone
NREL	National Renewable Energy Laboratory
PAA	Polyacrylic acid
PAN	Polyacrylonitrile
PCBM	Phenyl-C_{61}-butyric acid methyl ester
PCE	Power conversion efficiency
PDI	Polydispersity index
PDMS	Polydimethylsiloxane
PEDOT:PSS	Poly(3,4-ethylenedioxythiophene)-poly(styrene sulfonate)
PEG	Polyethylene glycol
PEI	Polyethylenimine
PET	Polyethylene terephthalate
PF-QNM	Peakforce quantum nanomechanical
PMMA	Polymethyl methacrylate
PS	Polystyrene
PTAA	Poly(triarylamine)
PVP	Polyvinylpyrrolidone
QNFCF	Quantum-Nano Fabrication and Characterization Facility
RH	Relative humidity

RNA	Ribonucleic acid
SEM	Scanning electron microscopy
spiro-MeOTAD	2,2',7,7'-tetrakis(N,N-di(4-methoxyphenylamino)-9,9'-
TMTA	Trimethylolpropane triacrylate
ToF-SIMS	Time of flight secondary ion mass spectroscopy
UGA	Universal gas analyzer
UV	Ultraviolet
V_{CPD}	Contact potential difference
VHB	Very high bonding
V_{OC}	Open-circuit voltage
WHO	World Health Organization
XRD	X-ray diffraction

Chapter 1
Introduction

Proper tuning of composition yielding a wide variation in electronic properties including capacitive, ferroelectric, piezoelectric, superconductive, metallic, catalytic, and magnetic properties has been the primary reason for perovskite compounds being a widely researched class of chemicals. The word 'perovskite' is derived from the mineral form of $CaTiO_3$ and is named after the Russian mineralogist Lev Perovski in honor of his contribution towards the structural characterization of the calcium titanium mineral, while its discovery in the Ural Mountains of Russia in 1839 is accredited to Gustav Rose.[1] In the context of the stoichiometry of the ionic composition in the parent mineral form, the formula of ABX_3 is generally deployed to refer to the family of materials expressing a three-dimensional (3-D) crystal structure similar to $CaTiO_3$, where A and B sites represent cations of dissimilar sizes while the X site is occupied by counterbalancing anionic species. The A, B, and X ions exhibit an overall valency ratio of 1:2:1. In a typical perovskite cubic unit cell composed of five atoms, the A cation occupies a 12-fold central coordination site and B cation forms 6 coordination fold while the BX_6 (i.e., BX_3) forms corner-sharing octahedra.[2] Considering the involved atoms as closely packed rigid spheres, the stability of the perovskite crystal structure at room temperature largely depends upon the sizes of the spheres and is dictated by Goldschmidt's Tolerance Factor concept (Formula 1.1):

$$t = \frac{R_B + R_X}{\sqrt{2}(R_A + R_X)} \tag{1.1}$$

where R_A, R_B, and R_X represent the empirical ionic radii of A, B, and X site elements, respectively. Mostly, the perovskite systems where the tolerance factor satisfies $t \approx 1$ exhibit cubic crystal structure, while the crystal framework exhibiting variation in 't' as $0.813 \leq t \leq 1.107$ show distortion from the ideal cubic phase.[3] It is due to these distortions that the perovskite systems vary largely in terms of their intrinsic physical properties, particularly the electronic, magnetic, and dielectric properties, and account for varied applications of the respective materials.

1.1 Organic-inorganic halide perovskites

Within the formal stoichiometry of ABX_3, charge balancing ($q^A + q^B + 3q^X = 0$) in the perovskites can be achieved in a variety of ways. For metal oxide perovskites (ABO_3), the formal oxidation states of the two metals must sum to six ($q^A + q^B = -3q^O = 6$). Hence, I-V-O_3, II-IV-O_3 and III-III-O_3 perovskites

are the common viable metal oxide systems. On the other hand, in the case of halide perovskites, the oxidation states of the cations should instead sum up to three ($q^A + q^B = -3q^X = 3$) leaving the only possible ternary combination as I-II-X_3.[4] In a typical case of organic-inorganic hybrid perovskites, the A site is occupied by a monovalent organic species while the B and X sites are occupied by a divalent metal (mostly IVA group elements) and halide, respectively.

The differences in the relative size of the ionic species forming the perovskite may result in the exhibition of different dimensionalities. For instance, when the A site is occupied by monovalent cations, such as Rb^+, Cs^+, $CH_3NH_3^+$ and $HC(NH_2)_2^+$, it acquires a 3-D framework, whereas in the case of a larger cation such as $CH_3CH_2NH_3^+$, two-dimensional (2-D) or one-dimensional (1-D) structures are obtained with relatively larger energy band gap (2.2eV for $CH_3CH_2NH_3^+$). Thus, it has been reported that an excessively large A cation is detrimental to the 3D framework, corresponding to $t << 1$ and reduced dimensionality.[5] It has been reported that the central A moiety does not influence the electronic properties of the perovskite compounds but may adversely affect the symmetry by distorting the B-X bond. Further, external factors such as heat/temperature variation, oxidizing/reducing environment, moisture, etc. may cause compositional changes that contribute to the distortion of the perovskite symmetry.[5] Hence, overall, external effects and compositional ionic species largely determine the symmetry, and the properties of the perovskite material could be specifically tailored depending upon intended applications.

1.2 Methylammonium lead iodide ($MAPbI_3$)

Among the organic-inorganic halide perovskite systems, methylammonium lead iodide ($MAPbI_3$) serves as the most widely researched and prototypical example, owing to its favorable tunable band gap and optoelectronic properties making it suitable for photovoltaic applications. In 1978, Weber was a pioneer in reporting the organic group, methylammonium (MA), at the A site and the Sn-based trihalide perovskite family $CH_3NH_3SnBr_xI_{3-x}$ ($x = 0$-3) possessing a cubic structure.[6] Soon afterward, he reported the Pb-based trihalide perovskites, which revolutionized, in particular, photovoltaics and solar cell applications.[7] Miyasaka et. al. were the first ones to utilize $CH_3NH_3PbI_3$ as a photosensitive material in a dye-sensitized solar cell demonstrating 3.8% efficiency. The efficiency of the same configuration of this perovskite sensitized solar cell was further increased to 6.5% by Park and his co-workers. However, the liquid-based perovskite solar cell did not attract much attention owing to the instant dissolution of the perovskite ionic crystal in the polar liquid electrolyte, which led to rapid degradation of device

performance. In 2012, Park et. al. substituted the liquid electrolyte with a solid-hole conductor material to address this issue and were able to enhance the efficiency to 9.7%. Since then, the organolead halide perovskites and $MAPbI_3$, in particular, have attracted enormous worldwide attention and prompted a dramatic increase in the power conversion efficiency (PCE) of perovskite-based solar cells to 25.2%. These are now being applied in other optoelectronic devices such as sensors, photodetectors, lasers, displays, light-emitting diodes (LEDs), field-effect transistors, and resistive switching memory devices.

The small size of methylammonium cation (MA^+) accounts for the formation of a stable tetragonal phase of $MAPbI_3$ at room temperature. The tetragonal phase exhibits a bandgap of 1.51—1.55 eV corresponding to an 820 nm absorption edge, and thus exceeds the optimal 1.1—1.4 eV band gap range governed by the Shockley-Queisser limit for a single junction solar cell.[8, 9] However, it forms a 3-D framework and is devoid of distortion in the A-X interaction, as otherwise observed in systems involving ethyl ammonium ($CH_3CH_2NH_3^+$) and formamidinium cation ($HC(NH_2)_2^+$). Moreover, using $t = 1$ as the tolerance factor, and more importantly having the largest values for R_B and R_X (i.e., Shannon ionic radii R_{Pb} = 1.19 Å and R_I = 2.20 Å), the limit on R_A is found to be approximately 2.6 Å for traditional BX^{3-} frameworks with B being the divalent metal and X representing the halogen.[10] Assuming the non-spherical symmetric organic cations are free to rotate around their centers of mass, the effective ionic radius of the MA cation (2.17 Å) satisfies the requisites for forming a stable $MAPbI_3$ compound.[11] In the context of occupying the B site in the ABX_3 system, lead has been reported as the superior constituent in comparison to its IVA metal counterparts such as tin, both in terms of stability and performance, and consequentially has been the most widely employed metal ion.[12] Ideally, utilization of lower atomic number elements (such as Ge or Sn) may result in a lower energy band gap since upon moving down the IVA group metals (Ge→Pb), the decrease in covalent character and electronegatively increases the band gap. However, the lower atomic number elements also exhibit low ionic stability in the divalent oxidation state owing to the reduced inert electron pair effects.[13] The halide anion X provides much more freedom of variation in its composition. Iodide, lying closest to Pb in the periodic table, shares a similar covalent character and thus, results in the most stable structure. Upon progressing down the VIIA group elements (Cl → I), with an increase in the atomic size of the constituent elements, shifting of absorption spectra towards longer wavelength (red shift) attributing to a decrease in electronegativity is observed. Such nature matches with the counterpart Pb ion at the B site and thus effectively reduces the ionic behavior and instead enhances the covalent character.[5] Hence, considering methylammonium lead iodide ($MAPbI_3$) as the prototypical example of the organolead

halide perovskites, it has been utilized as the material of interest for the entirety of my research work leading to this doctoral dissertation,

1.3 Symmetry and phase

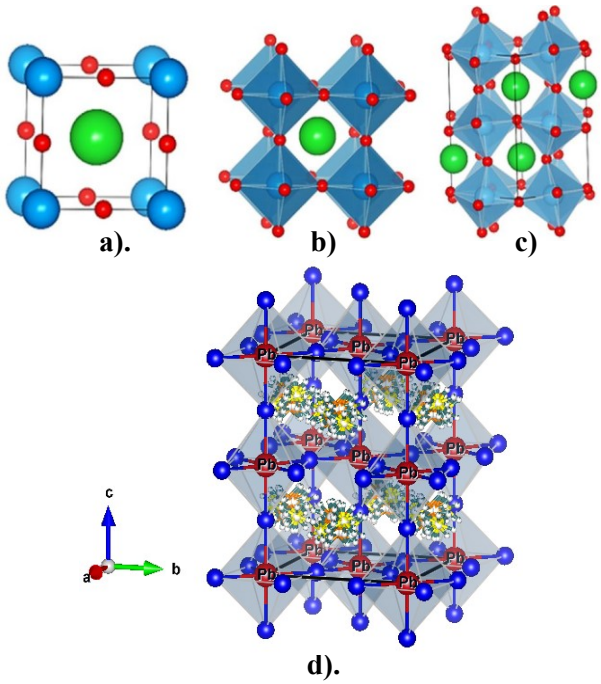

Figure 1.1 The ideal cubic unit cell of perovskite: (a) A cations (blue) occupy the lattice corners, B cations (green) occupy the interstitial site, and X anions (red) occupy lattice faces. (b) An alternative view showing B cations gathered around X anions to form BX_6 octahedra, as B-X bonds are responsible for determining electrical properties. (c) Tilting of BX_6 octahedra occurs from non-ideal size effects and other factors, inducing strain on the B-X bonds and (d) The ideal tetragonal unit cell of $MAPbI_3$. Source: Ref (5)

The $MAPbI_3$ exhibits three Bravais lattices i.e., orthorhombic, tetragonal, and cubic, stable in order of increasing temperature. Figure 1.1 a) b) and c) represent the crystal structure of an ideal cubic unit cell of a perovskite; where in the case of $MAPbI_3$, methyl ($CH_3NH_3^+$) occupies the A site while lead Pb^{2+} and I^- occupy the B and X site, respectively. Figure 1.1 d) represents the ideal tetragonal unit cell of $MAPbI_3$ based on ICSD #241477 data. The orthorhombic perovskite structure acquiring *Pnma* (a D_{2h} point group) phase is the low-temperature ground state of $MAPbI_3$ and maintains its stability up to 165

K after which it undergoes a first-order transformation to the tetragonal phase *I*4/*mcm* (D_{4h} point group), which continuously undergoes a second-order phase transition to the cubic phase $Pm\bar{3}m$ by 327K.[1] The lower temperature states could be accounted for by a $\sqrt{2}\times\sqrt{2}\times\sqrt{2}$ supercell expansion of the simple cubic perovskite cell unit. However, interestingly it has been noted in the current work and previous reports, that even after annealing samples at a temperature as high as 373K, the tetragonal phase may still surprisingly exist in thin films leading to ambiguity about the nature and the exact phase transition temperature between the tetragonal and the cubic phase.

1.4 Optoelectronic properties

The exceptional performance of organic-inorganic halide perovskites can be attributed to its substantial characteristics including but not limited to strong optical absorption with an adjustable band gap, ambipolar charge transport, long diffusion lengths, and thus minimized recombination rate, high carrier mobility, and high tolerance towards intrinsic defects. A half-micron thick perovskite film can achieve absorption across the entire visible spectrum which is substantially lower than the limitation of 2 um required to serve as an active layer in solar cells. A typical $MAPbI_3$ photovoltaic device is reported to achieve absorption up to nearly 800 nm.[5] With proper tuning of halide, divalent metal ion, and organic ion composition, the optical absorbance could be further extended in the infrared range.[14] The carrier diffusion length for $MAPbI_3$ has been reported up to 100 nm for both holes and electrons and up to 1 um in mixed halide perovskite $MAPbI_{3-x}Cl_x$ via the transient photoluminescence measurement.[15, 16] However, it has been observed that electron extraction poses a limitation in the case of $MAPbI_3$, unlike $MAPbI_{3-x}Cl_x$ where both holes and electrons could be extracted without needing electron transport material.[17] In terms of carrier mobility, almost an instant charge generation of highly mobile (25 cm^2/Vs) balanced free charge carriers is reported in $MAPbI_3$ within 2 picoseconds of illumination which may extend up to tens of microseconds.[18]

1.5 Challenges

High efficiency and long-term stability are the two key criteria for assessing any photovoltaic technology. The photovoltaic modules must complete the standard International Electrotechnical Commission (IEC) 61215 or 61646 design qualification testing protocols to be considered reliable and stable and compete with the existing silicon-based photovoltaic technology. To guarantee the warrantee period of the photovoltaic modules (with encapsulation) for at least 25 years, the modules should be able to retain a power output ≥ 80% of their initial output after 25 years. Despite exhibiting excellent

electro-optical properties and henceforth high power conversion efficiency of 25.2% in solar cells, the high responsivity of 10^4 A W^{-1} and detectivity of 3.7 x 10^{14} Jones in photodetectors, and high photoluminescence quantum efficiency of more than 90% in quantum dots, the long-term stability issues and lack ambient atmosphere compatible scalable coating techniques for developing large area perovskite-based devices, hinder the commercial viability of the perovskite-based optoelectronic devices.

1.5.1 Stability

As per the international standards (IEC 61646 climatic chamber tests), long-term stability at 358K is needed for a material-based device to compete with other solar cells/photovoltaic technologies. However, stability and material degradation issues are still a major concern for the organic-inorganic halide perovskites for their optimum utilization. Researchers have proposed multiple degradation pathways for $MAPbI_3$ which result in substantial degradation of its excellent light harvesting properties over time when exposed to prolonged humidity, heat, light, oxygen, etc. owing to the formation of PbI_2 after the loss of CH_3NH_3I.[19, 20] The degradation of $CH_3NH_3PbI_3$ into its initial reactant species i.e., CH_3NH_3I and PbI_2 is accompanied by the release of gases by a sublimation process. The first step of mass loss under an inert atmosphere is reported to occur during the thermal degradation of $CH_3NH_3PbI_3$ and CH_3NH_3I as follows:

$$CH_3NH_3PbI_3 \xrightarrow{\Delta} NH_3 + CH_3I + PbI_2 \quad (1.3)$$

$$CH_3NH_3I \xrightarrow{\Delta} NH_3 + CH_3I \quad (1.4)$$

Owing to the evolution of different gases during the degradation of $MAPbI_3$, researchers have proposed several interpretations of the degradation pathways. The degradation study conducted in the dry and inert gaseous environment by Fan et al. revealed that no hydrates of $MAPbI_3$ are released during the process, confirming the intrinsic hygroscopicity of the constituent CH_3NH_3 cations are not responsible for the $MAPbI_3$ phase transition to PbI_2. They instead proposed that the degradation of $MAPbI_3$ is a surface-dominated phenomenon and is kinetically preferred.[21] Niu and co-workers reported a series of chemical reactions held responsible for the degradation of $CH_3NH_3PbI_3$ in moisture in the following equations:

$$CH_3NH_3PbI_3 \rightleftarrows PbI_2 + CH_3NH_3I \quad (1.5)$$

$$CH_3NH_3I \rightleftarrows CH_3NH_2 + HI \quad (1.6)$$

$$4HI + O_2 \rightleftarrows I_2 + 2H_2O \quad (1.7)$$

$$2HI \rightleftarrows H_2 + I_2 \quad (1.8)$$

Therefore, degradation of perovskite due to moisture occurs with the $MAPbI_3$ transforming to MAI salt and metal halides, which could be accelerated by further decomposition of metal halide.[20] In another report, Walsh and co-workers demonstrated the formation of an intermediate complex $[(CH_3NH_3^+)_{n-1}(CH_3NH_2)_nPbI_3][H_3O]$ once the perovskite was exposed to Lewis base H_2O subsequently resulting in reduced stability of perovskites.[22] The interaction of water molecules with the highly hygroscopic MA^+ via hydrogen bond formation in the crystal structure of perovskite leads to the bond dissociation between the constituent of the crystal structure. Further, Philippe et al. demonstrated the migration and interdiffusion of each component, resulting in perovskite degradation upon thermal treatment.[23] Abdelmageed et al. disclosed that light exposure in the air oxidizes iodide anions that transfer electrons to p-type species such as O_2 and CO_2 in the atmosphere and form free radicals (O_2^- and CO_2^-) which deprotonate the ammonium group, finally resulting into the formation of highly volatile methylamine and leaving behind PbI_2. They proposed that $MAPbI_3$ films are insensitive to oxygen in the dark and stable under highly intense light in the absence of oxygen. Hence, light exposure and oxygen are combinedly responsible for the degradation of the perovskite.[24]

$$2CH_3NH_3I + \frac{1}{2}O_2 \xrightarrow{h\nu} 2CH_3NH_2 + H_2O + I_2 \quad (1.9)$$

$$CH_3NH_3I + CO_2 \xrightarrow{h\nu} CH_3NH_2 + HCO_2 + \frac{1}{2}I_2 \quad (1.10)$$

It has been observed that CO, an omnipresent gas undergoes a strong interaction with $MAPbI_3$. The exposure of perovskite film to the CO atmosphere leads to a lowering of work function and induces self-doping in the $MAPbI_3$ film. Interaction with CO at the perovskite film interface leads to layer-by-layer depletion of the organic moiety leaving behind PbI_2 and this also softens the film over time (details in Chapter 3).

Apart from the degradation induced by the external environment, $MAPbI_3$ and other organohalide lead perovskites are also subject to significant degradation in presence of an external electric field. When an external bias is applied across a perovskite-based device, three important phenomena may occur. First, owing to their low activation energy, primarily the I^- and organic cation may migrate towards the

electrodes of opposite polarity.[25] The theoretical and experimental studies reveal that the I^- ions migrate along the I−I edge of the PbI_6 octahedron and have the lowest activation energy (E_A) of 0.08–0.58 eV; the MA^+ ions migrate through the unit cell face comprising four I^- ions and have higher E_A of 0.46–0.84 eV; and the Pb^{2+} ions migrate along the diagonal of the cubic unit cell and have the highest E_A of 0.80–2.31 eV. Secondly, owing to the change in the internal electric field due to the ion migration or dipole orientation, hysteresis in the light-current-voltage (light *I-V*) characteristics of perovskite solar cells is observed. Finally, the photovoltaic effect is observed due to the self-doping effects of perovskite caused by the migration of internal ions.[26] The biasing test results have shown that the performance of the perovskite solar cells is severely degraded at voltages greater than the built-in potential or open-circuit voltage (V_{oc}).[27]

1.5.1.1 Strategies toward enhancing stability

As discussed above, as the adsorption of water, oxygen, and corrosive molecules proves to be detrimental to the stability of the perovskite material and leads to a substantial loss in its photovoltaic performance, a sensible material engineering is required to prevent such surface dominated phenomenon from occurring. Though strategies involving substrate modification or perovskite layer passivation via an interfacial or a barrier layer made of specific chemicals (e.g. poly(N, N'-bis(4-butylphenyl)-N, N'-bis(phenyl)benzidine) (polyTPD)), encapsulation of the complete device (e.g. thermosetting epoxy glue), variation in charge transport layers (e.g. spiro-MeOTAD, PEDOT: PSS) and compositional engineering via alteration in the constituent species of the hybrid perovskites (e.g. mixed cation and halide doping) have been used, these are limited to use of inert operating conditions or need special fabrication steps and chemicals.[28] As these special measures of preventing perovskite degradation mostly don't take into account, the specific interaction between the constituent ions into consideration, such strategies are at times too complex to carry out in a normal lab environment.

Instead, solution chemistry engineering, involving molecules that may lead to van der Waals interactions, Lewis acid-base interaction, or formation of hydrogen or halogen bond, etc. could serve as a simpler and better alternative to the above-mentioned techniques. These have been successfully deployed to passivate perovskite surfaces and prevent the interaction of the perovskite surface with unfavorable chemical species. Such wise solution engineering results in the enhancement of the stability and the photovoltaic performance of the hybrid perovskite devices. A Lewis acid-base interaction leads to either an adduct formation or a redox reaction. The adduct formation reaction involves the linking

of the acid and base moiety via a dative bond (i.e., shared electrons originating from the Lewis base). This intermediate adduct facilitates a homogeneous crystal growth of the perovskite due to the supplementary removal of the Lewis base from the adduct film, which in turn retards the formation rate constant for the perovskite. Dimethyl sulfoxide (DMSO), a polar aprotic solvent is one such typical Lewis base, possessing a lone pair rich oxygen atom. It forms an adduct with the Lewis acid of PbI_2 which lowers the rate of perovskite formation and thus leads to higher crystallinity in the resulting organohalide lead perovskite. The formation of such an adduct also aids in the formation of a larger crystal grain size. The initial work based on DMSO adduct formation reported highly efficient perovskite solar cells with an average η of 18.3%. The adduct formation is revealed by the shift of the S=O vibrational peak in DMSO.[29] Other polar aprotic small molecules such as urea, and N-methyl-2-pyrrolidone (NMP) has been investigated as well. Besides these, Lewis acid-base adducts, including $HPbI_3$, PbI_2-thiourea, and PbI_2-$DMSO_{1-x}thiourea_x$ have been reported in the literature as precursors for the formation of perovskite films with large grain size and low defect density.[30]

The addition of several types of chemical additives such as inorganic or ammonium salts, organic molecules, ionic liquids, fullerenes, and polymers have been also attempted in the perovskite precursor solution. Based on the classic crystallization theory, the addition of an additive into the perovskite precursor solution is a viable way to modulate the crystallization dynamics as well as change the overall film morphology.[31] The variation in functional mechanism and interaction of each additive with perovskite precursors may affect the resultant perovskite material in several ways. The introduction of an additive may provide reduced heterogeneous nucleation sites to improve the uniformity or may aid in coordinating with metal ions to decrease the crystallization rate and enlarge crystal grain size or may instead change the surface energy to control the crystal growth directions or combination of all these.

During the degradation process, owing to the low activation energy of primarily I^- and MA^+, the perovskite precursors PbI_2 and $CH_3NH_3^+$ start migrating within the material, especially across the grain boundaries. The individual perovskite moieties need to be kept bound to limit such ion migration.[27] Since PbI_2 and CH_3NH_3I provide Lewis acid characteristics and a cationic interaction, respectively, specific chemical interaction of each of the perovskite precursors with a polymer additive is possible. Such chemical interaction between the polymer and individual perovskite precursors may keep the material intact by limiting ion migration. Further, the presence of atoms such as oxygen, in a polymer could lead to the formation of hydrogen bonds with the H atoms in $CH_3NH_3^+$ to provide resistance against humidity. The electron lone pairs from some atoms (e.g., S and N atoms) in the polymer may

strongly interact with Pb ions, which in turn may stabilize the 3-D framework of perovskite. There exist numerous reports of polymer additive-based $MAPbI_3$ devices e.g. poly(ethylene glycol) (PEG), polyvinylpyrrolidone (PVP), polyacrylonitrile (PAN) polyacrylic acid (PAA), trimethylolpropane triacrylate (TMTA), etc. where the specific interaction between the polymer additive and the perovskite precursor aids in uniform high surface coverage, controls crystallization kinetics of perovskite formation and enhances device characteristics and stability.[32-35] Overall, polymer additives are reported to significantly enhance the stability & device characteristics of the resultant perovskite-polymer composite material.

1.5.1.2 Polystyrene: an efficient polymer additive for inducing stability in $MAPbI_3$

As discussed above, the challenge of enhanced stability of perovskite material while operating $MAPbI_3$-based devices in ambient conditions, needs to be addressed more simply. To address this challenge, our research group has developed a solution-engineering strategy for stabilizing the organic-inorganic lead halide perovskites. While the Lewis acid characteristics of the PbI_2 mediates cross-linking of PS, a cation-π interaction exists between the MAI and PS chains. Such combined effect of the interaction of PS with both perovskite precursors results in a well-coordinated long-range molecular ordering of the polymer chains along perovskite grain boundaries and at the interfaces. Also, PS is miscible in perovskite solvent and does not evaporate, unlike DMSO which has a comparatively high vapor pressure. Thus, PS remains in the perovskite film even after crystallization at high temperatures and a longer annealing time.

1.5.1.2.1 Mechanism of PbI_2 initiated PS cross-linking in PS-$MAPbI_3$

The previous work based on polystyrene interaction with Lewis acid, suggests PbI_2 mediated PS cross-linking at the perovskite grain boundaries in PS-$MAPbI_3$, by the mechanism shown in Figure 1.2.[36] Due to limited moisture available in the perovskite precursor solvents and also, absorbed from the atmosphere, the PbI_2 Lewis acid hydrolyzes and leads to the simultaneous formation of hydrogen iodide (HI) in the perovskite. The HI then combinedly interacts with the PbI_2 and PS to form a cation complex on the aliphatic chain of the polymer i.e., polymeric cation complex with PbI_3^-. The formation of such a cationic complex leads to an upshift in Nuclear Magnetic Resonance (NMR) resonance for both aliphatic and aromatic regions of PS.[37] The complex cation complex further loses the H_2 and is converted to carbonium ions, subsequently causing cross-linking of the polymer chain. It is

hypothesized that the formation of such carbonium cation and subsequent cross-linking of PS may take place at either α or β carbon atoms of the PS aliphatic chain (Details in Chapter 7).

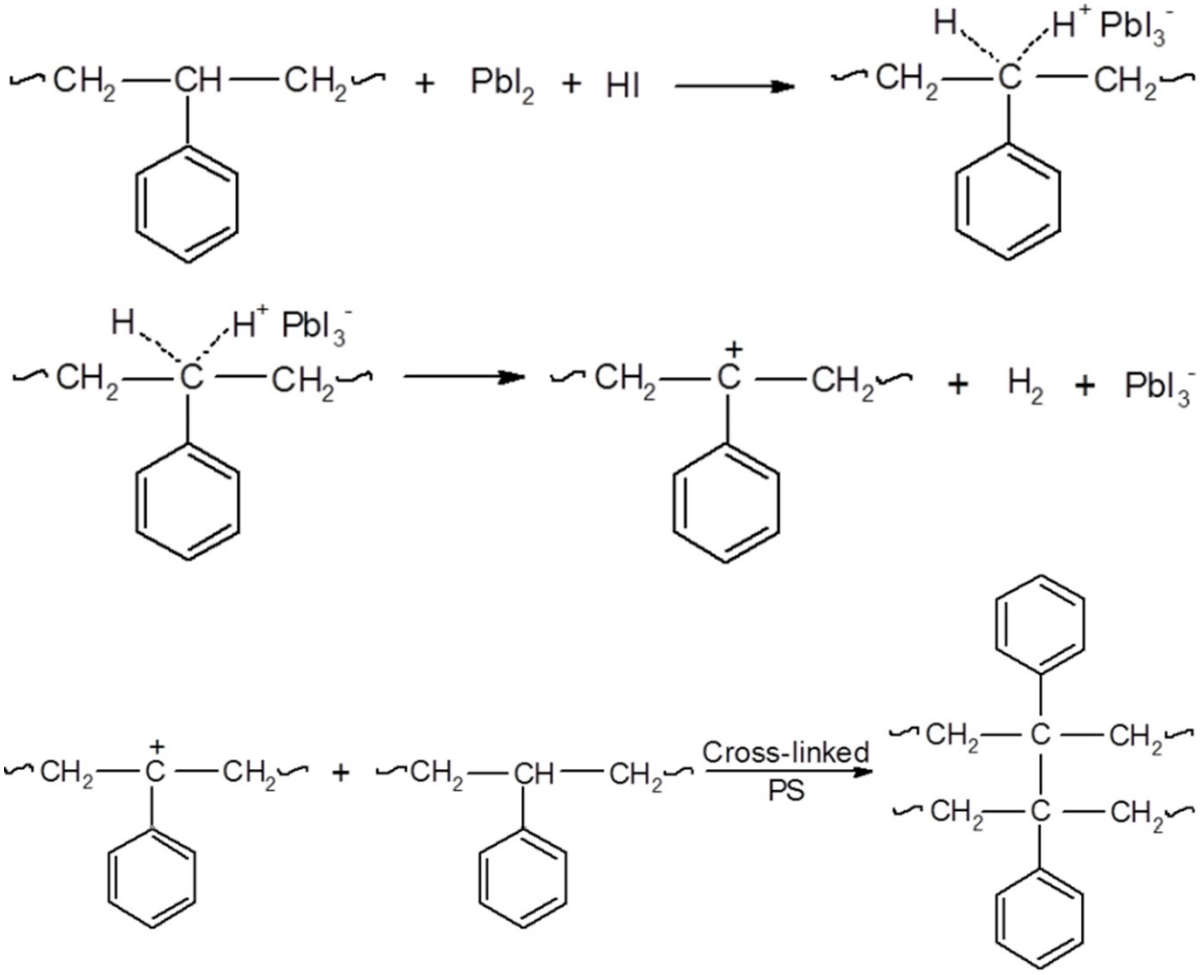

Figure 1.2 Mechanism of PbI_2 mediated cross-linking of PS in PS-$MAPbI_3$. Source: Ref (37)

Although in the presence of moisture, other than PbI_2 initiated cross-linking of PS, another potential mechanism may exist in the polystyrene system that may instead lead to its degradation. However, the NMR and the Gel Permeation Chromatography (GPC) results confirm the cross-linking mechanism is a favorable reaction. The GPC results confirmed an increase in average Mw in the PS-$MAPbI_3$ while no change is observed in relative intensities of the aromatic and aliphatic regions in the NMR spectra, thus, elucidating the intact nature of the polymeric backbone.

1.5.1.2.2 Cation-π electron interaction between MAI and polystyrene

Other than PbI_2 initiated cross-linking of the PS, PS chains can also coordinate with perovskite crystal defects of $CH_3NH_3^+$ at the grain boundaries and interfaces owing to π electron-cation interaction (Figure 1.3) which is well illustrated in natural biological systems.[38, 39] It has been reported that, although the grain boundaries are not the dominant location for non-radiative recombination, they may result in electronic trap states which may limit the charge carrier lifetime and photoluminescence (PL) yield.[40] In addition, these grain boundaries act as preferred channels for moisture diffusion and ion migration, ultimately leading to grain degradation and reduced stability of perovskite material. Owing to the low activation energy of MA^+ and I^-, ion migration of these ionic species occurs first. The specific chemical interaction between the MAI and the polystyrene can efficiently control this migration.

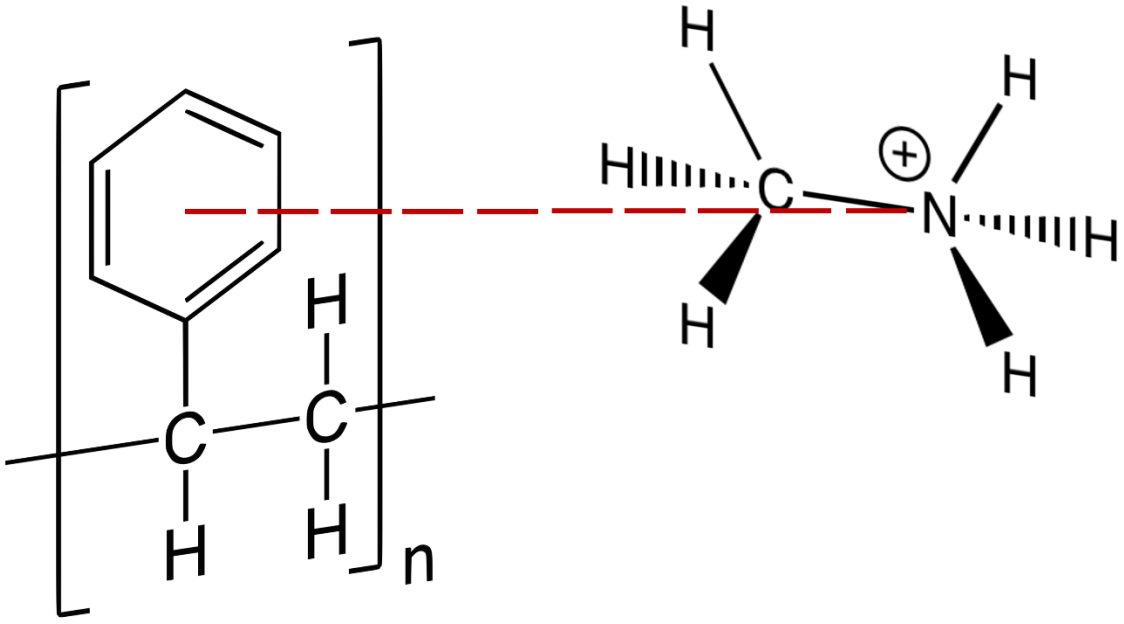

Figure 1.3 Cation-π interaction between polystyrene and methylammonium cation.

1.5.2 Scalable manufacturing of perovskite optoelectronics

The price per unit of energy referred to as the Levelized cost of energy (LCOE) can be effectively used to capture the cost competitiveness of perovskite photovoltaics.[41] Several cost model calculations have shown that perovskite LCOE can compete with the energy-intensive silicon and cadmium telluride (CdTe) photovoltaic technology, given that the requirements of high efficiency, low cost, and long lifetime, can be concurrently met.[42] The solution processible nature of perovskites provides the

opportunity to greatly reduce the capital expenditure for scalable manufacturing. Although to exploit this potential, solution methods that are compatible with high throughput manufacturing are needed. In this pursuit, the scalable deposition methods need to meet three major requirements. First, the efficiency achieved with the scalable deposition method needs to match with that obtained by the conventional spin coating technique. Second, there should be a minimal drop in efficiency when moving from lab-scale devices to large area modules. Lastly, the method needs to be compatible with high throughput production processes, either sheet-to-sheet or roll-to-roll manufacturing. Therefore, techniques such as doctor-blade coating, slot-die coating, spray coating, and inkjet printing, are now being widely used and are considered more appropriate candidates than spin coating for upscaling perovskite manufacturing.[43] However, most of the reported devices fabricated by such large area coating methods involve energy-consuming heating step during the coating or/and inert atmosphere.[44]

Thus, developing ambient atmosphere stable perovskite optoelectronics by large area coating techniques such as blade coating at room temperature possesses great potential for scalable manufacturing of perovskite optoelectronics (details in Chapter 6).

1.6 PS-$MAPbI_3$ strategy towards advanced optoelectronics

1.6.1 Photodetectors

A photodetector converts an optical input such as visible light photons into an electrical signal and has wide-ranging applications in the detection of light intensity, spectral range detection, thermal imaging, remote imaging, and so forth. The significant figures of merit for photodetectors include responsivity, detectivity, light switching ratio (on/off ratio), spectral selectivity, linear dynamic range, and response time. Currently, most commercial photodetectors are based on crystalline GaN, Si, and InGaAs. The underlying mechanism driving the photodetector operation is either a p–n (p–i–n) junction, Schottky based, or a photoconductive effect, where the conductivity of the active material increases on interaction with the incident photons. Broad spectral range (190–1100 nm) commercial photodetectors based on the Si p–n junction (photodiodes) (*e.g.*, Hamamatsu S1336) exhibit peak responsivities of 0.12 and 0.5 A W^{-1} at 200 and 960 nm, respectively, and those designed especially for the visible range (340–720 nm) photometry (*e.g.*, Hamamatsu S8265) exhibit a responsivity of 0.3 A W^{-1} at the peak sensitivity wavelength of 540 nm, with a dark current of ~20 pA. These commercial photodetectors usually require an external power supply and hence need an integrated assembly in the device which can make the device bulky and serve as a bottleneck for utilization in a remote location.

Furthermore, these commercial photodiodes need stringent manufacturing controls which limit them to low-volume, high-value markets. To overcome the existing trade-offs between performance, form factor, cost, and most importantly, power consumption, self-powered photodetectors are being investigated with intense interest. Self-driven photodetectors can be obtained when photodiodes work at zero bias, similar to solar cells working under short-circuit conditions. Currently, most self-powered photodetectors are demonstrated through the integration of the photodetectors with external power sources such as piezoelectric and/or triboelectric nanogenerators to operate in a self-powered mode. However, since these devices work only in the presence of continuously varying mechanical input, their measurement is intermittent. To address, this challenge, the perovskite thin film-based self-powered photodetectors can offer the benefit of being lightweight with small device size, without compromising on device performance. Owing to the inherent semiconducting nature and the electric field-induced effects in $MAPbI_3$, these can further exhibit self-powered operation. In this pursuit, developing self-powered continuously operable photodetectors with enhanced stability is mandatory. The PS integrated $MAPbI_3$ photodetectors fabricated as part of this dissertation work show enhanced performance and stability (details in Chapters 2, 3, and 4).

1.6.2 Flexible device application

Compared with the traditional devices based on rigid substrates such as silicon, flexible electronics have wider applications in the field of wearable and portable devices owing to their ability to bend, stretch, and have a reduced weight. Their promising applications are in the fields of healthcare, robotics, epidermal sensing, and so forth. Flexible solar cells and photodetectors based on perovskite thin films are therefore receiving more and more attention for their favorable traits, including flexibility, light weight, portability, and compatibility with curved surfaces.[45] More importantly, mass production and throughputs of such perovskite thin films can be achieved by continuous roll-to-roll or sheet-to-sheet technology contributing to reduced industrial costs. Despite exhibiting the promise of low-temperature solution processing, the rigid and brittle nature of the perovskite layer hinders their advancement in the field of flexible electronics. The high mechanical modulus of the perovskite material (compared to polymers) coupled with low fracture toughness and strain leads to limited dissipation of mechanical energy.[46] This may result in the development and propagation of cracks across the film leading to catastrophic mechanical failure and loss of device performance. Apart from the absorber material, the deterioration of the electrodes upon cycling also plays an indispensable role in determining the overall performance of such flexible devices. Researchers have made great efforts to optimize perovskite

material, charge transport layers, and electrode materials.[47] However, three issues still challenge the further development of flexible perovskite-based devices for practical application: limited flexibility in terms of unfavorable bending and stretching durability combined with environmental stability issues, and reduced efficiency on a large scale.[48]

The motivation is to utilize the low-temperature solution-processing and light absorption characteristics of the perovskite thin films to develop a stretchable photodetector. Solution-processed Pt-Au nanochains have been utilized to serve as mechanically durable and highly conductive electrodes. To address the rigid and brittle nature of the polycrystalline $MAPbI_3$ which otherwise serves as a bottleneck in the long-term operation of such stretchable devices, the viscoelastic and low modulus of PS additive is utilized to ensure that the PS-$MAPbI_3$ photodetector sustains appreciable performance despite being subjected to 10,000 stretching cycles and exhibits enhanced stability in the ambient atmosphere (details in Chapter 5).

1.6.3 Solar cells

Abiding by the United Nation's sustainable development goal no. 7 i.e., affordable, and clean energy, as we look forward to fulfilling the aims of ensuring access to reliable, sustainable, and modern energy for all, solar energy harvesting through photovoltaic conversion has emerged as of the most promising technologies for long-term renewable energy production.[49] While multiple policies are being rolled out to try and achieve net-zero carbon emission in the next few decades, the use of solar panels continues to grow around the world. In this pursuit of photovoltaics, crystalline silicon has served as the go-to-choice material for decades. However, getting the purest silicon wafer for fabricating a solar cell is a costly affair. Not only a thick silicon wafer is required but it also needs to be manufactured at high temperatures to get rid of the impurities. Hence, silicon solar cells are highly energy intensive to produce with considerably higher energy payback time.[50] Further, silicon solar panels do not fare well on the front of the greenhouse gas emission factor either, representative of the CO_2 emitted per unit of energy generated.[51] Other materials like copper indium gallium selenide (CIGS) and cadmium telluride (CdTe) have popped up, but they only cover a small piece of the market - about 5% owing to their non-feasible and expensive production methods.[52]

Amid this, the solution-processed, cost-effective yet highly efficient perovskites-based solar cells are revolutionizing photovoltaic technology owing to their excellent electro-optical properties. Within a short span of the past decade, the power conversion efficiency of perovskite-based solar cells has

surpassed 25% owing to the combined efforts in material optimization, device architecture, and interfacial engineering.[53-57] However, these high-efficiency devices have not necessarily been stable or possible to fabricate at a large scale (as discussed in section 1.5.2). For widespread deployment of perovskite-based solar cells, maintaining high efficiencies while simultaneously achieving long-term stability for perovskite solar cells with a large active area, remains a critical hurdle.[58] The room temperature blade coating technique utilizing PS additive strategy to coat ambient atmosphere stable perovskite films over large area substrates can hence serve as a pioneering step towards addressing this dual challenge (details in Chapter 6).

1.7 Thesis Outline

The thesis chapters are organized as follows:

Chapter 2 focuses on the long-term adverse effect of exposure to organolead halide perovskite under carbon monoxide (CO), an omnipresent gas in the atmosphere. The strong interaction of the CO at the perovskite ($MAPbI_3$) interface leading to the desorption of O_2 and softening of the films due to the formation of the PbI_2 rich phase is investigated. The lowering of the work function and formation of a p-n junction at the top interface of perovskite film is presented. The effective utilization of limited exposure of CO in enhancing the self-powered performance of a perovskite-based photodetector is highlighted.

Chapter 3 emphasizes utilizing the strong interaction capabilities of polymers with contrasting nature, independently and in form of block co-polymers for enhancing the stability and efficiency of the perovskite thin-film-based electro-optical devices. The hydrophilic polar PEG and hydrophobic non-polar PS polymers in a PEG-PS block co-polymer system have been investigated to better understand the effective contribution of each polymer counterpart when mixed alongside perovskite precursors. The inevitability of achieving long-term ambient atmosphere stable films in absence of the hydrophobic PS counterpart is argued.

Chapter 4 highlights the optimization of the molecular chain length of the PS additive and the nanoscale tri-layer architecture of the polymer-perovskite films involving polymer-rich top and bottom layers and the ubiquitous presence of polymer across the perovskite-rich interlayer. This understanding is further correlated with molecular weight-driven mobility and volume of the polymer chains leading to the rearrangement of the polymer chains within the perovskite film which affects the crystallization kinetics

and, hence, perovskite grain size. Further, the resultant electro-optical characteristics especially ion migration and conduction of electronic charge modeled as a function of the polymer chains is discussed.

Chapter 5 is focused on the extension of perovskite-based devices beyond rigid substrates to realize perovskite thin film-based stretchable photodetector. By incorporating polymer chains in the $MAPbI_3$ films, the strategy to alter the mechanical modulus and the viscoelastic nature of the films is presented. Moreover, the utilization of solution-processed nano chains to form flexible electrodes is highlighted. The superior electro-optical response of the perovskite-polymer device with minimal decay in performance over 10000 stretching cycles owing to the fundamental difference in the dissipation of the mechanical energy between the pristine perovskite and PS-$MAPbI_3$ device, is conferred.

Chapter 6 showcases the upscaling of perovskite film fabrication to pave the way for roll-to-roll manufacturing of perovskite films. The advantages of replacing the conventional spin-coating technique with an ambient atmosphere blade coating technique and combining it with the PS additive strategy to ensure compact pin-hole-free perovskite film deposition are highlighted. Structural, morphological, and spectroscopical data along with ToF-SIMS depth profiling of the resultant pristine perovskite and PS-$MAPbI_3$ films is analyzed. Initial *J-V* characteristics of the prototype large area solar cell with stability test in the ambient atmosphere are shown.

The results of this thesis are summarised in Chapter 7, along with suggestions for future work.

Chapter 2

Carbon Monoxide Induced Self-Doping in Methylammonium Lead Iodide Films and Associated Long-Term Degradation Effects

2.1 Introduction

Processing and operation of electro-optical devices, in general, leads to their exposure to different gases either in a controlled setting or in ambient conditions. The interaction with gas molecules can critically affect the interfaces in the devices and hence will impact their performance.[59-62] Therefore, understanding such interactions and their effects is required for developing proper device processing conditions and the physics governing their operation. Organolead halide perovskites such as methylammonium lead iodide ($MAPbI_3$) due to their high-performance electro-optical characteristics are being applied in commercial photovoltaics and are also intensely researched in devices such as photodetectors, light-emitting diodes, and self-powered sensors.[63-71] Their structural stability is affected by interaction with a variety of gas molecules such as O_2 and water vapor which has led to preventive steps in processing to limit their exposure to these species.[72-75] The key is the mobility and the stability of the CH_3-NH_3^+ (methylammonium) and the I^- species, which interact with such molecules and lead to the decomposition of the $MAPbI_3$.[76-78] However, the effect of gases that are present in a limited concentration in the atmosphere and many controlled conditions, can be detrimental owing to their strong interaction with $MAPbI_3$.[79, 80] Limited research has been conducted in this area which can provide critical insights into increasing the stability and performance of the perovskite-based devices.[81, 82]

In this work, we show through the use of a variety of gases that carbon monoxide (CO) has strong interaction with $MAPbI_3$. Due to this strong interaction, CO can displace the O_2 adsorbed on the surface, and cause a rapid change in the characteristics of the $MAPbI_3$. Exposure to CO leads to increased surface roughness, change in grain size, and redistribution of organic and inorganic moieties causing the layer-by-layer formation of PbI_2 starting at the top interface, and softening of the film over time. Two contrasting effects in terms of device performance are observed based on the extent of CO exposure. At limited exposure, a thin top layer of PbI_2 is formed, as a result, the short-circuit current (I_{sc}) of the perovskite device poled (when an external bias is applied) in dark and under CO environment shows 122% enhancement in comparison to devices poled in ambient, O_2, and N_2, and CO_2 atmosphere. However, prolonged exposure to the CO environment in combination with light and electrical bias leads

to catastrophic degradation of perovskite films. This can be attributed to the formation of pinholes and accelerated loss of volatile species from the surface, in addition to the formation of insulating PbI_2 clusters. Such a detailed understanding of the effects of CO exposure will enable the design and optimization of perovskite-based optoelectronic devices for their application in not just photovoltaics but also for emerging applications in self-powered and piezoelectric devices.[83-85]

2.2 Experimental Section

2.2.1 Synthesis of CH_3NH_3I precursor

Methylammonium iodide (MAI) was synthesized by dropwise addition of 30 mL of hydroiodic acid (57 wt. % in water, Sigma-Aldrich) to 27.8 mL of methylamine (33 wt. % in absolute ethanol, Sigma-Aldrich) under constant stirring at 0 °C. This solution was stirred for 2 hours and later, a dark yellow precipitate was recovered using a rotary evaporator at 60 °C for 1 hour. The solid precipitate was then washed and recrystallized with a copious amount of diethyl ether and ethanol, respectively, until it turned white. The resultant white precipitate was dried overnight to obtain pure MAI.

2.2.2 Synthesis of perovskite precursor solution

The 1.35M perovskite solution was prepared by mixing 79.4 mg of MAI and 230.5 mg of lead iodide (99.999% trace metals basis, Sigma-Aldrich) in the solvent comprising 53.3 ul of dimethyl sulfoxide (anhydrous, ≥99.9%, Sigma-Aldrich) and 317.5 ul of N, N-dimethylformamide (anhydrous, 99.8%, Sigma-Aldrich). Further, 1 wt/v % PS with a polydispersity index (PDI) of 1.02 (0.0037g PS of average Mw 35,000 and, Sigma-Aldrich) was added to the precursor solution to ensure resultant films stay stable and avoid moisture-induced degradation before exposure to CO. The solution was stirred on a magnetic stirrer for 30 minutes before spin-coating.

2.2.3 Spin coating of perovskite precursor solution and fabrication of perovskite-based photodetector

The perovskite films were spin-coated on Si/SiO_2 chips having equidistant gold electrodes at 200 μm to fabricate the lateral configuration of a self-powered photodetector device (Figure 2.1). The chips were initially washed with Millipore water and later ultrasonicated in acetone and isopropanol for 5 minutes each and finally, re-washed with Millipore water. The chips were then Piranha treated (3 H_2SO_4:1 H_2O_2) for 3 minutes, washed with copious Millipore water, and finally dried with an N_2 gun.

The precursor perovskite solution was spin-coated on the cleaned chips at 4000 rpm for 30 seconds. Upon reaching 6 seconds of rotations, 200 µl of diethyl ether was added. The obtained films were annealed stepwise at 65 ºC for 2 minutes followed by 100 ºC for 3 minutes to ensure complete perovskite phase formation.

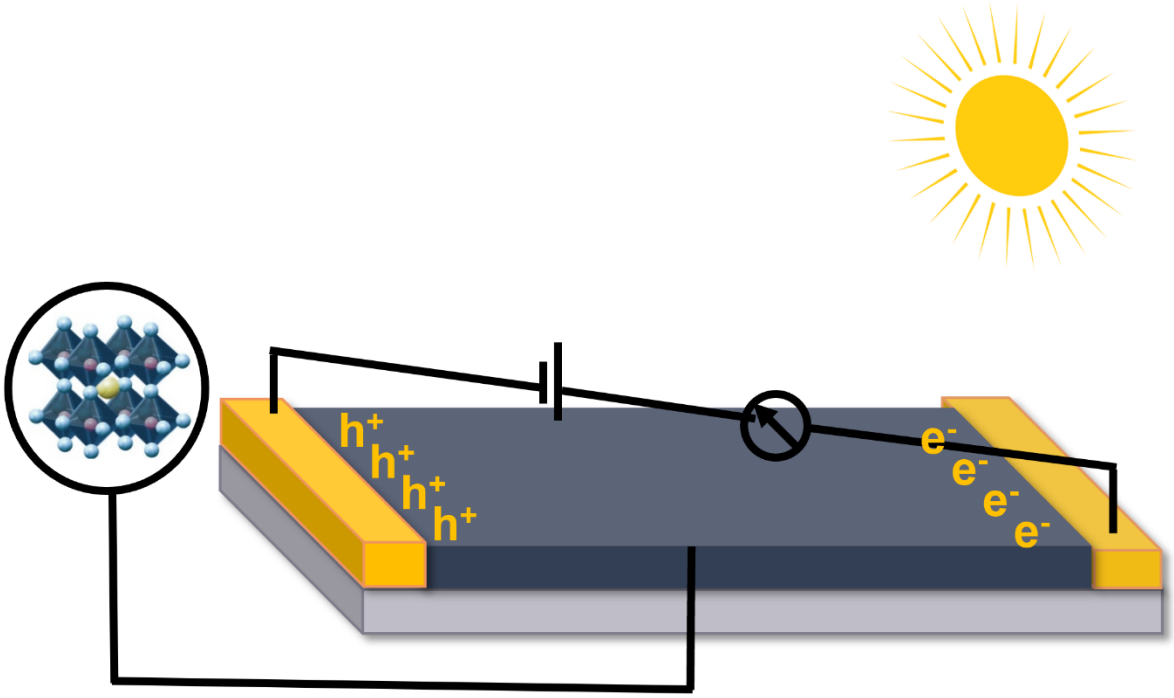

Figure 2.1 Schematic illustration of the lateral device configuration of Au/perovskite/Au.

2.2.4 Structural, microscopic, and spectroscopic characterization

The grazing incidence X-ray diffraction (GIXRD) patterns of obtained samples were measured using a PANalytical X'Pert Pro MRD diffractometer with Cu Kα radiation (λ = 1.54 Å) at an incidence angle of 0.4°. The X-ray diffraction from the bulk material was characterized using PANalytical Empyrean diffractometer with Cu Kα radiation (λ = 1.54 Å). The samples used for X-ray diffraction were exposed to a steady rate of dry air and CO under dark and light conditions, independently for 3 hours, and were not subjected to any external bias (poling). A Zeiss Ultraplus field emission scanning electron microscopy (FE-SEM) equipped with energy-dispersive X-ray spectroscopy (EDX) was used to examine the surface topology and grain size distribution of the pristine and CO-exposed perovskite films. Further, Raman spectroscopy was performed over Horiba HR800 spectrometer in the

backscattering configuration. All Raman spectra were recorded at 532 nm excitation wavelength at a power of 6 mW. The samples used for FE-SEM and Raman spectroscopy consisted of perovskite films exposed to a steady flow of dry air and CO. This exposure to gases was either carried out in dark or under light for 60 minutes each. The poled perovskite films refer to the samples where a constant voltage of 2 V was applied across the gold electrode and ground, during the 60 minutes of exposure to requisite gases. The depth profile of freshly prepared and perovskite films exposed to CO for 6 hours was analyzed using time-of-flight ion mass spectroscopy by employing a Cs^+ ion source (500 eV) for sputtering and Bi^{3+} (30 keV) for analysis over ToF-SIMS 5, ION-ToF GmbH. A Stanford Research Systems Universal Gas Analyzer (UGA) system was used to analyze the gases present in a custom-made sealed quartz beaker. The required gas was initially purged and maintained within the sealed beaker. Later, a 1.8 m long capillary tube (175 μm inner diameter) was inserted into the beaker to monitor the change observed in the partial pressures of O_2, N_2, and CO upon opening the outlet valve. The Young's Modulus maps were acquired using RTESPA 525 probes (Bruker) with a nominal spring constant of 200 N/m and resonant frequency of 525 kHz on a Bruker Dimension Icon in PeakForce Quantum Nanomechanical (PF-QNM) mode. The spring constant and deflection sensitivity of the probes were calibrated using a sapphire standard sample before each measuring session. The tip radius was estimated to be 20-30 nm, using a Titanium sample of known roughness. The elastic modulus for the sample surface was calculated following the Derjaguin-Muller-Toropov (DMT) model for tip-sample contact. The contact potential difference (V_{CPD}) maps were acquired with the topographic signal simultaneously at an effective tip-sample lift height of 80 nm on a Bruker Dimension Icon in Amplitude Modulated - Kelvin Potential Force Microscopy (AM-KPFM) mode using SCM PIT probe (Bruker). The topographic height was obtained by maintaining the amplitude of the first cantilever resonance at 65.8 kHz at a predefined amplitude setpoint of approximately 30 nm. The V_{CPD} was then determined by compensating the ac component of the electrostatic force at angular frequency ω with an applied dc voltage (= $|V_{CPD}|$) in a feedback control loop. To separate the topographic signal from the V_{CPD} signal, enhance the sensitivity and minimize the probe-sample convolution effects, the alternating current (AC) electrostatic force component was generated at the cantilever's 2nd resonance frequency of 411 kHz.

2.2.5 Electrical measurements

The electrical measurement on the planar lateral device configuration of the Au/$MAPbI_3$/Au self-powered photodetector was conducted using a probing station. A two-probe method was employed by connecting one probe to a gold electrode on the chip and another probe connected to the ground. A

Keysight 6614C 50-Watt system power supply with a maximum voltage output of 100 V was used for applying an external bias. For carrying out optoelectronic measurements of a perovskite-based self-powered photodetector device, an external bias of 2 V was applied (referred to as poling) for 5 min under exposure of various gases (O_2, N_2, CO_2, and CO) and in ambient atmosphere. This poling time was chosen to induce optimum polarization in perovskite film without incurring spontaneous material degradation. Post poling, optoelectronic measurements including the open-circuit voltage (V_{oc}) and the short-circuit current (I_{sc}) were sequentially measured using a Keysight 3458A Digital multimeter. The film was connected in series with the multimeter and power supply to complete the circuit. The illumination/light exposure, wherever reported, refers to simulated airmass 1.5 global irradiation (100 mW/cm^2), generated using a Xenon-lamp based solar simulator (Newport Oriel Instrument 67005, 150 W Solar Simulator). An NREL calibrated KG5 silicon reference cell was used to calibrate light intensity to minimize any spectral mismatch.

2.3 Results and Discussion

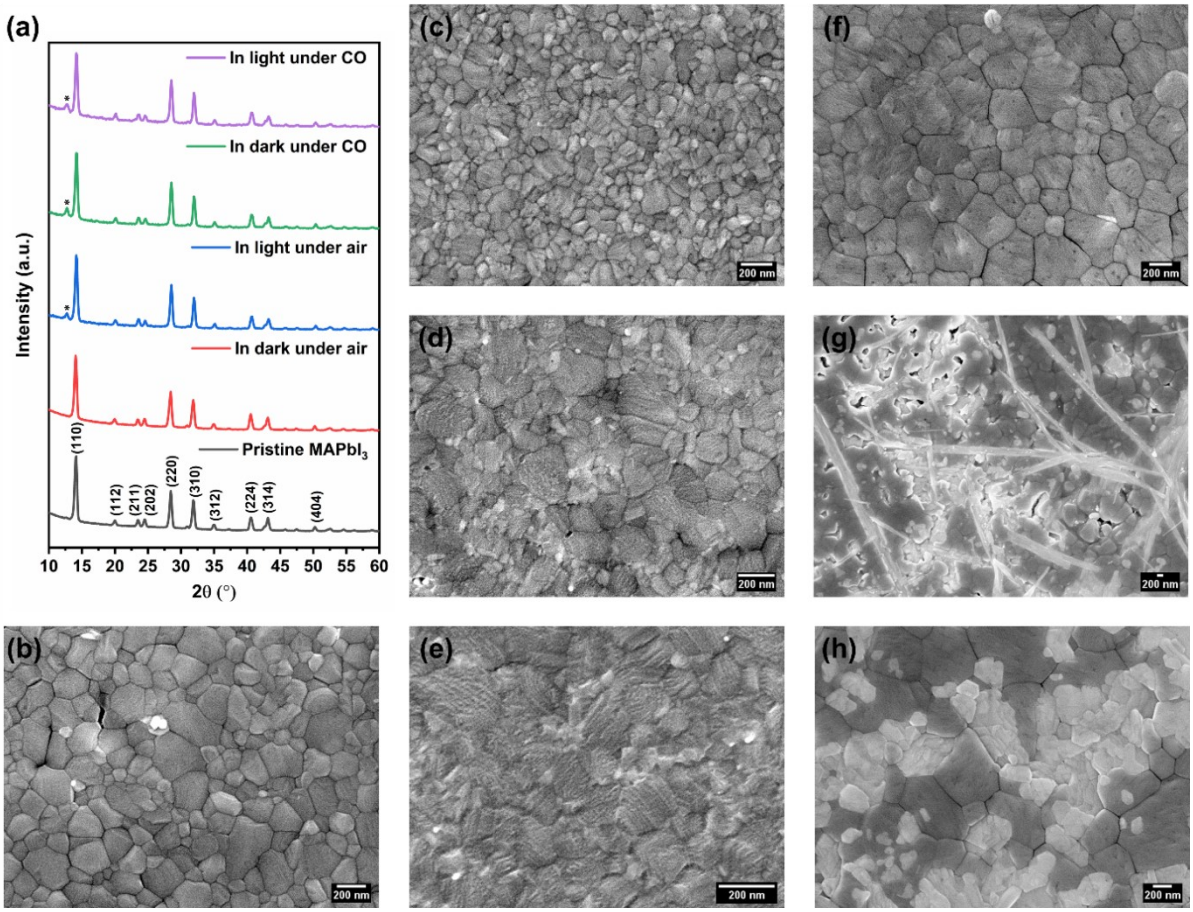

Figure 2.2 (a) XRD pattern of pristine $MAPbI_3$ and films exposed to dry air and CO under dark and light. Here, * corresponds to the PbI_2 diffraction peak. FE-SEM images of (b) pristine $MAPbI_3$ film. Striations begin appearing in the perovskite film exposed to CO in dark for (c) 1 hour and (d) 3 hours without poling and they further intensify after (e) poling for 1 hour. Pitting and merging of grains is observed in FE-SEM images of (f) unpoled perovskite film. Needle-like PbI_2 flakes and pinholes develop in (g) poled $MAPbI_3$ film exposed to CO in light for 1 hour. (h) The bulk PbI_2 phase is observed in the FE-SEM image of the perovskite film exposed to CO for 3 hours in light without poling.

The grazing angle X-ray diffraction (GIXRD) pattern of $MAPbI_3$ films is shown in Figure 2.2a. Due to the sensitivity of the GIXRD to surface layers, the change and decomposition of $MAPbI_3$ film surface on exposure to specific gases is observed. The presence of the tetragonal phase of $MAPbI_3$ is confirmed by the intense diffraction peaks of (1 1 0), (2 2 0), and (3 1 0) h k l planes. No PbI_2 phase is observed

in pristine $MAPbI_3$ or in films that have been exposed to dry air (hence also O_2) in dark conditions. However, the perovskite film exposed to dry air in light for 3 hours, exhibits a new peak at 12.7º corresponding to the (0 0 1) h k l plane of PbI_2.[86] It has been previously established that the emergence of the PbI_2 peak in $MAPbI_3$ is due to the combined effect of illumination and O_2.[87, 88] The photo-oxidative degradation of the $MAPbI_3$ surface involves iodide anions undergoing oxidation with the surrounding electron acceptor molecules (such as O_2) leading to the generation of superoxide free radicals followed by deprotonation of ammonium group, and eventually, evaporation of volatile species such as methylamine and iodine gas from the perovskite surface.[24, 89]

In the case of CO exposure, even in dark conditions, the PbI_2 peak is observed. This signifies that light illumination is not required for the interaction between CO and $MAPbI_3$ which leads to the decomposition of the perovskite. This is a significant difference from the effect of O_2 and indicates a strong interaction between CO and $MAPbI_3$. The XRD of the CO-exposed perovskite film, representative of diffraction by the bulk film material, does not exhibit the additional PbI_2 peak, confirming that the degradation of perovskite films for the given duration is limited to the top interface (Figure A2.1a). $MAPbI_3$ films stored in the N_2 atmosphere do not show the PbI_2 degradation at the top interface (Figure A2.1b).[90]

The effect of CO exposure under different conditions was further characterized by a Field emission scanning electron microscope (FE-SEM). Considering the naturally formed grooves on top of perovskite films representative of the grain boundaries, the as-fabricated films show an average grain size of 145 nm and the absence of pinholes (Figure 2.2b and Figure A2.2a). The duration of CO exposure, illumination condition, and presence of an external electric field heavily influence the grain size distribution (Figure 2.2c-h & Figure A2.2b-g) and morphology of the perovskite films. Exposure of the perovskite films to CO in dark for a short duration (1 hour) and without an electric field reduces the average grain size to 90 nm (Figure 2.2c and Figure A2.2b). The reduction in grain size is attributed to the interaction of CO with the perovskite interface leading to the formation of defects. On longer exposure (3 hours) under the same conditions, the average grain size increases slightly to 106 nm (Figure 2.2d & S2c). This occurs as continued degradation of the perovskite causes roughening of the surface and formation of striations (Figure 2.2d), which leads to the merging of the grains. On application of an external electrical field (applied bias of 2V) for 1 hour in dark and under a CO atmosphere, the striation pattern is even more pronounced (Figure 2.2e), and average grain size of 105 nm is observed (Figure A2.2d). The rearrangement of grains and formation of striations points to the

degradation of the $MAPbI_3$ surface due to strong interaction with CO and preferential loss of a particular component, MA, from the films leading to the formation of PbI_2 at the grain boundaries and on the top interface.[91] This is supported by the GIXRD results of Figure 2.2a as the MA^+ ions line up and the Pb^{2+} and I^- ions form a natural passage for CO molecules alongside the [0 0 1] axis (the c axis).[21] The CO molecules (kinetic diameter of 0.376 nm) may, therefore, easily infiltrate the 0.88 nm wide [0 0 1] passage and anisotropically erode the organic moiety across the perovskite film depth similar to the penetration of ambient moisture reported in earlier works.[92, 93]

A similar change in grain texture along with pitting and formation of PbI_2 is observed when CO exposure is performed under illumination. The effect is further enhanced in presence of an external electric field. When the perovskite films are exposed to CO for a 1-hour duration under light, besides striations, pitting and merging of the grains is observed. As a result, the average grain size of 318 nm is observed (Figure 2.2f and Figure A2.2e). Upon applying an external field under similar conditions, large pinholes accompanied by micrometer needle-like flakes start appearing over the perovskite surface and the average grain size enhances to 480 nm (Figure 2.2g and Figure A2.2f).[94, 95] Upon prolonged exposure (3 hours) to CO in light but in absence of an external field, the average grain size further increases to 520 nm (Figure A2.2g) and a separate phase with considerable contrast starts appearing (Figure 2.2h). This could be ascribed to the formation of bulk PbI_2. [96, 97]

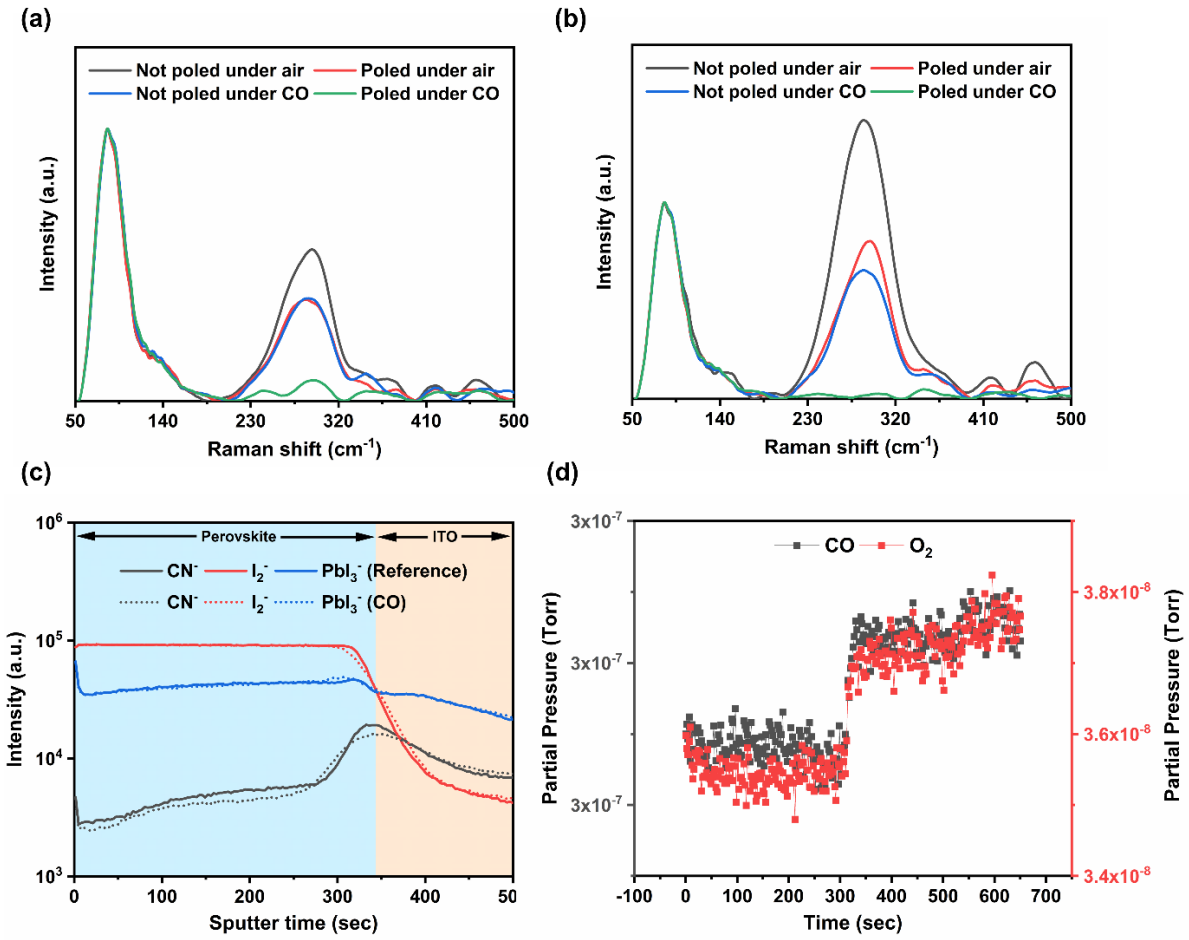

Figure 2.3 Raman Spectra of poled and unpoled $MAPbI_3$ films exposed to dry air and CO in (a) dark and (b) under light for 1 hour. (c) ToF-SIMS depth profile of pristine $MAPbI_3$ and perovskite films exposed to CO for 6 hours. (d) Gas analysis plot of perovskite film stored in CO atmosphere in a sealed beaker showcasing increase in partial pressure of O_2 and CO signals in comparison to the ambient atmosphere.

Raman spectroscopy was conducted to characterize the surface-sensitive interaction of CO over perovskite surface (Fig 2a&b). The sharp characteristic band at 85 cm^{-1} represents the Pb–I liberation mode and the broad band centered at 288 cm^{-1} is assigned to the MA^+ torsional mode of $MAPbI_3$. Under dark conditions (Figure 2.3a), the air-exposed $MAPbI_3$ films (1 hour) show a high-intensity Pb–I and MA^+ band with a relative intensity ratio of $I_{288}/I_{85} = 0.546$. The MA^+ band decreases on both, poling in air and exposure to CO, however, there are critical differences. On exposure to CO in dark (for 1 hour, without any electric field) the MA^+ band intensity decreases while the Pb–I band remains unchanged

leading to a decrease in I_{288}/I_{85} to 0.376. A similar effect is observed when the film is exposed to air and under poling (for 1 hour) where the I_{288}/I_{85} decreases to 0.371. A drastic change is observed when the film is exposed to CO and is also poled (for 1 hour) leading to an I_{288}/I_{85} of 0.07. This shows that in dark, CO has a strong interaction with the $MAPbI_3$ film and under prolonged exposure leads to the formation of PbI_2. This process is further accelerated in presence of an electric field. A similar trend is observed when the films are exposed to air and CO (with and without poling) in presence of 1.0 sun illumination (Figure 2.3b). To further ascertain that the degradation of the film is from the loss of the organic species due to its interaction with CO, and can proliferate across the whole film depth, Time of Flight Secondary Ion Mass Spectroscopy (ToF-SIMS) depth profiling was performed (Figure 2.3c). The depth profiling data reveals a reduced CN^- signal (representative of MA^+) across the depth of the perovskite film exposed to the CO atmosphere (6 hours). On the other hand, the PbI_3^- signal (due to the PbI_2 component) is maintained at the same level as that in the reference (pristine $MAPbI_3$) sample. The shape of the CN^- signal with an initial slow increase (after ~ 10 sec.) and rapid increase after 275 sec., is attributed to the effect of beam damage from both the primary beam (500 eV) and sputtering beam (30 keV).[98] The degradation of $MAPbI_3$ in presence of CO can follow multiple paths (see Appendix for Chapter 2). These can include interaction with reactive oxygen species that are known to form on the perovskite surface in presence of oxygen, and/or direct reaction between the CO and $MAPbI_3$. It is also possible that a limited loss of the organic moiety from the perovskite film on exposure to CO can be (partially) replenished by annealing the film in a methylamine vapor-rich atmosphere.

The strength of CO interaction with the $MAPbI_3$ and its ability to displace the adsorbed O_2 on the film surface was measured using a residual gas analyzer system equipped with a mass spectrometer. A $MAPbI_3$ film was initially exposed to dry air to adsorb O_2. Following that, the film was placed in a sealed quartz beaker in a CO-exclusive atmosphere. After 4 hours of equilibration, the gas in the sealed beaker was analyzed with the system. As seen in Figure 2.3d, the gas analysis shows an obvious signal from CO, but a rise in the O_2 signal is also observed. Control experiments conducted with a blank substrate without a $MAPbI_3$ film do not show such a rise in the O_2 signal (Figure A2.3a). Hence, the rise in the O_2 signal in the presence of $MAPbI_3$ film confirms that CO has a very strong interaction with the perovskite film surface and can displace the adsorbed O_2 leading to an increase in the corresponding signal intensity. To further verify this, a $MAPbI_3$ film exposed to air (for O_2 adsorption) was placed in the chamber in an N_2-exclusive atmosphere. After 4 hours of equilibration, upon analysis of the gas,

only a rise in the N_2 signal is observed (Figure A2.3b). The O_2 signal shows a decrease, further attesting to the strong interaction between CO and the $MAPbI_3$ surface.

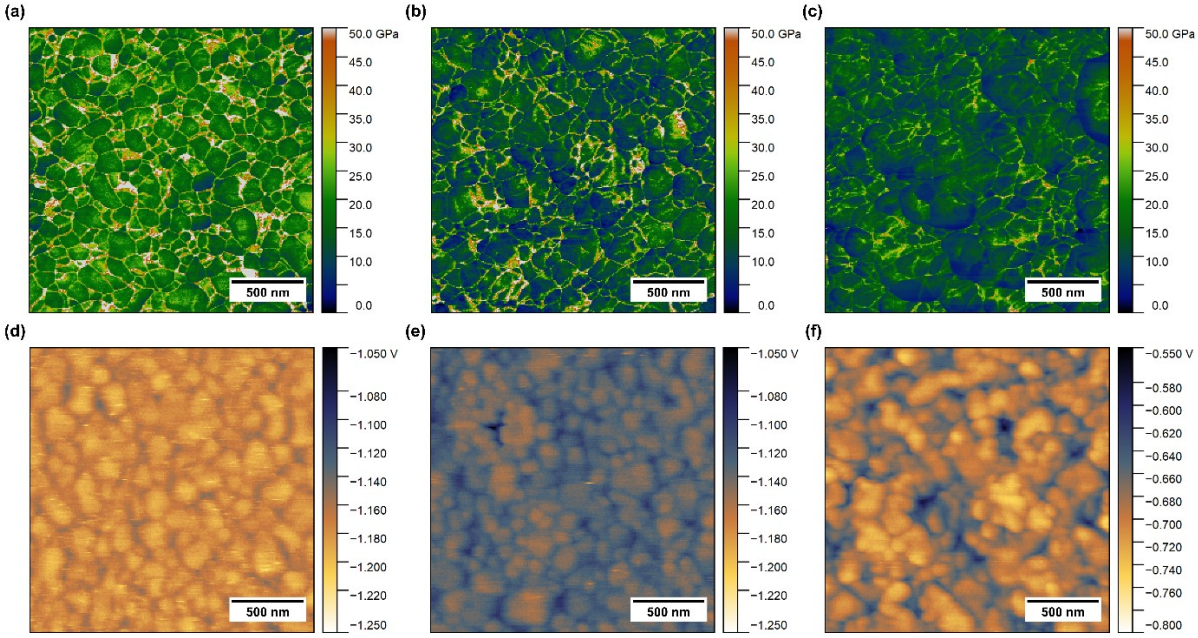

Figure 2.4 Young's modulus maps of (a) freshly prepared perovskite film and the film exposed to CO for (b) 6 hours and (c) 24 hours. Contact potential difference maps of (d) pristine $MAPbI_3$ and perovskite film exposed to CO for (e) 6 hours and (f) 24 hours.

The effect on mechanical properties of the $MAPbI_3$ films due to interaction with CO was characterized by mapping the surface modulus using the PeakForce Quantum Nanomechanical (PF-QNM) mode in an Atomic Force Microscope (AFM). The average modulus (23 GPa) observed for the pristine perovskite films (Figure 2.4a) is consistent with the previous reports.[99, 100] While the perovskite grains are softer with an average modulus value of 14.65 GPa, the grain boundaries are rigid with a higher modulus value of 25.5 GPa. On exposure to CO for 6 hours in the dark, significant changes in the film modulus are observed (Figure 2.4b). The average modulus of the film decreases to 17.5 GPa, and a significant contrast in modulus is observed across the film. Regions with low modulus (dark green) and some with significantly lower modulus (blue regions in Figure 2.4b) are observed. The low modulus regions indicate the formation of PbI_2 (elastic modulus of 17 GPa), while the extremely low modulus regions indicate the formation of striations as observed in the FE-SEM images in Figure 2.2.[101] Under prolonged CO exposure, the overall surface softens (12.6 GPa) as the PbI_2 present on the top interface

starts dominating the mechanical characteristics (dark green regions in Figure 2.4c).[102] Further, a much higher proportion of the very low modulus regions is observed (blue regions in Figure 2.4c).

The effect of the CO exposure was further characterized by Amplitude Modulated Kelvin Potential Force Microscopy (AM-KPFM). The contact potential difference (V_{CPD}) maps shown in Figure 2.4d-f can be used to calculate the work function of the perovskite surface (see details and Figure A2.4 in Appendix for Chapter 2).[103] The freshly prepared $MAPbI_3$ film exhibits an average work function of 4.70 eV (Figure 2.4d), indicating O_2 doping (p-type) of film in the ambient atmosphere.[104-106] After exposure to CO for 6 hours, the average work function lowers to 4.66 eV (Figure 2.4e). Prolonged exposure to CO (24 hrs) further lowers the work function to 4.25 eV (Figure 2.4f). Such lowering of the work function can be attributed to the combined effect of CO-driven desorption of O_2 molecules (as observed in Figure 2.3d) and the positively charged iodine vacancies at the PbI_2-rich top interface acting as n-type dopants.[107] Moreover, significant inhomogeneity is observed across the perovskite film as the surface roughness (height difference) increases over time with CO exposure (Figure A2.5a-c). The interfacial layer of PbI_2 rich n-type $MAPbI_3$ leads to the formation of a vertical p-n junction with the underlying p-type $MAPbI_3$ layer, which affects the electro-optical properties of the films as discussed below.[108]

The effect of CO on the electro-optical properties and polarization effects in perovskite films was studied in a lateral device configuration of Au/$MAPbI_3$/Au on Si/SiO_2 substrate, to avoid any interference from charge transport layers. The photocurrent response of the device in ambient conditions (referred to as reference) and under CO atmosphere under 1.0 sun illumination and 2V applied bias is shown in Figure 2.5a. The photocurrent under the CO atmosphere is 820 nA compared to 1306 nA under ambient conditions.

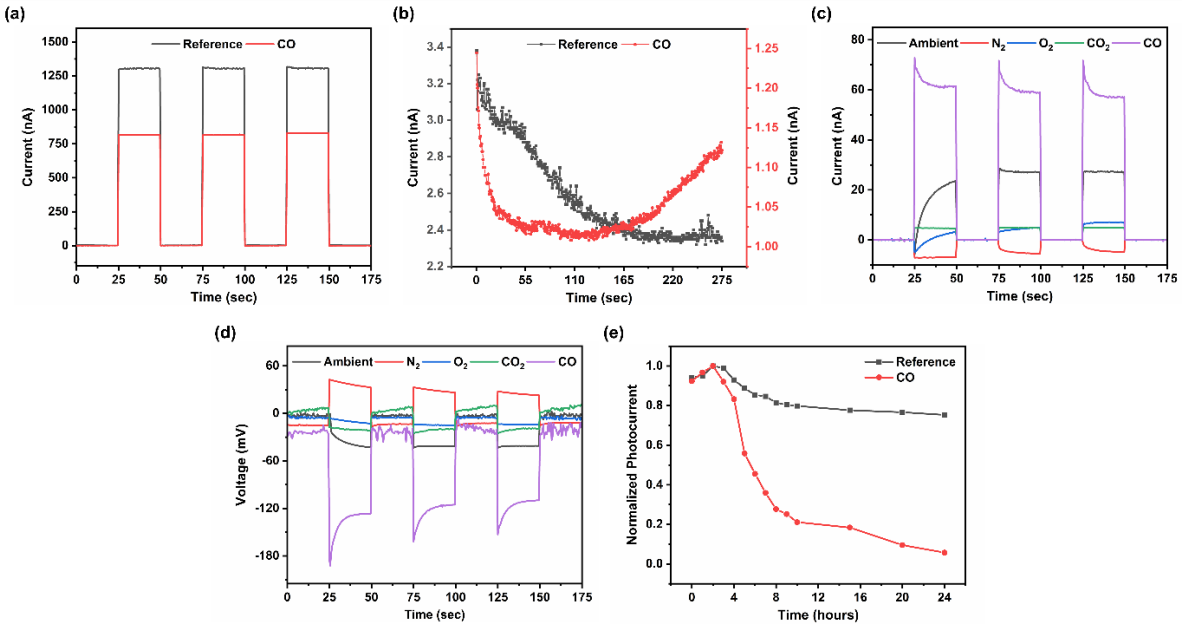

Figure 2.5 (a) Photocurrent and (b) dark current response of $MAPbI_3$ film exposed to the ambient (reference) and CO-exclusive atmosphere. (c) I_{sc} and (d) V_{oc} response of perovskite film measured in the ambient environment after being poled under various gaseous environments. (e) Normalized photocurrent observed for the devices aged continuously in ambient (reference) and CO atmosphere, in dark for 24 hours. The 0-25 sec., 50-75 sec., 100-125 sec., and 150-175 sec. cycles in (a), (c) and (d) represent the time duration when the device was in the dark while the 25-50 sec., 75-100 sec., 125-150 sec. cycles represent the time when the device was illuminated under air mass (AM) 1.5 global 1 sun.

The extent of decay in the dark current characterizes the ion migration effect in the perovskite films. Under external bias in dark, the mobile ions with low activation energy will drift toward metal electrodes. As the oppositely charged ions accumulate at the metal electrodes, the ion-induced electric field opposes the applied external field and hence, a transient decay in current is observed until the ion accumulation reaches an equilibrium condition.[109, 110] The initial dark current for the device in the CO atmosphere is 1.24 nA, which is lower than the 3.38 nA observed under ambient conditions (Figure 2.5b). With time, the current in ambient conditions decays monotonically to 2.36 nA. In contrast, the dark current for films under CO conditions decays rapidly to 1.03 nA within 55 sec., as seen in Figure 2.5b. This rapid decay in the perovskite films under the CO atmosphere is attributed to their higher density of ionic defects (which will affect the mobility and density of mobile ions). The dark current reaches a minimum value of 1.01 nA at 120 sec and then starts to increase in a monotonic fashion and

reaches 1.12 nA after 275 sec. This increase in dark current is attributed to the rapid degradation of the $MAPbI_3$ film under CO which leads to enhanced ion migration effects.[111]

Under both light and dark conditions, the current increases with external bias (*I-V* in Figure A2.6). The significantly lower dark currents initially observed under CO can be attributed to the formation of PbI_2 at the top surface and the grain boundaries. The large bandgap (2.3 eV) and higher activation energy required for ionic conduction (0.53 eV) in PbI_2, compared to $MAPbI_3$ (1.57 eV and 0.2-0.4 eV respectively), increase the activation energy for ion migration at the PbI_2 passivated perovskite grain boundaries.[112, 113] The formation of the PbI_2-rich top surface also reduces the photocurrent values under the CO atmosphere, due to its poor electro-optical properties.[114, 115]

An internal electric field is induced in $MAPbI_3$ films (in the lateral direction) on poling due to ion migration and polarization effects.[116, 117] Briefly, as explained above, due to applied external field (bias) MA^+ and I^- ions migrate to oppositely charged metal electrodes. This leads to the formation of ion depletion regions in the perovskite film and the generation of an internal field (formation of a lateral p-n junction). The direction of this internal field (from the ion migration effect) is opposite to the applied field during poling. Subsequently, the charge carriers generated upon illumination are separated by the induced electric field leading to short-circuit current (I_{sc}) and open-circuit voltage (V_{oc}), forming the basis of self-powered devices.[118] In the case of polarization effects, however, the resulting V_{oc} is of the same polarity as that of the poling bias (field) due to the formation of a charge compensating layer at the metal electrodes (because of the free electrons in the metal).[59] Both ion migration and polarization effects may exist simultaneously in the perovskite film and either one may dominate based on the poling conditions. The reversal of the sign observed for I_{sc} and V_{oc} distinguishes between the dominance of the respective effects.

Improving the power capacity of self-powered perovskite devices (based on ion migration and polarization effects) through simple methods is crucial for expanding their application and performance.[119] Based on the effect of CO on the $MAPbI_3$ films, we show its ability to enhance the I_{sc} generation in these films by ~122% on poling in dark. Figure 2.5c and d show the I_{sc} and V_{oc} behavior of these films in an Au/$MAPbI_3$/Au lateral device after poling under different gases in the dark and measuring in ambient conditions. Poling was done in all the cases for just 5 minutes at 2V in dark to limit degradation in the films. Post CO poling, the device shows a stable I_{sc} and V_{oc} of ~60 nA and -110 mV, respectively. While post CO_2 poling, the I_{sc} value reaches ~4.9 nA while the V_{oc} is -19.5 mV.

For the films poled in ambient conditions and O_2, the I_{sc} settles to a final value of 27 nA and 7 nA while the V_{oc} values reach -41 mV and -14 mV, respectively. However, under both these conditions, the initial I_{sc} is negative, and slowly over the first cycle changes sign to positive. Post poling in N_2, the I_{sc} is negative and gradually decreases over the course of 3 cycles from an initial value of -7.1 nA to -4.8 nA. The corresponding V_{oc} reduces from 42.6 mV (1st cycle) to 22.8 mV by the end of the 3rd cycle.

This difference in both the magnitude of I_{sc} and V_{oc} and its change in sign reflects differences in interaction between the $MAPbI_3$ film and CO, compared to other gases. The previously discussed characterization results show the strong interaction between CO and $MAPbI_3$ and are the basis of this improved I_{sc} performance. Specifically, we note that among all the gases CO has a strong dipole and leads to the rapid formation of PbI_2 in these films.[120] Hence, positive I_{sc} is maintained across all cycles similar to that observed in CO_2 exclusive atmosphere representing the dominance of the polarization effect. In comparison, the I_{sc} changes direction and gradually turns from negative to positive in O_2 exclusive and ambient atmosphere. This suggests that the polarization effect eventually dominates over the ion migration, as the ions that previously diffused under the influence of applied bias (poling) begin to re-homogenize. The negative I_{sc} in the N_2 exclusive atmosphere suggests that the ion migration effect dominates over the polarization effect for a longer time.

Due to the limited poling duration only the formation of a thin top layer of PbI_2 is expected, along with its possible formation at the grain boundaries. This is supported by the GIXRD data and the significantly reduced dark and ionic current observed in the CO-exposed films. Based on the band structure of $MAPbI_3$ and PbI_2 two effects can lead to the enhancement in the I_{sc} performance: (1) the formation of type I semiconductor junctions between $MAPbI_3$ and PbI_2 passivated grain boundaries will limit the recombination at defect sites and hence improve the I_{sc} performance.[121, 122] (2) the top layer of PbI_2 rich $MAPbI_3$ (n-type) forms a vertical p-n junction with the underlying p-type $MAPbI_3$ layer.[123] Under short-circuit conditions, the photogenerated charge carriers within this junction will be effectively separated and contribute to I_{sc}.

Short duration exposure to CO, therefore, improves the self-powered performance of $MAPbI_3$ films due to the formation of a limited amount of PbI_2. Such improved performance with a limited amount of PbI_2 has been previously reported for $MAPbI_3$ solar cells.[124-126] However, prolonged exposure which leads to large-scale degradation of the $MAPbI_3$ films into PbI_2 is detrimental to the device's performance.[127-129] This can be seen in the photocurrent response of Figure 2.5e. The photocurrent response of the

$MAPbI_3$ films is reduced to 55.8% within 5 hours and 5.7% within 24 hours as the perovskite film suffers accelerated degradation to PbI_2 due to interaction with CO. In comparison, the reference perovskite film stored in ambient and under dark conditions maintains 75.2% of its performance even after 24 hours.

2.4 Conclusions

In conclusion, it has been established that CO gas molecules interact with the top interface of $MAPbI_3$ film, facilitate O_2 desorption, and induce considerable changes in its inherent physicochemical properties and energy level alignment. A short exposure of the perovskite films to CO induces n-type doping at the top interface, while longer exposure leads to MA^+ deficient and PbI_2 rich phase across the depth of the entire film. The stoichiometric change across the perovskite films leads to the generation of an internal electric field in the film near the top interface due to the formation of a vertical p-n junction. On illumination, this leads to more effective charge carrier separation under short-circuit conditions. Moreover, the passivation of defects and trap states at the perovskite grain boundaries by the PbI_2 initially results in reduced ion migration. However, continuous exposure to CO results in significant deterioration of electro-optical performance following the destruction of the inherent perovskite structure. This is due to the increased degradation of $MAPbI_3$ and excessive formation and phase segregation of the PbI_2 phase in bulk. The presence of PbI_2 is no longer restricted at the grain boundaries and top surface and instead spreads out across the entire perovskite film forming a relatively insulating barrier. This prevents the flow of electronic current and reduces overall electro-optical performance. Such observations also call for deeper studies of the all-inorganic lead-halide counterparts to research if similar CO-induced degradation is observed. Irrespective, understanding the changes induced by CO molecules at the perovskite interface calls for precise CO exposure protocols and research into the interaction of perovskites with other gases that may be present in limited concentrations.

Chapter 3

Hydrophobic-Hydrophilic Block Copolymer Mediated Tuning of Halide Perovskite Photosensitive Device Stability and Efficiency

3.1 Introduction

Halide perovskite-based photosensitive devices are being actively researched in the photovoltaic world amid the power conversion efficiency of the perovskite-based single junction solar cells reaching beyond 25%.[130] The low-cost solution-processibility along with excellent electro-optical characteristics, lightweight, and mechanical flexibility has led to perovskite photosensitive applications to reach beyond conventional solar cells to LEDs, display devices, sensors, and self-powered devices.[84] Despite the success in achieving high efficiency, the stability issues of halide perovskites in the ambient atmosphere serve as the toughest challenge to the commercial viability of these devices.[131] To address the degradation issues, polymer additive engineering has been realized as a facile way of fabricating high-quality perovskite films with improved stability without compromising the performance of photoactive devices.[132] The perovskite grain boundaries and interface primarily serve as trap states for recombination.[133] These further act as the preferred site for the leaching of moisture and interaction with external degradation factors.[134] Due to their high molecular weights, the polymers do not evaporate during the annealing of the perovskite films and can effectively passivate the defect centers present at the grain boundaries and interface of the perovskite film.[135] In addition, the presence of polymer can alter the crystallization kinetics and retard the growth of perovskite grains leading to alteration in the grain size.[136, 137] Over the years, several research groups have attempted to utilize polymers containing atoms or functional groups with the potential of interacting with perovskite precursors. Several works have been reported using different polymer additives such as polystyrene (PS), polyethylene glycol (PEG), polymethyl methacrylate (PMMA), polyethylenimine (PEI), and polyvinylpyrrolidone (PVP) which inherently differ not only in terms of their hydrophobicity but also in the interaction mechanism with the perovskite precursors owing to the difference in polarity.[37, 119, 138-144] Hence, owing to such contrasting nature of the different polymer additives, there is a need to understand the characteristics of the polymer that are important for achieving stable perovskite-polymer composite films without compromising the device performance. In this regard, block copolymer additive systems can be useful systems for establishing the influence and dominance of each individual polymer component.[145-152]

The current work henceforth aims to utilize the strong interaction capabilities of the hydrophilic and polar PEG, and hydrophobic non-polar PS polymers in a PEG-PS block copolymer system to better understand the effective contribution of each polymer when mixed alongside perovskite precursors. We systematically show that while the presence of the polymer additive either as a homopolymer or as a block copolymer does not interfere with the inherent perovskite phase, it does affect the microstructural evolution of the $MAPbI_3$ grains. It has been observed that the presence of PEG and PS leads to reduced ion migration and defect sites due to the passivation of grain boundaries and device interfaces. While the presence of PS enhances the average grain size, in contrast, the presence of just PEG increases heterogeneous nucleation within the perovskite films leading to an enhanced density of grain boundaries and trap sites and proving insufficient to reduce ion migration. Among the polymer-perovskite composite films, the 36 PS-b-1.4 PEG copolymer additive effectively enhances the photocurrent to 1420 nA in comparison to 957 nA observed in pristine $MAPbI_3$. Moreover, it maintains 80% performance over 7 days. Another critical observation is the limitation of achieving long-term ambient atmosphere stable films in absence of the hydrophobic PS counterpart.

3.2 Experimental Section

3.2.1 Synthesis of perovskite precursor solution

A 1.35 M pristine $MAPbI_3$ solution was prepared by mixing 79.4 mg of methylammonium iodide (>99.99%, Greatcell Solar Materials) and 230.5 mg of lead iodide (>99.999% trace metals basis, Sigma-Aldrich) in 53.3 µL of dimethyl sulfoxide (anhydrous, ≥99.9%, Sigma-Aldrich) and 317.5 µl of N, N-dimethylformamide (anhydrous, 99.8%, Sigma-Aldrich). To fabricate PS-$MAPbI_3$ film, a previously optimized concentration of 1 wt/v % of 35 kDa P was introduced in the perovskite precursor solution separately. An optimized concentration of 1×10^{-4} wt/v % of different polymers (21.5 PS-b-20 PEG, 36 PS-b-1.4 PEG, and 35 kDa PEG; Polymer Source) was used to prepare the rest of the polymer-perovskite precursor solutions. The PDI value for the 35kDa PS, 21.5 PS-b-20 PEG, 36 PS-b-1.4 PEG, and 35 kDa PEG polymers was 1.02, 1.09, 1.02, and 1.08 respectively. The solutions were later stirred on a magnetic stirrer to allow sufficient interaction, before spin-coating in the ambient atmosphere.

3.2.2 Fabrication of perovskite-based samples for electro-optical characterization

To understand the influence of individual contribution of PS and PEG polymers in the co-polymer system and also, independently over the optoelectronic properties of the resultant perovskite-polymer

composite films, planar lateral devices with $MAPbI_3$ (or polymer-$MAPbI_3$) sandwiched between gold (Au) electrodes, were fabricated. The typical fabrication involved spin coating of respective precursor solutions over Si/SiO_2 chips with gold electrodes being 200 μm apart (Au chips). The Au chips were sequentially washed and ultrasonicated in Millipore water, acetone, and isopropanol for 10 minutes each. After re-washing with Millipore water and drying with N_2, the Au chips were treated with UV Ozone to remove organic moieties. The precursor perovskite solution was then spin-coated on the cleaned chips at 4000 rpm for 30 seconds. After 6-8 seconds of rotations, 200 μl of diethyl ether was dropped over the continuously rotating films to remove excess solvents. The spin-coated films were ultimately annealed stepwise at 65 ºC for 2 minutes and 100 ºC for 3 minutes to ensure complete perovskite phase formation.

3.2.3 Structural, microscopic, spectroscopic, and contact angle characterization

The X-ray diffraction (XRD) was characterized using PANalytical Empyrean diffractometer with Cu Kα radiation (λ = 1.54 Å). A Zeiss Ultraplus field emission scanning electron microscopy (FE-SEM) equipped with energy-dispersive X-ray spectroscopy (EDX) was used to examine the surface topology and average grain size distribution in the pristine and polymer integrated perovskite films. All Raman spectra were recorded with 6 mW power at an excitation wavelength of 532 nm using a Horiba HR800 spectrometer in a backscattering configuration. The time-of-flight ion mass spectroscopy was performed to analyze depth profiling of freshly prepared perovskite and polymer-perovskite films using Cs^+ ion source (500 eV) for sputtering and Bi^{3+} (30 keV) for analysis over ToF-SIMS 5, ION-ToF GmbH. The contact angles were measured using a standard automated contact angle goniometer (Rame-Hart, Model 190 CA) with deionized water.

3.2.4 Electrical measurements

The electrical measurement on the planar lateral device configuration of Au/$MAPbI_3$ (polymer-$MAPbI_3$)/Au photodetector was conducted using a probing station. A two-probe method was employed by connecting a single probe to one of the gold electrodes and the other probe was grounded to the second gold electrode. A Keysight 6614C 50-Watt system power supply was used for applying an external voltage. For carrying out electro-optical measurements of the pristine and polymer-perovskite photodetector device, an external bias of 2 V was applied. The current-voltage (*I-V*) characteristics, photocurrents, and dark currents were sequentially measured using a Keysight 3458A Digital multimeter. The perovskite film was connected in series with the multimeter and power supply to

complete the circuit. Simulated AM 1.5 global irradiation (100 mW cm^{-2}) was generated using a Xenon-lamp based solar simulator (Newport Oriel Instrument 67005, 150 W Solar Simulator). An NREL calibrated KG5 silicon reference cell was used to calibrate light intensity to minimize any spectral mismatch. All measurements were conducted in ambient conditions. The long-term stability test of the devices was tested by directly exposing the devices to an ambient atmosphere under room light with 35−40% relative humidity. The humidity was measured by a portable relative humidity sensor.

3.3 Results and Discussion

The schematic in Figure 3.1a represents the chemical structure of PS, PS-b-PEG, and PEG. To understand the effect of the individual contribution of each constituent polymer in a block copolymer additive system, two PS-b-PEG polymers with different individual chain length contributions (21.5 PS-b-20 PEG and 36 PS-b-1.4 PEG), were utilized to prepare the polymer-perovskite films (details in Appendix of Chapter 3). This was also coupled with the use of homopolymers of PS and PEG to make the perovskite samples. The X-ray diffraction (XRD) pattern shown in Figure 3.1b confirms that the addition of either of the polymers independently or as the block copolymers in the perovskite film does not alter the tetragonal phase of $MAPbI_3$. The dominant peaks of (1 1 0), (2 2 0), and (3 1 0) lattice planes are evident with the absence of any obvious impurity phase. Owing to its hydrophilic nature, utilization of excessive PEG (1 wt/v %) leads to degradation of the perovskite phase with a noticeable PbI_2 impurity phase (see XRD pattern and SEM image in Figure A3.1a-b). The FE-SEM images (Figure 3.1c-g) of the polymer-perovskite films show that the incorporation of PS and PEG in the perovskite matrix leads to modulation of the nucleation and the growth rate of crystal grains.[153] This can be attributed to the direct interaction of PS and PEG chains with $MAPbI_3$ precursors. The average grain size observed in pristine $MAPbI_3$ is 120 nm (Figure 3.1c and Figure A3.2a) which reduces to 70 nm in 35 kDa PEG-$MAPbI_3$ film (Figure 3.1d and Figure A3.2b) owing to increased heterogeneous nucleation in the PEG-perovskite film leading to enhanced grain boundaries and trap & defect sites.[154] The addition of PS as a copolymer and also as a homopolymer leads to a progressive trend in the average grain size as its value increases from 108 nm in 21.5 PS-b-20 PEG-$MAPbI_3$ films (Figure 3.1e and Figure A3.2c) to 190 nm in 36 PS-b-1.4 PEG-$MAPbI_3$ (Figure 3.1f and Figure A3.2d). The largest grain size of 195 nm is observed in the 35 kDa PS-$MAPbI_3$ film (Figure 3.1g and Figure A3.2e)

suggesting that the presence of PS modulates crystallization kinetics favorably to allow improved grain growth.

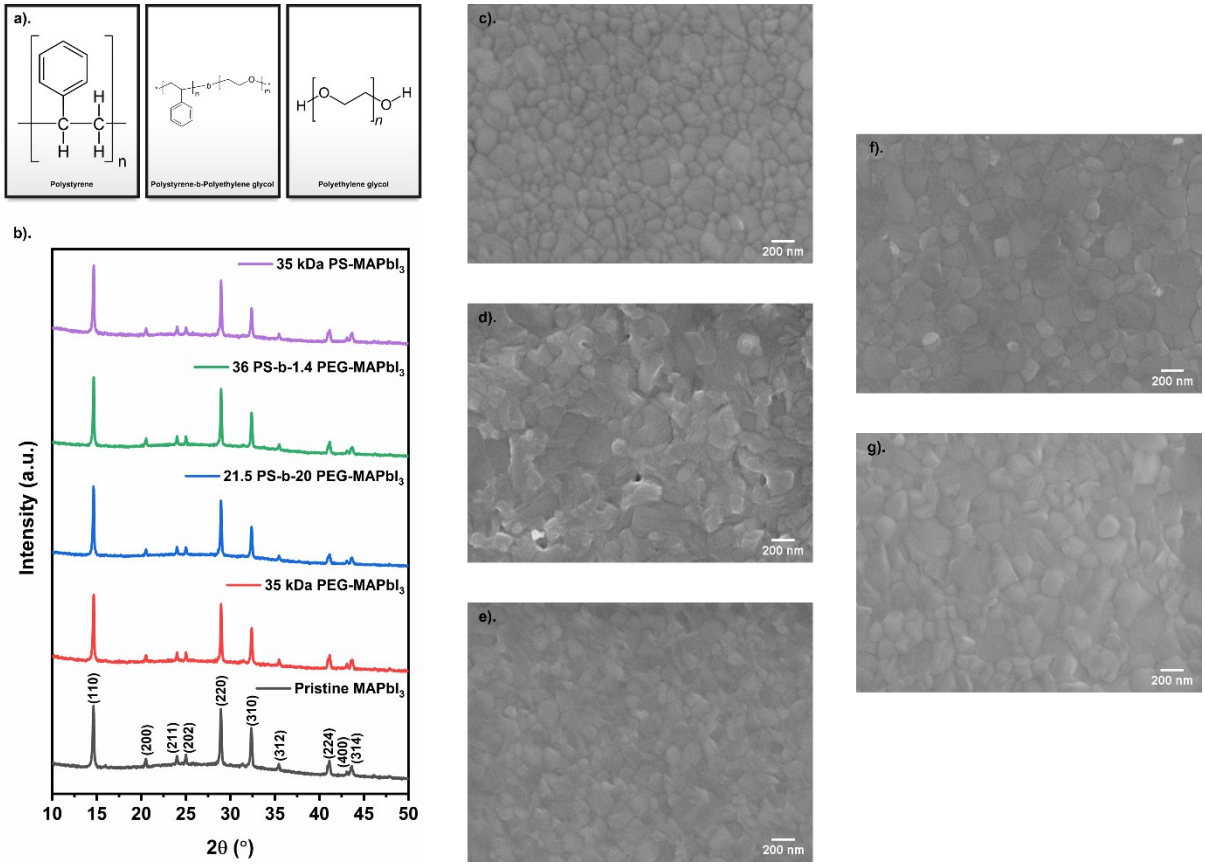

Figure 3.1 (a) Structure of polystyrene (PS), polystyrene-b-polyethylene glycol (PS-b-PEG), and polyethylene glycol (PEG). XRD pattern of pristine and polymer-perovskite films. Scanning electron micrographs of (c) pristine $MAPbI_3$ and polymer-perovskite films made with (d) PEG, (e) 21.5 PS-b-20 PEG, (f) 36 PS-b-1.4 PEG and (g) PS as additives. Here, the naturally formed grooves on top of perovskite films have been considered representative of grain boundaries.

The specific molecular-level interaction between perovskite precursors and polymer additive was characterized by Raman spectroscopy. The pristine $MAPbI_3$ and polymer-$MAPbI_3$ films exhibit sharp characteristic peaks of Pb–I cage at 74, 95, and 110 cm^{-1}, and a broad torsional mode corresponding to organic cations between 160-260 cm^{-1}, as seen in Figure A3.3a. As observed in Figure A3.3b, the Pb–I liberation mode shifts to a higher wavenumber with the inclusion of increasing PS content in the copolymer system and also as a homopolymer. Typical cation-π interaction between MA^+ and PS chains

also leads to variation in MA^+ modes in the polymer-$MAPbI_3$ films (Figure A3.3c). Such variation in perovskite's Raman active modes signifies an enhanced molecular-level interaction between polymer and perovskite precursors which forms the basis of the inclusion of a polymer in the perovskite layers. The interaction between PS and the perovskite precursors has been previously confirmed by gel permeation chromatography and the growth of single perovskite crystals.[37, 75] On the other hand, spectroscopic techniques have been effectively utilized to demonstrate the coordination of the lone pair of -O in PEG with Pb^{2+} ions.[155] Further, the upshift in NH^{3+} and MA^+ peak in ^1H nuclear magnetic resonance data indicating strong hydrogen bond interaction between the oxygen atom of PEG and MAI precursor has been previously reported in the literature.[35] The strong interaction of the polymer additives with perovskite precursors leads to interfacing between the polymer chains and perovskite phase at the grain boundaries in the resultant polymer-perovskite films.

To ascertain the presence of polymer additive across the depth of the perovskite film, Time of Flight Secondary Ion Mass Spectroscopy (ToF-SIMS) depth profiling was performed (Figure 3.2). The C_2H^- and O^- signals are representative of PS and PEG respectively. The corresponding first derivative curves of C_2H^- and O^- signals with respect to the normalized depth of the perovskite film are presented in Figure A3.4a and Figure A3.4b. The $In_2O_2^-$ signal arising from the indium tin oxide (ITO) substrate shows a sudden increase at ~300 sputtering sec in all samples signifying that the sputtering beam has reached the substrate. The O^- signal (due to ITO) in the pristine $MAPbI_3$ (Figure 3.2a) and PS-$MAPbI_3$ films follows the trend of the $In_2O_2^-$ signal and is confined to the substrate. While in the $MAPbI_3$ films with PEG, the O^- signal due to PEG can be observed at the top and bottom interface and across the whole film. Hence, the O^- signal from PEG can unambiguously be distinguished from the $In_2O_2^-$ (representative of ITO substrate exclusively). The depth profiling data reveals a high intensity of the C_2H^- signals in the PS-containing samples (Figure 3.2c, Figure 3.2d, and Figure 3.2e) across the whole film and an even higher intensity at the top and bottom interface. This signifies that PS chains are incorporated across the whole perovskite film and further are preferentially located at the top and bottom interfaces(Figure A3.4a).[119] The O^- signal in the PEG-$MAPbI_3$ film is higher across the whole film (Figure 3.2b, compared to pristine perovskite film). However, unlike the preferential accumulation of the PS signal at the top and bottom interface, the intensity of the PEG signal is high only at the bottom interface (Figure A3.4b). This can be accredited to the difference in mobility of the PS and PEG polymer chains, the strength of interaction with the perovskite precursors, and the adherence of polymer chains to the substrate during spin coating. This signifies that PEG as a homopolymer is distributed

uniformly across the whole perovskite film, with preferential accumulation at the bottom interface. In the block copolymer-$MAPbI_3$ films (Figure 3.2c and Figure 3.2d), while the distribution of PS and PEG is observed across the whole perovskite film, now not just PS but also PEG has a higher concentration at both the top and bottom interfaces. This is expected as the PS and PEG are now covalently linked and the accumulation of PS chains at the top interface is also accompanied by that of the PEG chains. It also signifies that the PS has a strong structural influence on the block-copolymer-$MAPbI_3$ films and can alter the distribution of the PEG (Figures S4a and S4b).

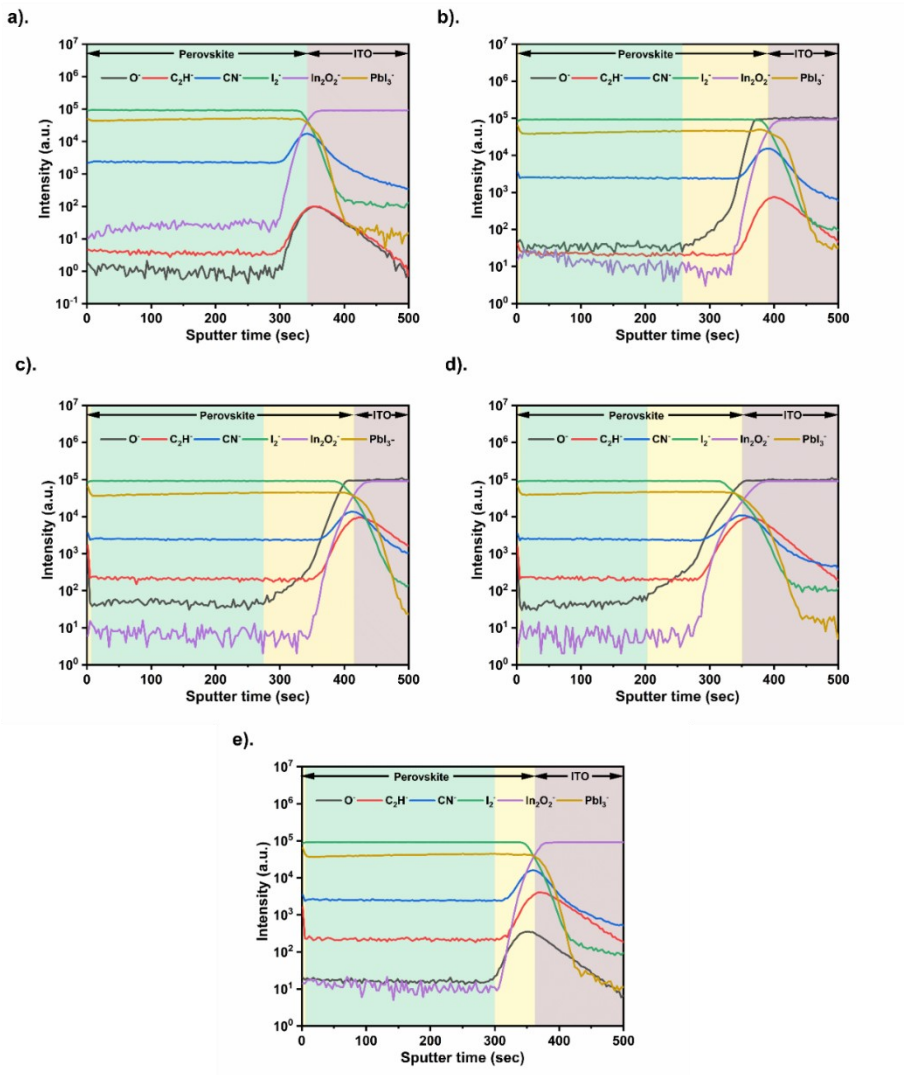

Figure 3.2 ToF-SIMS plots of (a) pristine $MAPbI_3$ and polymer-perovskite films made with (b) PEG, (c) 21.5 PS-b-20 PEG, (d) 36 PS-b-1.4 PEG and (e) PS as additives.

The ambient atmosphere stability serves as a critical factor in the long-term operation of the perovskite-based devices.[156] Hence, contact angle measurements were utilized to assess the hydrophobicity of the pristine $MAPbI_3$ and perovskite-polymer composite films to determine their ability to survive in ambient moisture. The contact angle (Figure 3.3) and thus the hydrophobicity of the polymer-perovskite films was observed to increase in the following order: 35 kDa PEG (56.05°) < Pristine $MAPbI_3$ (60.1°) ≈ 21.5 PS-b-20 PEG (61.6°) < 36 PS-b-1.4 PEG (66.7°) < 35 kDa PS (76.7°). The contrasting hygroscopic and hydrophobic nature of PEG and PS respectively can ascribe to such observation. Although the good solubility of the PEG polymer in a polar solvent can be advantageous in spreading the precursor solution leading to even coverage of perovskite film over the bare substrate, there is also a trade-off as its hydrophilic nature limits the ambient atmosphere stability of the prepared perovskite-polymer films.[157, 158] In contrast, the improved contact angles in the perovskite films with the presence of PS additive suggest that its hydrophobic nature dominates and can effectively provide a barrier function for perovskite film to suppress moisture invasion.

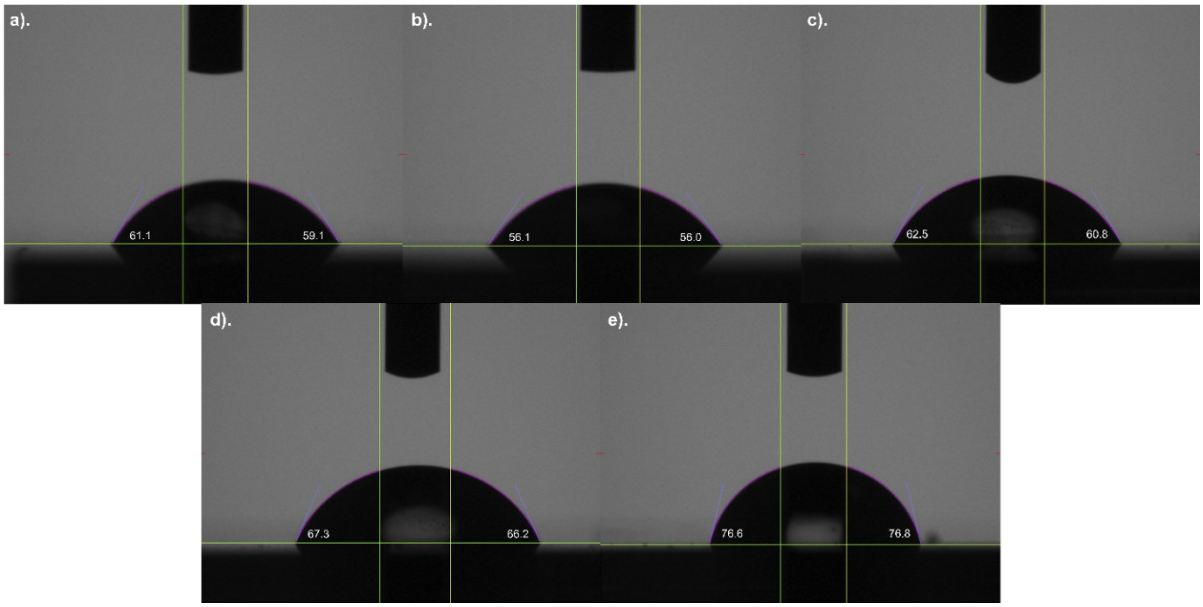

Figure 3.3 Contact angle images of (a) pristine $MAPbI_3$, (b) PEG-$MAPbI_3$, (c) 21.5 PS-b-20 PEG-$MAPbI_3$, (d) 36 PS-b-1.4 PEG-$MAPbI_3$ and (e) PS-$MAPbI_3$.

The effect of polymer additives on the electro-optical properties and polarization effects in perovskite films was studied in a lateral device configuration of Au/$MAPbI_3$/Au on Si/SiO_2 substrate without any charge transport layers. The photocurrent response of the pristine $MAPbI_3$ device in ambient conditions

and polymer-perovskite devices under 1.0 sun illumination and 2V applied bias is shown in Figure 3.4a. The average photocurrent of the pristine $MAPbI_3$ device is 957 nA which enhances with the integration of polymer in the polymer-perovskite composite films. While the 35 kDa PEG-$MAPbI_3$ film shows a photocurrent of 1282 nA, the current increases for the 21.5 PS-b-20 PEG-$MAPbI_3$ films to 1375 nA and 1420 nA in the 36 PS-b-1.4 PEG block copolymer perovskite hybrid film. The insulating nature of PS leads to a drop in photocurrent to 1291 nA in the 35 kDa PS-$MAPbI_3$ film. The extent of decay in the dark current directly represents the magnitude of the ion migration effect in the perovskite films (Figure 3.4b). Under external bias in dark, the mobile MA^+ and I^- ions with low activation energy drift towards metal electrodes. As the oppositely charged ions accumulate at the metal electrodes, an ion-induced electric field is generated in the opposite direction of the applied external field. Hence, the competing fields lead to a transient decay in the overall current until the ion accumulation reaches an equilibrium condition. The pristine $MAPbI_3$ shows the highest ionic current starting at 8.5 nA which rapidly decays by 20% to 6.8 nA within 10 seconds. PEG is used as an ionic conductor in battery electrolytes.[159-161] It is hence not surprising to note that the PEG-$MAPbI_3$ films show an increase in ionic current over time as the dark current value starts at 5.4 nA and ends at 5.6 nA. On the contrary, the magnitude of ionic currents progressively decreases in the polymer-perovskite films with an increase in PS chains owing to its poor ionic conductivity. The minimum dark current of 2.2 nA is exhibited in PS-$MAPbI_3$ which steadily decreases to 1.6 nA after 24 seconds. Despite exhibiting a lower average photocurrent, the significant reduction in ionic current (Figure A3.5) leads the 35 kDa PS-$MAPbI_3$-based film to achieve the highest light switching ratio (Figure A3.6).

Owing to the combined effects of the electric field poling that leads to polarization in the perovskite films and the inherent semiconducting nature of $MAPbI_3$, upon illumination, a self-powered response is observed in these films.[162] Subsequently, once the external bias is removed, the charge carriers generated upon illumination can be separated by the induced electric field leading to the observance of short-circuit current (I_{sc}) response and the open-circuit voltage (V_{oc}) in the pristine $MAPbI_3$ and polymer-perovskite films (Figure 3.4c and Figure 3.4d). Similar to the photocurrent response, Isc and Voc values increase sequentially for the pristine $MAPbI_3$, 35 kDa PEG, 21.5 PS-b-20 PEG-$MAPbI_3$, 36 PS-b-1.4 PEG-$MAPbI_3$, and 35 kDa PS-$MAPbI_3$ film (Figure A3.7). The best Isc (100 nA) and Voc (130 mV) are observed for 35 kDa PS-$MAPbI_3$ as it exhibits more than 2.5-fold enhancement with respect to the pristine $MAPbI_3$ (30 nA and 52 mV, respectively). Degradation in perovskite films results from two primary factors, the first from exposure to environmental elements such as oxygen and

moisture and the second due to internal degradation via ion migration. Upon exposing the as-fabricated films to an ambient atmosphere for a week in dark, the normalized photocurrent in pristine $MAPbI_3$ reduces to 81% within a day and 30% within 7 days (Figure 3.4e). It has been previously hypothesized that in presence of a humid environment, although perovskite undergoes hydrolysis, moisture may be soaked by the surrounding PEG molecules and PbI_2 and MAI may recombine in-situ to form $MAPbI_3$.[163] However, the rapid decay of device performance to 81% within 2 days in the PEG-$MAPbI_3$ device suggests otherwise. On the contrary, the 36 PS-b-1.4 PEG-$MAPbI_3$ and PS-$MAPbI_3$ films maintain 80% of their initial performance until 7 days. It can be seen that the presence of PEG in the block copolymer governs the initial decay pattern in the performance. The top PS (hydrophobic)-rich layer is crucial for acting as a barrier against oxygen and moisture, while the density of grain boundaries in the perovskite-rich layer determines the ion migration effects.[74] As a result of the combined effect of these two factors and consistent with the electro-optical performance, the best stability is observed for PS-rich films.

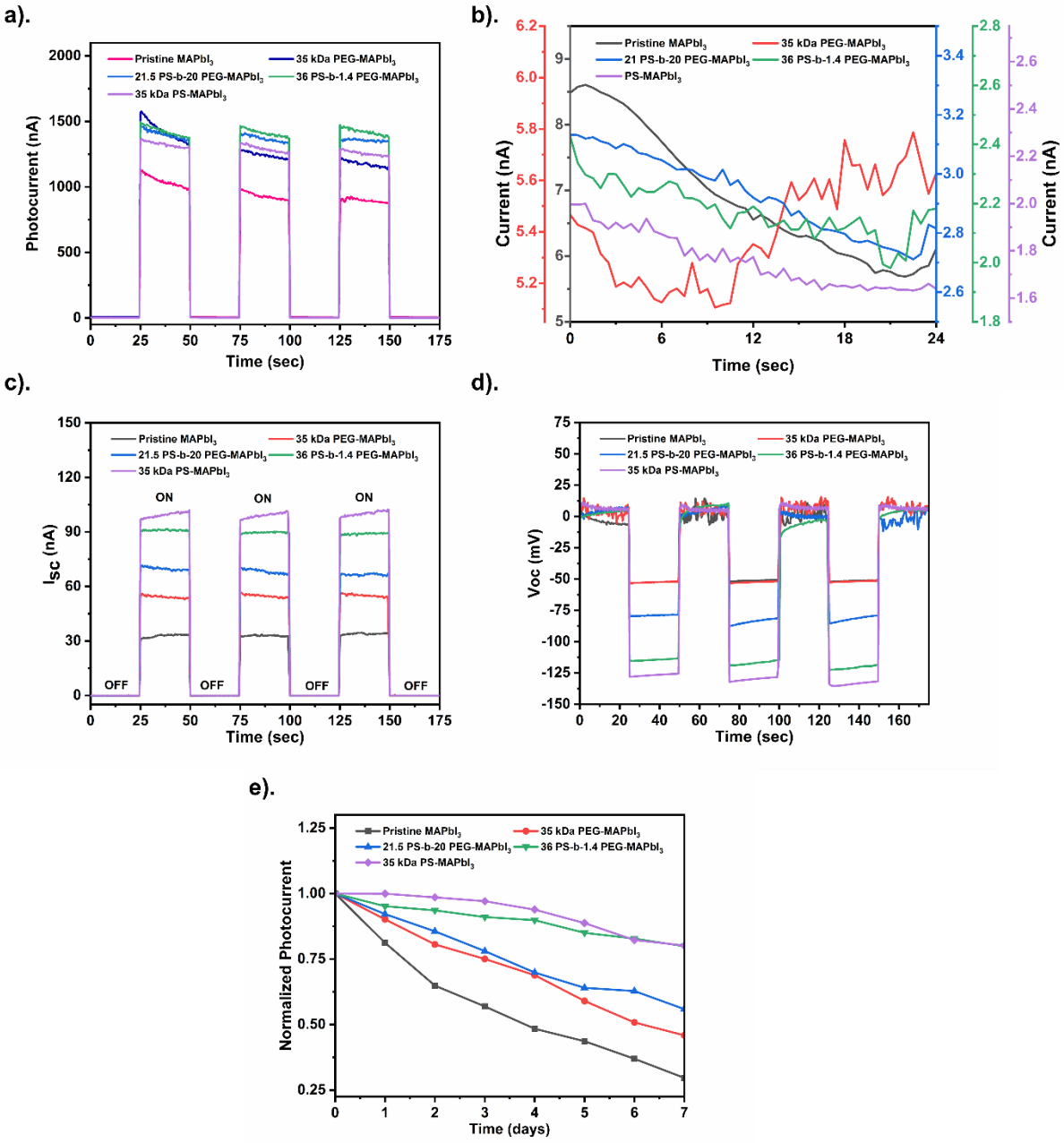

Figure 3.4 (a) Photocurrent, (b) dark current, (c) short-circuit current (Isc), (d) open-circuit voltage (Voc) plots of pristine and polymer-perovskite photodetector devices. (e) Operational stability of the as-fabricated pristine and polymer-perovskite composite films in terms of their photocurrent.

3.4 Conclusion

In conclusion, the current work presents a detailed investigation of integrating hydrophobic and hydrophilic polymer additives in form of both homopolymer and also as block copolymer with perovskite films. Their difference in chemical structure (leading to hydrophobic vs hydrophilic nature) and interaction with perovskite components leads to critical differences in the respective polymer-perovskite films. The structural differences in the films are observed in the results from ToF-SIMS where the polymer distribution changes across the films. As a result, the electro-optical performance and stability of the films are affected. The hydrophobic polymer integrated perovskite devices PS-$MAPbI_3$, 36 PS-b-1.4 PEG-$MAPbI_3$, and 21.5 PS-b-20 PEG-$MAPbI_3$ outperform hydrophilic polymer-perovskite (PEG-$MAPbI_3$) and pristine $MAPbI_3$ devices and exhibit high photocurrent, lower dark currents, and relatively higher stability. The PS-$MAPbI_3$ device exhibits a photocurrent of 1291 nA and a reduced dark current value of 1.6 nA, respectively. The hydrophobic nature of PS enables prevention against moisture seepage in the ambient atmosphere as the 36 PS-b-1.4 PEG-$MAPbI_3$ and PS-$MAPbI_3$ photodetector maintain 80% of its initial device performance. The discussed facile copolymer additive strategy involving polymers of contrasting nature will serve as a strong foundation for effective tuning and careful selection of polymers for developing polymer-perovskite thin films based on portable optoelectronic devices such as LEDs, solar cells, photodetectors, and self-powered applications.

Chapter 4
Nanoscale Architecture of Polymer-Organolead Halide Perovskite Films and the Effect of Polymer Chain Mobility on Device Performance

4.1 Introduction

Polymer incorporation into films of organolead halide perovskite such as methylammonium lead iodide ($MAPbI_3$) has been shown to improve their structural stability and electro-optical properties, by reducing ion migration effects, improving grain size, and alleviating hysteresis characteristics.[37, 164-169] In this aspect, the use of polymers for developing high-performance inorganic composites is also well illustrated in nature.[170-172] Molecular weight (Mw) of the polymer chain is a fundamental property that influences critical aspects such as its viscosity, mobility, solubility, and size.[173-175] These aspects of the chains directly impact their ability to interact with an inorganic matrix and hence affects the final properties of the polymer-inorganic composites.[176-178] We specifically show, using polystyrene (PS) and $MAPbI_3$, that the molecular weight of the chains directly affects the structure of the composite thin films at the nanoscale, their electro-optical properties, and their stability. Characterization results show that the PS-$MAPbI_3$ films have a three-layered structure with a nanometer-scale top and bottom polymer-rich phase and an interlaying perovskite-rich phase. The extent of incorporation of the PS in the perovskite matrix is critically affected by the molecular weight of the chains. This variation in the incorporation of PS directly impacts the electro-optical properties of the PS-$MAPbI_3$ films compared to plain $MAPbI_3$ films and better performance is observed at a low and medium molecular weight of PS, with the best performance at Mw ~35,000 kDa. This is supported by the crystal grain size modulation of the films and their stability which follows a similar trend. Polarization effects that have been reported in $MAPbI_3$ films also show a similar dependence on the Mw of the PS chains, where short-circuit currents (I_{sc}) and open-circuit voltage (V_{oc}), both significantly increase for low to medium Mw PS chains.

Further, a linear relationship is observed between the inverse of polymer chain viscosity (in confined spaces, which depends on the polymer $Mw^{1.4}$ and the extent to which the PS is incorporated into the perovskite matrix.[179] Viscosity is a key factor that affects the ability of the chains to reorganize as the perovskite crystallization occurs, directly affecting their incorporation in the perovskite layer at the

grain boundaries. The inverse of ionic current and dark current (which is proportional to film resistance) is related to the Mw of the PS chains based on two terms. One of the terms accounts for the effect of PS on the rate of nucleation of the perovskite in the film, which affects the grain size (and hence also the density of grain boundaries). The other exponential term corresponds to an increase in the charge transport barrier at the grain boundaries due to the inclusion of the PS chains which are insulating in nature. Both terms lead to a decrease in the ionic currents and dark currents with an increase in the Mw of the chains. In comparison, the change in the photo-current of the PS-$MAPbI_3$ shows optimal performance with the use of PS of Mw 35,000 due to the critical effect of grain boundaries that act as charge recombination centers.

4.2 Experimental Section

4.2.1 Synthesis of CH_3NH_3I

A typical synthesis of methylammonium iodide (MAI) involves drop wises addition of 30 ml hydroiodic acid (57 wt. % in water) to 27.8 ml methylamine (33 wt. % in absolute ethanol) under continuous stirring for 2 hours. A dark yellow precipitate was recovered by rotary evaporation of this solution at 60 °C for 1 hour. The solid precipitate was subjected to multiple cycles of washing and recrystallization by a copious amount of diethyl ether and ethanol, respectively until the powder turned white. The resultant white precipitate was vacuum-dried overnight to obtain the pure MAI powder.

4.2.2 Synthesis of perovskite precursor solution

The control 1.35M $MAPbI_3$ solution was prepared by adding 79.4 mg of CH_3NH_3I and 230.5 mg of PbI_2 (99.999% trace metals basis) to a combined solvent of 53.3 ul of dimethyl sulfoxide (anhydrous, ≥99.9%) and 317.5 ul of N, N-dimethylformamide (anhydrous, 99.8%). The synthesis of PS-$MAPbI_3$ precursor solution involved an additional introduction of a fixed concentration (1 wt/v %) of PS (99.9%) of different Mw (2.5, 11, 35, 61, 105, and 190 kDa). The PDI value for the 2.5 kDa PS was 1.03 and for the rest of the different Mw polymers (11, 35, 61, 105, and 190 kDa PS), the PDI value was 1.02. The solution was stirred on a magnetic stirrer for 30 minutes to ensure adequate dissolution of precursor salts and interaction with PS additive.

4.2.3 Fabrication of perovskite-based samples for electro-optical characterization

To understand the influence of variation in Mw of PS additive over optoelectronic properties, lateral devices with $MAPbI_3$ (or PS-$MAPbI_3$) sandwiched between gold (Au) electrodes, were fabricated. The typical fabrication involved spin coating of respective precursor solutions over Si/SiO_2 chips having equidistant gold electrodes at 200 µm (Au chips) as follows:

Au chips were first washed with Millipore water and were then ultrasonicated in acetone and isopropanol for 10 minutes each. After re-washing with Millipore water, the Au chips were put in Piranha solution (3 H_2SO_4:1 H_2O_2) for 3 minutes to remove organic moieties. To remove the acid traces, the chips were washed with copious Millipore water and finally dried with an N_2 gun. The precursor perovskite solution was then spin-coated on the cleaned chips at 4000 rpm for 30 seconds. Within the initial 6-8 seconds of rotations, 200 µl of diethyl ether was dropped over the continuously rotating films to remove excess solvents. The obtained films were finally annealed stepwise at 65 ºC for 2 minutes followed by 100 ºC for 3 minutes to ensure complete perovskite phase formation.

4.2.4 Structural, microscopic, and spectroscopic characterization

The X-ray diffraction pattern of pristine $MAPbI_3$ and PS-$MAPbI_3$ perovskite films was measured by a PANalytical Empyrean diffractometer with Cu Kα radiation ($\lambda = 1.54$ Å). A Zeiss Ultra plus field emission scanning electron microscopy (FE-SEM) equipped with energy-dispersive X-ray spectroscopy (EDX) was used to examine the surface morphology and grain size distribution of freshly prepared samples. A Horiba HR800 spectrometer was used in the backscattering configuration to perform Raman spectroscopy. All Raman spectra were recorded with 6 mW power at an excitation wavelength of 532 nm. The depth profile of freshly prepared perovskite films was analyzed using time-of-flight ion mass spectroscopy by employing a Cs^+ ion source (500 eV) for sputtering and Bi^{3+} (30 keV) for analysis over ToF-SIMS 5, ION-ToF GmbH.

4.2.5 Electrical measurements

Electrical measurement on the planar lateral device configuration of Au|$MAPbI_3$/PS-$MAPbI_3$|Au self-powered photodetector was conducted using a probing station. A two-probe method was employed by connecting one probe to a gold electrode on the chip and another probe connected to the ground. A Keysight 6614C 50-Watt system power supply with a maximum voltage output of 100 V was used for applying an external bias. For generating an optimum inherent polarization in perovskite film without

incurring material degradation, an external bias of 2 V was applied for 5 min. Post poling, optoelectronic measurements including the open-circuit voltage (Voc) and short-circuit current (Isc) were sequentially measured using a Keysight 3458A Digital multimeter. The perovskite-based photodetector device was connected in series with the multimeter and power supply to complete the circuit. A simulated airmass 1.5 global irradiation (100 mW/cm^2) generated using a Xenon-lamp based solar simulator (Newport Oriel Instrument 67005, 150 W Solar Simulator) was utilized for performing measurements under illumination. A National Renewable Energy Laboratory (NREL) calibrated KG5 silicon reference cell was used to calibrate light intensity to minimize any spectral mismatch. The long-term stability test was performed over devices exposed to ambient conditions with 40−45% relative humidity (RH) and measured in 1 day. The humidity was measured by a portable RH sensor and was controlled by adjusting the flow rate of the carrier gas (dry N_2).

4.3 Results and Discussion

The structural characterization of the polymer-perovskite (with varying polymer chain length) and plain perovskite material by X-ray diffraction (Figure 4.1a) show that the typical tetragonal phase is observed in all cases. All PS-$MAPbI_3$ films are made by using a previously optimized concentration of 1 wt. % PS in the precursor solution.[118] The change in Mw (chain length) of the PS (or its presence) does not alter the structure of the perovskite films, as sharp diffraction peaks corresponding to (1 1 0), (2 2 0) and (2 2 2) *h k l* planes remain intact across all diffraction patterns and no impurity phase is observed (Figure A4.1). However, as seen in Figure 4.1b-c, the intensity of dominant (1 1 0) and (2 2 0) diffraction peaks change as a function of PS Mw. Primarily, the introduction of lower Mw members of the PS family (2.5, 11, and 35 kDa) leads to a successive increase in diffraction peak intensity with the highest being observed for 35 kDa PS-$MAPbI_3$. However, a further increase in Mw of PS (61, 105, and 190 kDa) results in a progressive reduction of peak intensity.

The full width at half maximum (FWHM), which is a measure of the crystallite quality, likewise varies as a function of PS chain length. In general, smaller FWHM values correspond to a larger crystallite size.[180] The FWHM (Figure 4.1d) values decrease successively with an increase in Mw of PS additive, with the lowest being observed for 35 kDa M_w PS-$MAPbI_3$ and starts increasing again for the higher Mw PS-$MAPbI_3$. The incorporation of PS of varying Mw into the perovskite solution thus assists in controlling the nucleation rate and growth and hence the grain size of the polycrystalline perovskite film due to the interaction of the polymer with $MAPbI_3$ and its precursors.[181] The most intense

diffraction peaks and smallest FWHM values are observed for the 35 kDa PS-$MAPbI_3$ which should lead to the largest crystallite size and better quality of the perovskite-polymer hybrid film owing to optimum crystallization kinetics.[181] The average crystallite size corresponding to pristine and PS-$MAPbI_3$ calculated using Scherrer's equation are tabulated in Table A4.1

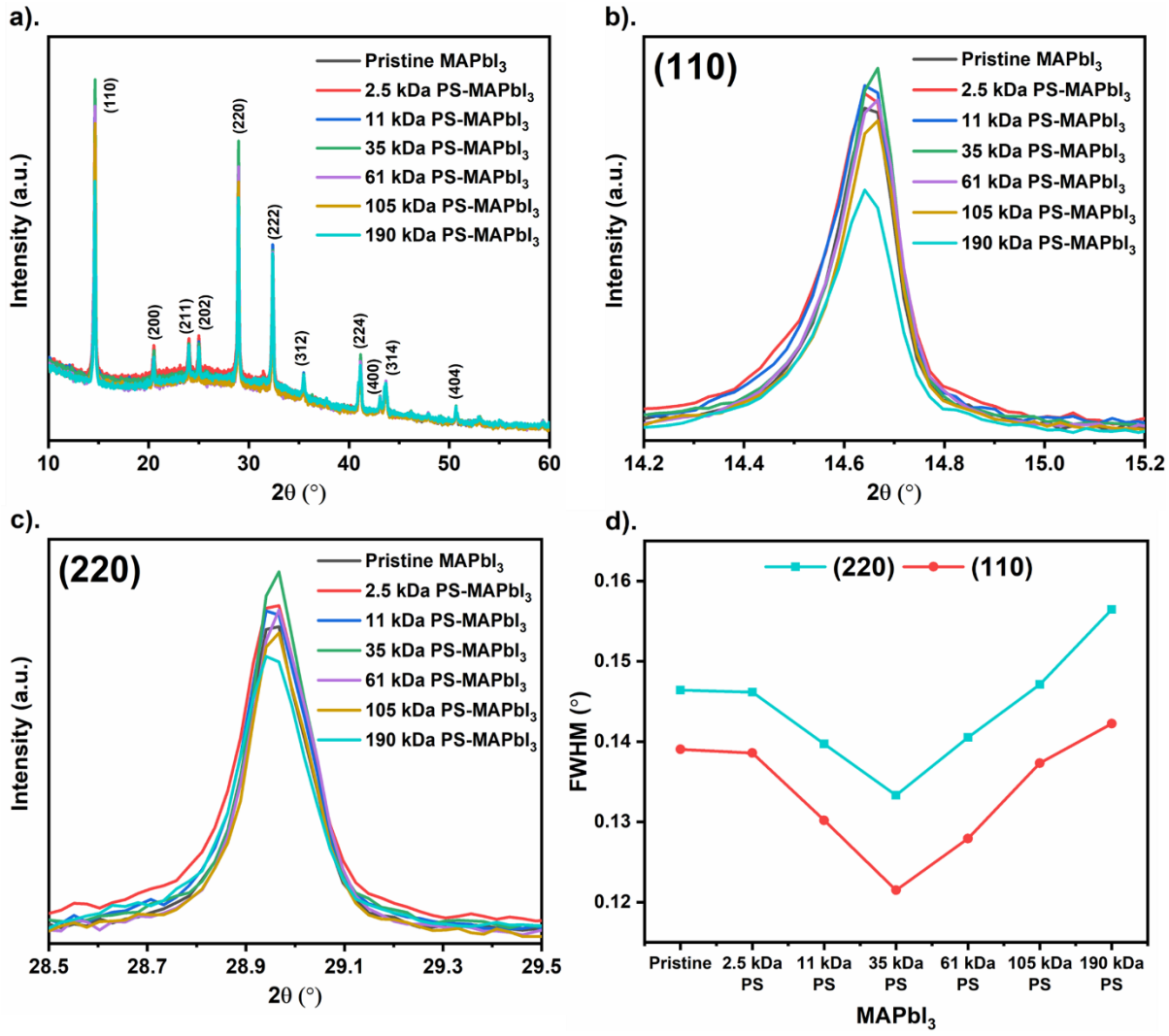

Figure 4.1 (a) X-ray diffraction pattern of pristine $MAPbI_3$ and PS-$MAPbI_3$ with varying polymer Mw exhibiting tetragonal phase. Variation in intensity of (b) (110) h k l plane and (c) (220) h k l plane as a function of additive PS chain length. (d) Dependence of (110) and (220) h k l planes FWHM values on Mw of PS.

The effect on the grain size in the perovskite films due to variation in Mw of polymer is confirmed by Field emission scanning electron micrographs (FE-SEM) (Figure 4.2a-g). Considering the naturally formed grooves on top of perovskite films representative of the grain boundaries, the average size of the grain in the samples is presented in Figure 4.2h. In general, a larger grain size with uniform films is observed with intermediate polymer Mw, with the best films being observed for the 35 kDa sample. However, with higher-Mw members of PS (105 and 190 kDa), non-uniform grain morphology is observed. Longer polymer chains have reduced mobility and occupy a larger volume which hinders their ability to orient as the perovskite crystals grow, this limits the size of the crystal grains and enhances the nucleation events.[181] Since the increase in grain boundary density and defects may act as trap and recombination centers for charge carriers, tuning of polymer chain length could be effectively utilized to manipulate the optoelectronic characteristics of perovskite-based devices.[182, 183] The FESEM analysis provides a qualitative comparison of the grain sizes in the perovskite films, and the trend with the inclusion of PS of varying Mw, is corroborated by the XRD data discussed above.[184-186]

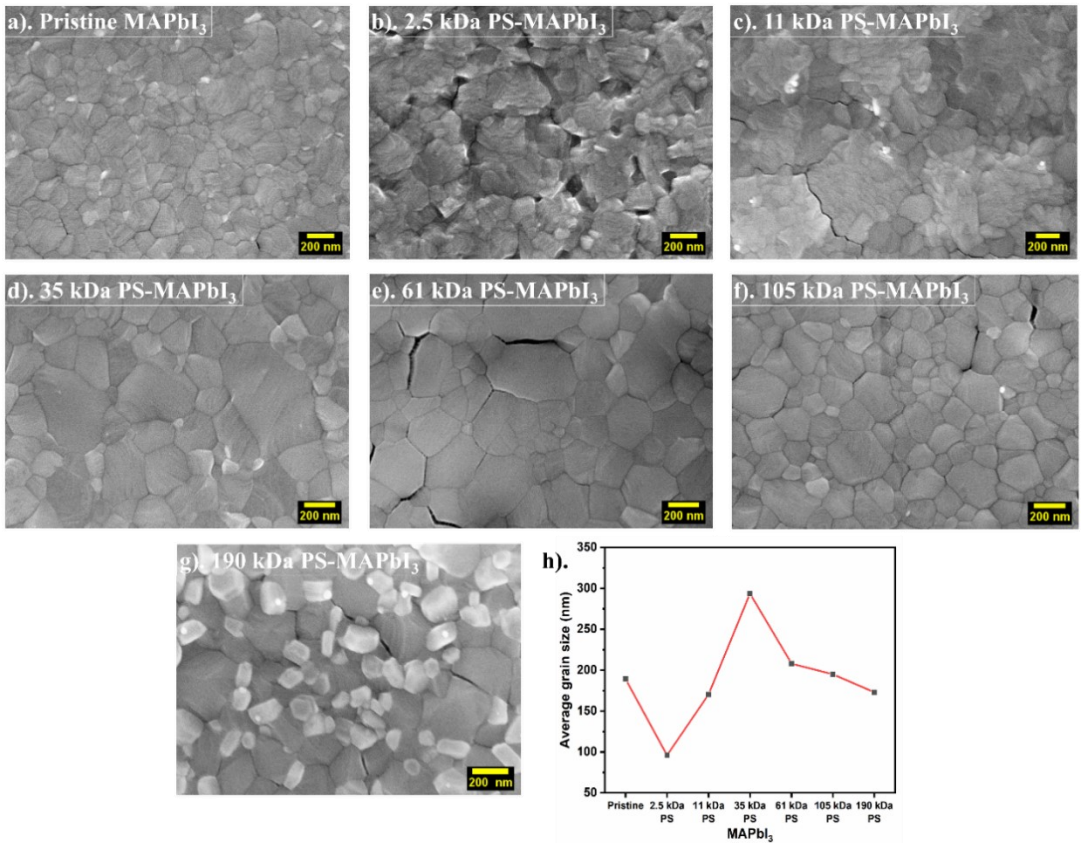

Figure 4.2 Scanning Electron Micrographs of (a) pristine $MAPbI_3$, (b) 2.5 kDa PS-$MAPbI_3$, (c) 11 kDa PS-$MAPbI_3$, (d) 35 kDa PS-$MAPbI_3$, (e). 61 kDa PS-$MAPbI_3$, (f). 105 kDa PS-$MAPbI_3$ and (g). 190 kDa PS-$MAPbI_3$. (h) Average grain size in pristine and PS-$MAPbI_3$ films. Here, the cracks ascribe to e-beam induced localized widening of grain boundaries due to prolonged scanning time.

The specific molecular-level interaction between perovskite precursors and PS of different Mw is characterized by Raman spectroscopy. The pristine $MAPbI_3$ and different Mw PS-$MAPbI_3$ films exhibit sharp characteristic peaks of Pb-I liberation mode and MA^+ liberation mode peaks at 91 and 155 cm^{-1} respectively, and a broad MA^+ torsional mode peak centered at 260 cm^{-1} (Figure A4.2a). As observed in Figure A4.2b, the Pb-I liberation mode shifts to a higher wavenumber with the inclusion of the PS. Typical cation-π interaction between MA^+ and PS chains also leads to variation in MA^+ liberation and torsional modes in the PS-$MAPbI_3$ films (Figure A4.2c). Such variation in perovskite's Raman active modes signifies an enhanced molecular-level interaction between PS and perovskite precursors[99] which forms the basis of the inclusion of PS in the perovskite layers. The interaction between PS and the

perovskite precursors was also confirmed by gel permeation chromatography[37] and the growth of single perovskite crystals.[181]

A key factor that will affect the perovskite performance is the structure of the material distribution and the concentration of the PS material across these films. ToF-SIMS depth profiling on the plain perovskite films and those with varying Mw of PS is conducted for this purpose. The ToF-SIMS profile of plain $MAPbI_3$ (Figure 4.3a), 2.5 kDa PS-$MAPbI_3$ (Figure 4.3b), 11 kDa PS-$MAPbI_3$ (Figure 4.3c), 35 kDa PS-$MAPbI_3$ (Figure 4.3d), 61 kDa PS-$MAPbI_3$ (Figure 4.3e), 105 kDa PS-$MAPbI_3$ (Figure 4.3f) and 190 kDa PS-$MAPbI_3$ (Figure 4.3g) films show that the typical PbI_3^-, CN^-, I_2^- signals, indicative of $MAPbI_3$ are detected spanning the entire perovskite film.[187-189] Moreover, the intensity of the signals remains constant during the sputtering process. In contrast, the C_2H^- and C_2^- signals, indicative of PS[190, 191] (Figure A4.3), are only observed in PS-$MAPbI_3$ films and are negligible in pristine $MAPbI_3$. Common amongst all PS-$MAPbI_3$ films, the PS signals gradually drop within 5-15 sec of sputter time, signifying a very thin PS-rich layer at the top interfaces of all PS-$MAPbI_3$ polycrystalline films. Similarly, a relatively PS-rich layer is observed at the bottom interface between the perovskite layer and the substrate. The thickness of both the PS-rich interfacial layers decreases with the Mw of the PS. Further, the signal strength of the PS which is directly proportional to its concentration also decreases with the Mw of the PS and stabilizes at the higher Mw. In the middle layer of the film, which is the relatively perovskite-rich layer, PS concentration decreases as a function of the PS Mw. Such variation in PS concentration across perovskite film could be considered a direct measure of the ability of PS chains to orient, stretch and undergo motion to successfully get incorporated into the perovskite structure at the grain boundaries. Such adjustments are required from the PS chains to accommodate the perovskite grains as they nucleate and grow in the film. Lower Mw PS chains due to their lower viscosity can more easily undergo such adjustments compared to higher Mw chains and hence can get incorporated into the film at a greater concentration.[192]

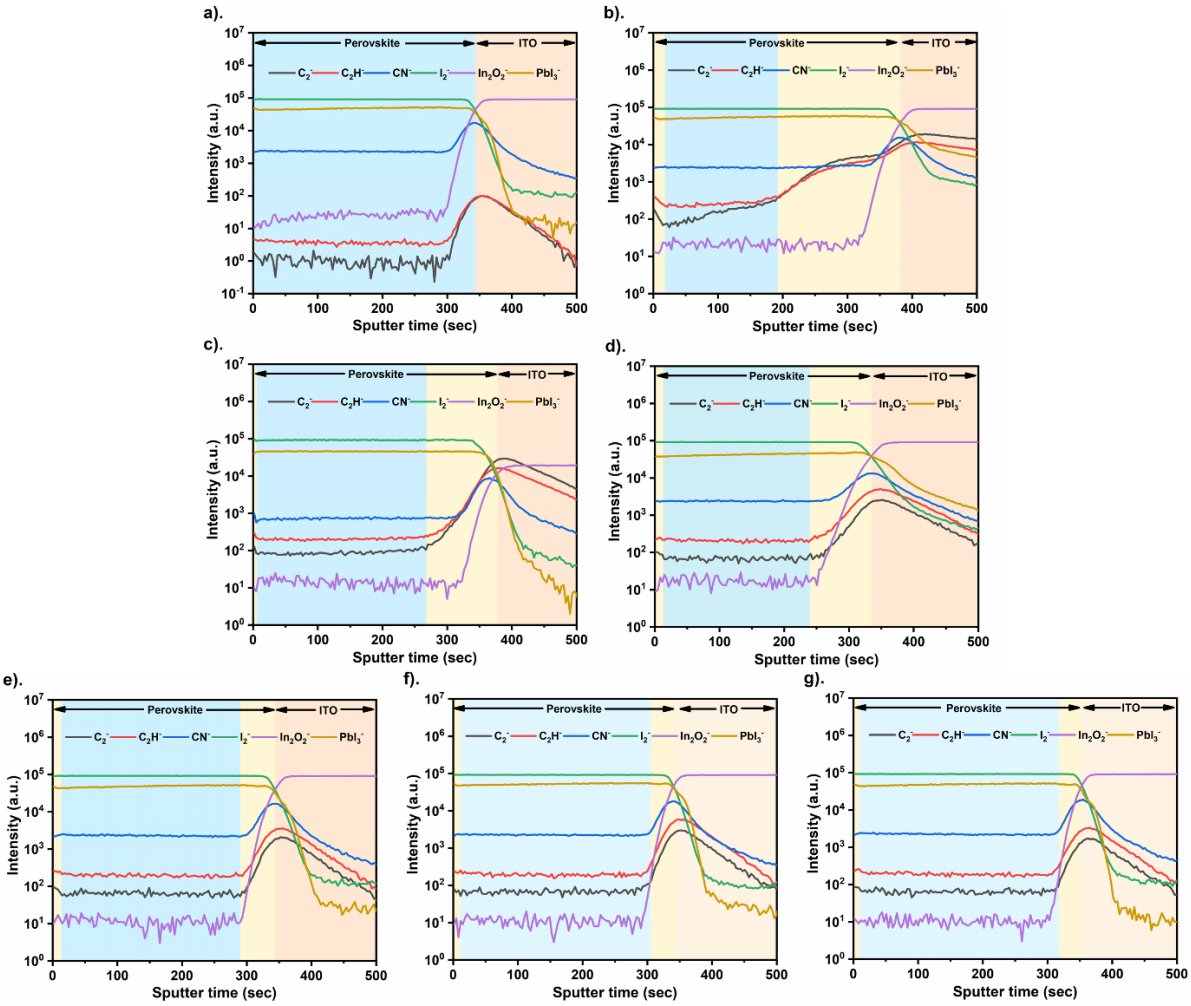

Figure 4.3 ToF-SIMS depth profiling of (a) pristine $MAPbI_3$, (b) 2.5 kDa PS-$MAPbI_3$, (c) 11 kDa PS-$MAPbI_3$, (d) 35 kDa PS-$MAPbI_3$, (e) 61 kDa PS-$MAPbI_3$, (f) 105 kDa PS-$MAPbI_3$ and (g) 190 kDa PS-$MAPbI_3$. The blue and pink colored region distinguishes between perovskite film and ITO substrate, respectively, while the yellow region represents the sputter time frame where relatively high PS concentration is observed.

The PS-$MAPbI_3$ films are further characterized to evaluate the effect of PS Mw, and the structure of the films on their electro-optical properties. In the configuration of Au|$MAPbI_3$/PS-$MAPbI_3$|Au, the photoresponse, dark current, and ionic currents (due to ion migration effects) of the plain perovskite and PS-$MAPbI_3$ films are characterized. The results from the optoelectronic measurements suggest that the PS-$MAPbI_3$ devices with varying polymer Mw, exhibit high photocurrent and low dark current

compared to pristine $MAPbI_3$. When the lower Mw PS is initially introduced in the perovskite films, the photocurrent response (Figure 4.4a) increases sequentially in 2.5, 11, and 35 kDa PS-$MAPbI_3$ and later decreases successively in 61,105 and 190 kDa PS-$MAPbI_3$. On the contrary, as observed in Figure 4.4b and Figure A4.4 respectively, the dark current and the ionic current decrease successively with increasing Mw of the PS.

The extent of decay in the dark current from the initial value to a final stable value characterizes the ionic current due to ion migration in the films (Figure A4.4). This transient decay behavior can be explained by the movement of mobile ions in the perovskite film towards metal electrodes due to the applied bias. The accumulating ions lead to an electric field that opposes the applied external field and hence a transient decay in current is observed. The rate of decay in current will depend on the mobility of the ions, and the extent of the decay characterizes the magnitude of ion migration effects. Consequently, perovskite films with higher ion mobility and density of ionic defects will exhibit faster decay under an applied bias.[27, 110] Specifically, the initial dark current at t = 0 sec for pristine $MAPbI_3$ is 9.8 nA which suffers a rapid decay (55.1%) and is reduced to 4.4 nA within 10 sec (Figure A4.5). On the other hand, the decay of dark current in 35 kDa PS-$MAPbI_3$ is much slower (7.6% within 10 sec). The net drop in dark current after 275 sec for 35 kDa PS-$MAPbI_3$ (0.18 nA) is less by a factor of 37 compared to pristine $MAPbI_3$ (6.61 nA) which reveals that the ion migration effects are significantly reduced in PS-$MAPbI_3$. The significant reduction in the magnitude and the rate of decay, of the dark current (Figure A4.6 & 4.4b) for high Mw PS-$MAPbI_3$ films (105 kDa and 190 kDa) and also their low photocurrent response (Figure 4.4a), can be attributed to the decrease in ion mobility and higher overall film resistance with the use of large chain PS.[193] Due to the combined effects of photocurrents and dark currents, the highest ratio of photocurrent to dark current is for the 35 kDa PS-$MAPbI_3$ films (Figure A4.7). Also, a higher value of photocurrent is observed in the 11 kDa, 35 kDa, and 61 kDa PS-$MAPbI_3$ films compared to plain $MAPbI_3$ films. Combined with the reduced ion migration effects in the PS-$MAPbI_3$ films, it should alleviate the hysteresis effects in perovskite solar cells, without compromising their performance.

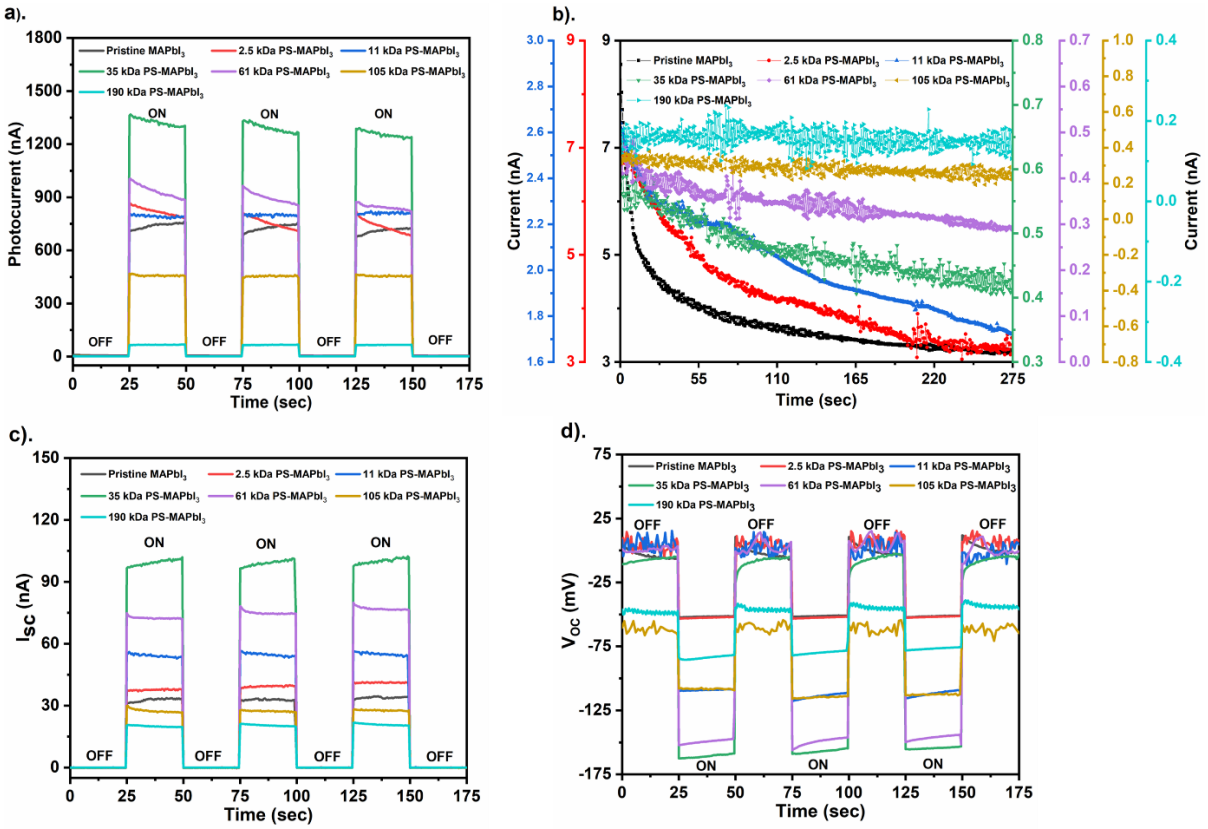

Figure 4.4 (a) Photocurrent response of pristine and PS-MAPbI$_3$ with varying PS Mw. (b) Dark current decay in pristine and PS-MAPbI$_3$. (c) I_{SC} and (d) V_{OC} response for pristine and PS-MAPbI$_3$ films of varying Mw.

Owing to the combination of the effects of electric field poling that leads to polarization in the perovskite films[116, 117, 194] and the inherent semiconducting nature[195-197] of MAPbI$_3$, upon illumination, a self-powered response is observed in these films.[118] The resultant short-circuit current (I_{SC}) response and the open-circuit voltage (V_{OC}) are measured for the plain MAPbI$_3$ and PS-MAPbI$_3$ films (Figure 4.4c-d). Like the photocurrent response, I_{SC} and V_{OC} values increase sequentially for the 2.5, 11, and 35 kDa PS-MAPbI$_3$ and reduce for the higher Mw PS-MAPbI$_3$ device. The best I_{SC} (96.6 nA) and V_{OC} (162.5 mV) are observed for 35 kDa PS-MAPbI$_3$ as it exhibits a 3-fold enhancement compared to that observed for the pristine MAPbI$_3$ (31.1 nA and 52.3 mV, respectively).

The influence of PS on the properties of MAPbI$_3$ is dependent on multiple factors. Among them, the first is the extent to which the PS chains get integrated into the perovskite films. To accommodate the

nucleation and growth of perovskite grains, the PS chains must rearrange at the grain boundaries and the interface. The viscosity of the PS chains hence will critically affect their ability to undergo this rearrangement. Considering that as the perovskite grains grow the PS chains will be confined in space, their viscosity (η) dependence on the Mw follows a power law of $(Mw)^{1.4}$, (Equation A4.1 in Appendix of Chapter 4).[179] The ToF-SIMS PS signal (C_2^-) in the perovskite layer is analyzed for this purpose. As the PS signal (C_{ps}, from C_2^-) is directly proportional to the concentration of the PS groups in the perovskite film, the number of chains of the polymer (n) being incorporated will be proportional to C_{ps}/Mw (Equation A4.2 in Appendix of Chapter 4). A linear dependence is observed between n and $Mw^{-1.4}$ for both the top PS-rich layer and the main perovskite layer (Figure 4.5a-b) (Equation A4.3 in Appendix of Chapter 4). This signifies that with increasing Mw of the PS chains, as the viscosity of the polymer chains increases while their mobility reduces,[198] as expected, the number density of polymer chains in the perovskite matrix decreases.

The inclusion of PS chains in the perovskite matrix affects the electrical conductivity based on two factors. First, the PS chains lead to modulation of the crystallization kinetics and affect the size of the crystal grains (Figure 4.1d and Figure 4.2) and hence also, the density of grain boundaries (and defects associated with them) in the film. Second, the inclusion of PS due to its electrically insulating nature increases the resistance of the PS-$MAPbI_3$ film. The effect of PS on the perovskite grain size is illustrated by the rate of nucleation (Equation A4.4 in Appendix of Chapter 4). The viscosity of the solution increases with $Mw^{1.4}$ (Equation A4.5 in Appendix of Chapter 4), which decreases the rate of nucleation and hence increases the grain size. However, with an increase in the Mw of the chains their volume increases ($n.Mw^{1.74}$)[199], and due to their interaction with the perovskite it decreases the surface energy for the crystals (Equation A4.6 in Appendix of Chapter 4) and hence increases the rate of nucleation. These two competing effects lead to first a decrease in the nucleation rate and then an increase, with the Mw of the PS, as observed in the final Equation A4.9 (in Appendix of Chapter 4). The effect will be the opposite of the grain size (which is inversely proportional to the nucleation rate) which will first increase and then decrease with the Mw of the PS, consistent with the experimental observations (Figure 4.1d and Figure 4.2). The initial increase in grain size will reduce the grain boundaries and hence improve the electro-optical properties of the film at the same time.[200] This is due to the grain boundaries serving as scattering and recombination sites and a barrier for electrical conduction[201, 202] while serving as conducive pathways for ion migrations due to defects.[27, 203] Following

that at higher Mw of PS as the rate of nucleation increases, the grain size becomes smaller and increases the grain boundaries[204] which degrades the electro-optical properties.

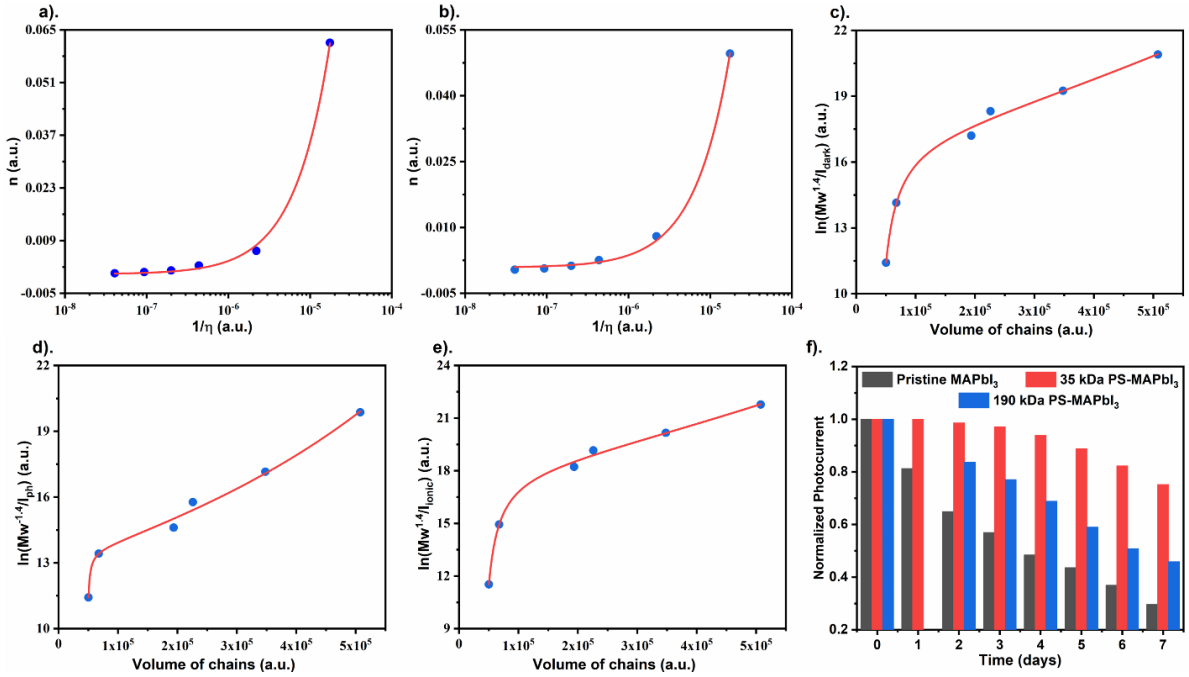

Figure 4.5 Variation in the number of polymer chains present at the (a) PS rich top interface and (b) perovskite layer, as a function of an inverse of viscosity. Dependence of (c) dark current, (d) ionic current, and (e) photocurrent over the volume of PS chains spanning across PS-$MAPbI_3$ films. (f) Pristine and 35 kDa PS-$MAPbI_3$ device stability and performance pattern for the duration of 7 days. The OFF and ON conditions represent measurements performed under light and dark conditions, respectively.

This effect is coupled with the inclusion of the PS chains into the conducting perovskite matrix. The inclusion of insulating PS chains increases the energy barrier for charge transport at the grain boundaries (Equation A4.10 in Appendix of Chapter 4). The energy barrier scales with the volume of the PS chains $n*Mw^{1.74}$ (Equation A4.7 in Appendix of Chapter 4), as PS is an insulator for both charge conduction mechanisms (dark current due to electronic charges and ionic current due to ion migration). The final model that combines both the effects (Equation A4.11-13 in Appendix of Chapter 4) fits accurately the monotonic decrease in the dark current and ionic currents (ion migration) with increasing Mw (Figure 4.5c-d). The model also fits the response observed in the photocurrent which initially increases and then decreases with PS Mw (Figure 4.5e). The combined model signifies the role of PS

in modulating the crystallization dynamics of the perovskite grains and its inherent insulating nature that alters the conductivity of the films. The combined effect from these two factors is effectively illustrated in the model and hence it can accurately scale the behavior of the PS-$MAPbI_3$ films.

Degradation in perovskite films results from two primary factors, one from exposure to environmental elements such as oxygen and moisture and the second due to the internal factor of ion migration. The top PS (hydrophobic) rich layer is crucial for acting as a barrier against oxygen and moisture[169], while the density of grain boundaries in the perovskite-rich layer will determine the ion migration effects.[205] As a result of the combined effect of these two factors and consistent with the electro-optical performance, the best stability is observed for films with PS of Mw 35 kDa in comparison to the plain and the 190 kDa films (Figure 4.5f).

4.4 Conclusion

Three major effects are observed by optimizing the Mw of the PS for inclusion in the perovskite films: 1. It leads to improved stability of the perovskite films; 2. The electro-optical performance of the films is improved; 3. The dark currents and ion migration effects are reduced. These effects from the inclusion of a polymer in the perovskite films result from multiple factors that include, the formation of nanoscale structured layers with polymer-rich layers at the top and bottom interface sandwiching a middle perovskite-rich phase. The three-layered architecture of the PS-$MAPbI_3$ films should also enable better alignment of the energy bands and charge extraction at the interfaces in photovoltaic devices.[205-209] The viscosity of the chains (which depends on their Mw) is the key factor that determines the extent to which they get incorporated into the perovskite structure. This is due to the need for the chains to rearrange during the growth of the perovskite grains. The modulation of the perovskite crystallization kinetics and the insulating nature of PS chains towards both charge and ion transport affect the electro-optical properties of the perovskite film. The combined effect results in optimized electro-optical performance with the use of PS of Mw ~ 35,000. These results show that the Mw of the polymer chains is a key factor to consider in the use of perovskite-polymer devices, as it governs critical aspects of the interaction between the perovskite and the polymer. The strategy presented here also leads to a path for other polymer inorganic composites to optimize the performance based on the characteristics of the polymer.

Chapter 5
Soft Polymer-Organolead Halide Perovskite Films for Highly Stretchable and Durable Photodetector with Pt-Au Nanochain Based Electrodes

5.1 Introduction

The development of stretchable optoelectronic devices with high-performance organic-inorganic materials such as methylammonium lead iodide ($MAPbI_3$) is challenging owing to their rigid and brittle nature.[46, 210, 211] Therefore, strategies are being actively researched to enable such stretchable devices as they will provide a combination of high performance with low form factor and flexibility of function.[212-214] Their direct application is in fields such as solar cells, light-emitting diodes, next-generation displays, and photodetectors.[84, 215-220] Designing a stable perovskite-based stretchable device mandates meeting two basic requirements 1) a photosensitive perovskite layer capable of enduring strain due to stretching without degrading in ambient atmosphere, and 2) mechanically durable and highly conductive underlying electrodes.[221, 222] In addition, fatigue-driven degradation of the perovskite layer during repeated deformations must be limited for the long-term practical viability of such stretchable optoelectronic devices.[223, 224] Most of the past research work has been limited to bendable perovskite devices and little success has been achieved in making stable and stretchable perovskite devices.[225-231] The challenge has primarily been due to the limited mechanical durability of the devices, lasting only a few hundred stretching cycles under small strains, combined with poor environmental stability.[150, 232-239] Therefore, there is an urgent need to address these issues in order to utilize the excellent electro-optical properties of perovskites for the development of stretchable devices.

In this work, we show a stretchable, polystyrene (PS) incorporated $MAPbI_3$ (PS-$MAPbI_3$) photodetector that can sustain 98%, 90%, 62%, and 52% of its initial photocurrent value after 5, 100, 5000, and 10,000 stretching cycles, respectively, at 50% strain. In comparison, the performance in pristine $MAPbI_3$ photodetector drops to 80% after 5 cycles and to just 22% after 10,000 cycles. The stretchable photodetector is made by introducing a wrinkled structure in the device. This is achieved by depositing the device on a pre-stretched flexible substrate and then releasing the strain, inducing a regular wrinkled pattern. The pristine $MAPbI_3$ device shows significant cracking after just 5 stretching cycles, leading to a drastic loss in performance. In comparison, the PS-$MAPbI_3$ has significantly reduced crack density

with a much smaller size of the cracks. Instead, small flakes are observed in response to the stretching, leading to sustained device performance. The key is the introduction of the PS in the $MAPbI_3$, which reduces the modulus of the film by ~38%. The measured surface modulus of pristine $MAPbI_3$ is ~11.7 GPa, while in PS-$MAPbI_3$ this is reduced to 7.1 GPa. The presence of insulating hydrophobic PS chains also leads to a three-layer structure, which reduces ion migration across grain boundaries and simultaneously protects against the ambient environment.[119] To address the equally important issue of fabrication of low-cost electrodes which can survive extreme bending, twisting, and stretching conditions, the current work demonstrates the utilization of room temperature solution-processed platinum-gold (Pt-Au) nanoparticle chains.[240] The mesh of metallic Pt-Au nanochains has high conductivity and offers resistance against oxidation over the conventionally used Ag and Cu nanowire electrodes in flexible devices.[241-244] Further, the nanochain electrodes are deposited by a simple vacuum filtration-based method, a cost-effective alternative to sputtering and thermally evaporated metal electrodes.[245, 246] The stretchable photodetector assembly of 1 wt/v % PS-$MAPbI_3$ film with underlying Pt-Au nanochains electrodes exhibits, ultralow dark currents in the range of $\sim 10^{-11}$ A, high light switching ratio of the order $\sim 10^3$, and can sustain high lateral strain up to 100%.

5.2 Experimental Section

5.2.1 Preparation of Pt-Au and Au-Ca^{2+} solution

1 mL of citrate capped gold nanoparticle solution (~10 nm, BBI Solutions OEM Limited) was mixed with 135 µL of 4.5 mg/mL $PtCl_4$ (99.9%, Sigma-Aldrich) and kept on a shaker at 300 rpm until the color of the solution changed to dark blue indicating Pt^{4+} ions assisted self-assembly of Au nanoparticles. To reduce Pt^{4+} ions to metallic Pt, 75 µL of 4 mg/mL $NaBH_4$ (99%, Sigma-Aldrich) was later added to the solution leading the solution color to turn to a dark brown color indicating the formation of metallic Pt-Au nanoparticle chains. The Au-Ca^{2+} nanoparticle chain solution was prepared similarly. Briefly, 1 ml of gold solution was mixed with 105 µL of 1 mg/mL $CaCl_2$ (99.0%, ACP chemicals Inc.) and left on the shaker until the solution color changed to dark blue.

5.2.2 Fabrication of PDMS mask

2.0 g of silicone elastomer base (Dow Inc.) was mixed with 0.2 g elastomer curing agent (Dow Inc.) and degassed under vacuum to remove air bubbles. The mixed solution was later cured at 75 °C for one hour. A 5 mm long and 2 mm spaced electrode pattern was obtained using laser cutting.

5.2.3 Preparation and transfer print of Pt-Au electrodes on PET

The fabrication process of the stretchable Pt-Au nanochain electrodes on PET is schematically illustrated in Figure 5.1a. To ensure the formation of a smooth interfacial layer and enable efficient transfer, 0.6 ml of Au-Ca^{2+} solution was first vacuum filtered through a 200 nm pore-sized polycarbonate filter membrane (WATMAN) kept on top of the patterned PDMS. 0.8 ml of Pt-Au solution was then vacuum filtered to obtain the black-colored Pt-Au nanoparticle chain electrodes. Simultaneously, a 0.5×0.5-inch piece of 12.5 µm thin PET film was cleaned with acetone, and isopropyl alcohol was treated with UV-ozone for 15 min. The Pt-Au nanoparticle chains-based electrodes were finally transfer printed from the filter membrane to the PET with the assistance of water.

5.2.4 Synthesis of CH_3NH_3I precursor

Methylammonium iodide (MAI) was synthesized by dropwise addition of 30 mL of hydroiodic acid (57 wt. % in water, Sigma-Aldrich) to 27.8 mL of methylamine (33 wt. % in absolute ethanol, Sigma-Aldrich) under constant stirring at 0 °C. This solution was stirred for 2 hours and later, a dark yellow precipitate was recovered using a rotary evaporator at 60 °C for 1 hour. The solid precipitate was then washed and recrystallized with a copious amount of diethyl ether and ethanol, respectively, until it turned white. The resultant white precipitate was dried overnight to obtain pure MAI.

5.2.5 Synthesis of perovskite precursor solution

A 1.35 M pristine $MAPbI_3$ solution was prepared by mixing 79.4 mg of MAI and 230.5 mg of lead iodide (99.999% trace metals basis, Sigma-Aldrich) in 53.3 µL of dimethyl sulfoxide (anhydrous, ≥99.9%, Sigma-Aldrich) and 317.5 µl of N, N-dimethylformamide (anhydrous, 99.8%, Sigma-Aldrich). To obtain the PS-$MAPbI_3$ solution, 1 wt/v % PS (0.0037g PS of average Mw 35 kDa and PDI of 1.02, Sigma-Aldrich) was additionally introduced in the perovskite precursor solution. The solution was later stirred on a magnetic stirrer for 30 minutes to allow cross-linking in PS, before spin-coating in ambient conditions.

5.2.6 Fabrication of stretchable perovskite-based photodetector

The PET film carrying Pt-Au nanochain electrodes was pasted on a pre-stretched elastomeric adhesive (3M™ VHB™ 4910) tape. A small amount of eutectic gallium indium was brushed over the Pt-Au electrode ends to enhance the availability of the contact area and avoid perforation of thin PET by sharp probe tips while performing electro-optical measurements. 50 µL of perovskite precursor solution was

then spin-coated on the pre-stretched assembly at 3500 rpm for 30 seconds. Upon reaching 6 seconds of rotations, 150 µl of diethyl ether was drop cast. The obtained films were annealed stepwise at 65 ºC for 5 minutes followed by 100 ºC for 8 minutes to ensure the complete formation of the perovskite phase. Finally, a transparent self-adhesive tape was used to cover the perovskite films during optoelectronic measurements.

5.2.7 Structural, microscopic, and spectroscopic characterization

The grazing incidence X-ray diffraction (GIXRD) patterns of obtained samples were measured using a PANalytical X'Pert Pro MRD diffractometer with Cu Kα radiation (λ = 1.54 Å) at an incidence angle of 0.4°. A Zeiss Ultraplus field emission scanning electron microscopy (FE-SEM) was used to examine the surface topology and grain size distribution of the pristine and polymer-integrated perovskite films. The optical absorption spectra were recorded using a UV–Visible spectrophotometer (Perkin Elmer Lambda 750). Young's Modulus and dissipation energy maps were acquired using RTESPA 525 probes (Bruker) with a nominal spring constant of 200 N/m and resonant frequency of 525 kHz on a Bruker Dimension Icon in PeakForce QNM mode. The spring constant and deflection sensitivity of the probes were calibrated using a sapphire standard sample before each measuring session. The tip radius was estimated to be 20-30 nm, using a Titanium sample of known roughness. The elastic modulus for the sample surface was calculated following the Derjaguin-Muller-Toropov (DMT) model for tip-sample contact.[247]

5.2.8 Electrical measurements

The electrical measurement on the planar lateral device configuration of Pt-Au/$MAPbI_3$ (PS-$MAPbI_3$)/Pt-Au photodetector was conducted using a probing station. A two-probe method was employed by connecting a single probe to one of the Pt-Au electrodes and the other probe to the second Pt-Au electrode. A Keysight 6614C 50-Watt system power supply was used for applying an external bias. For carrying out optoelectrical measurements of the perovskite-based stretchable photodetector device, an external bias of 3.5 V was applied. The current-voltage (*I-V*) characteristics, photocurrent, dark current, spectral response, responsivity, and detectivity were sequentially measured using a Keysight 3458A Digital multimeter. The perovskite film was connected in series with the multimeter and power supply to complete the circuit. Simulated AM 1.5 global irradiation (100 mW cm^{-2}) generated using a Xenon-lamp based solar simulator (Newport Oriel Instrument 67005, 150 W Solar Simulator) was used for illuminating the sample, unless stated otherwise. The Newport optical bandpass

and neutral density filters were used to vary incident light intensities and spectral selectivity. An NREL calibrated KG5 silicon reference cell was used to calibrate light intensity to minimize any spectral mismatch. All measurements were conducted in ambient conditions. The active area of the devices was 0.10 cm^2. For the stretching cycles, an MFA motorized miniature linear stage was used to stretch the flexible device at 50% of its initial relaxed position and to perform 10,000 stretching cycles at a constant speed. The long-term stability test of the devices was tested by directly exposing the devices to ambient air with 35−40% relative humidity and under room light. The humidity was measured by a portable RH sensor and was controlled by adjusting the flow rate of the carrier gas (dry N_2).

5.3 Results and Discussion

The schematic in Figure 5.1a represents the fabrication process of the stretchable organolead halide perovskite films. The detailed process is described in the Experimental section. Briefly, first for making the electrodes, a solution consisting of Pt^{4+} ions mediated self-assembled micron-sized long Au nanoparticle chains were initially reduced to obtain a continuous network of ~5-10 nm wide metallic Pt-Au nanochains (High-resolution transmission electron microscopy (HRTEM) and field emission scanning electron microscopy (FE-SEM) images in Figure 5.1b and Figure 5.1c, respectively). The metallic Pt-Au nanochains solution was vacuum filtered through a polycarbonate filter membrane using patterned polydimethylsiloxane (PDMS) mask to obtain a pair of highly conductive electrodes (Figure 5.1d). The lateral electrode assembly was then transfer printed on a UV-Ozone pre-treated polyethylene terephthalate (PET) film that was finally pasted over a pre-stretched (under 100% lateral strain) very high bonding (VHB) elastomeric adhesive. The $MAPbI_3$ layer is formed by spin coating and a two-step annealing procedure, following that, the pre-stretched substrate when released, undergoes buckling to ultimately yield a wrinkled perovskite film (at 0% strain). The polymer-organolead halide perovskite films (PS-$MAPbI_3$) were prepared similarly by utilizing a previously optimized concentration of 1 wt/v % 35 kDa PS.[37, 119]

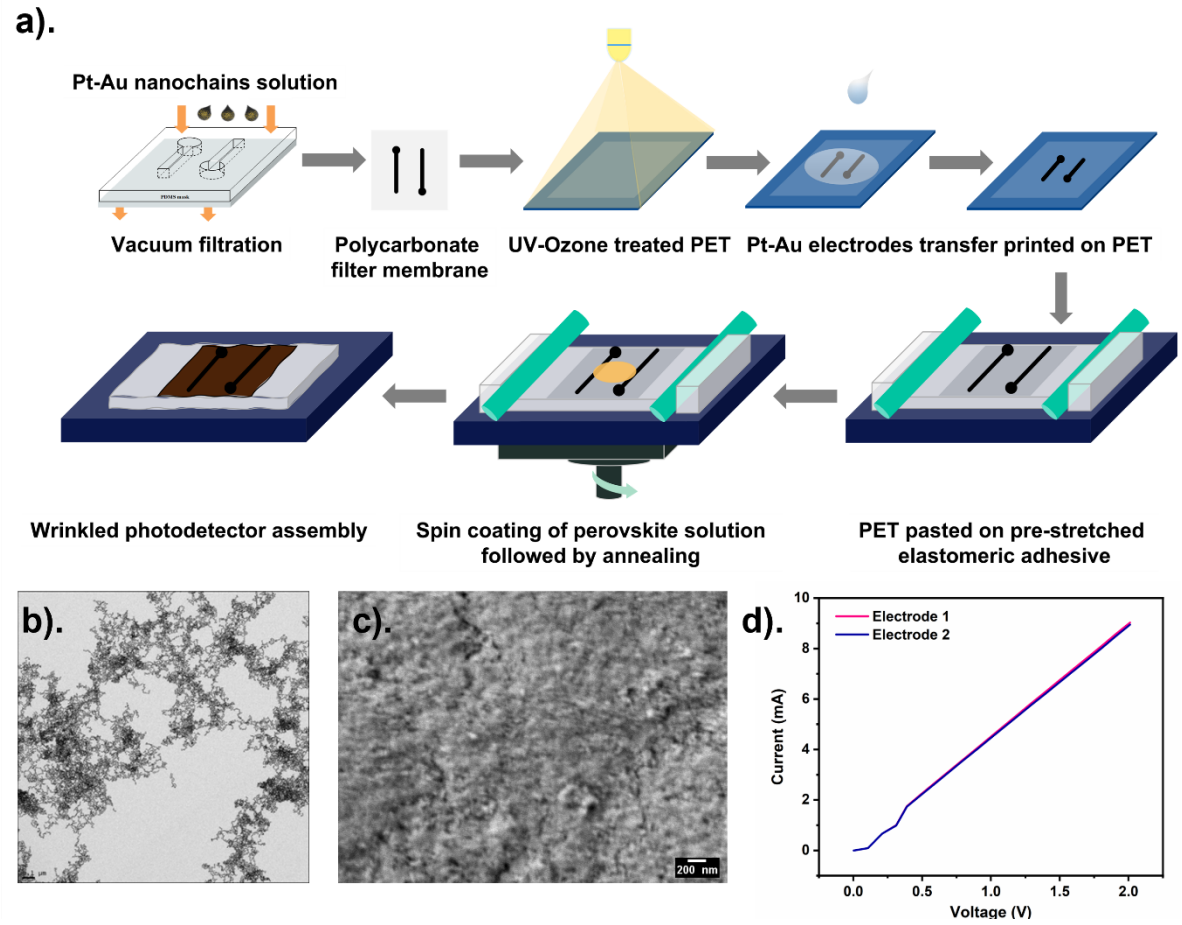

Figure 5.1 Fabrication and characterization of the perovskite-based stretchable photodetector. (a) Vacuum filtration assisted deposition of electrodes on polycarbonate filter membrane using self-assembled Pt–Au nanochains solution, transfer printing of Pt-Au electrodes on PET pasted over a pre-stretched elastomeric substrate followed by spin coating of perovskite solution and annealing. (b) HRTEM image of the metallic Pt-Au nanochains. (c) FE-SEM images of the Pt-Au electrodes transfer printed on flexible PET substrate. (d) *I-V* curve of Pt-Au electrodes transfer printed on PET exhibiting high conductivity.

The cross-section FE-SEM image in Figure 5.2a confirms the wrinkled structure of the photodetector. The thickness of the perovskite absorber layer is 400 nm while the Au-Pt nanochains electrode is 710 nm thick (Figure A5.1). The amplitude and the wavelength of the pattern match closely to the theoretical model, as being determined by the flexible substrate (VHB) and the PET films (details in Appendix for Chapter 5).[248, 249] The lateral FE-SEM images showcase the presence of relatively larger

grains in the PS-$MAPbI_3$ films (Figure 5.2b) in comparison to pristine $MAPbI_3$ (Figure 5.2c). The corresponding grain size distribution for pristine and PS-$MAPbI_3$ is presented in Figure A5.2a and Figure A5.2b, respectively. Previous studies validate that the incorporation of PS in the perovskite matrix leads to modulation of the nucleation and the growth rate of crystal grains, along with reduced defect density.[37, 75] This is attributed to the direct interaction of PS chains with $MAPbI_3$ precursors which has previously been confirmed.[75, 99] The X-ray diffraction (XRD) pattern (Figure 5.2d) shows the formation of a single tetragonal phase in both $MAPbI_3$ and PS-$MAPbI_3$ films, with dominant peaks corresponding to (1 1 0) (2 2 0) and (3 1 0) lattice plane and no obvious impurities. As represented in Figure 5.2e, the UV-Visible absorption spectra of both $MAPbI_3$ and PS-$MAPbI_3$ films demonstrate their excellent light-harvesting characteristics with broad absorption spanning across 300-780 nm, with the inherent absorption properties of $MAPbI_3$ being conserved in the presence of the polymer additive.

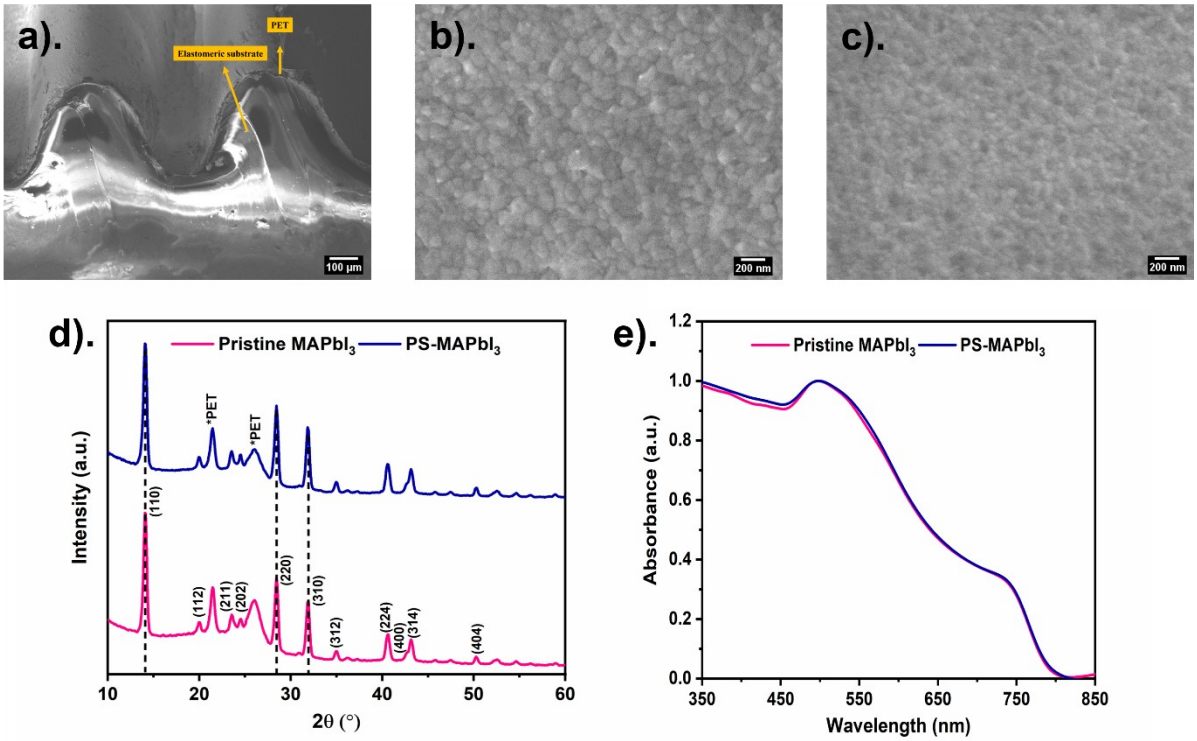

Figure 5.2 (a) Cross-sectional FE-SEM image of wrinkles developed in the photodetector assembly upon relaxation (to 0% strain). FE-SEM image of (b) PS-$MAPbI_3$ and (c) pristine $MAPbI_3$. (d) X-ray diffraction (XRD) pattern and (e) UV–visible absorption spectra of pristine and 1 wt/v % PS-$MAPbI_3$ films.

The operating principle of the two-terminal stretchable perovskite device is based on the photoconductive effect. In presence of an external bias, an electric field is induced within the perovskite film which drives the separation of photogenerated charge carriers. Owing to energy level alignment, holes are preferentially collected at the negative Pt-Au electrode in the symmetric Pt-Au/$MAPbI_3$ (or PS-$MAPbI_3$)/Pt-Au lateral device configuration.[250] The photoresponse of the photodetectors under the variable lateral strain of 0, 50, and 100 % at an applied bias of 3.5 V with the illumination of 1.0 sun is presented in Figure 5.3a. The corresponding light switching ratio of photocurrent to dark current (I_{ph}/I_{dark}) is illustrated in Figure A5.3. An increase in the wrinkle radius with a decrease in height is observed on stretching the device (Figure 5.3b). The relaxed photodetector (under 0% strain) exhibits the highest photocurrent owing to better trapping of photons within the wrinkled structures (Figure 5.3c).[238, 251] The effective photon trapping, and absorption proficiency are reduced when the device is stretched to 50 and 100% of the relaxed position. The PS-$MAPbI_3$ photodetector exhibits better photocurrent in comparison to the pristine $MAPbI_3$ across all strain positions. The pristine $MAPbI_3$ photodetector exhibits ultralow dark currents (in the 10^{-11} A range) with the values being further reduced for the PS-$MAPbI_3$ device. The stretchable PS-$MAPbI_3$ photodetector maintains ~85% (60.32 nA) of its initial photocurrent (71.28 nA) under 50% strain and this is reduced to ~38% (27.57 nA) upon stretching the device to 100%. Specifically, at 50% strain, the PS-$MAPbI_3$ device exhibits ~1.4 times higher photocurrent (60.32 nA) in comparison to the pristine $MAPbI_3$ (43.77 nA). Meanwhile, the dark current is reduced to more than one-half (28.11 pA) in PS-$MAPbI_3$ with respect to the pristine $MAPbI_3$ film (66.39 pA). The improved optoelectronic characteristics in PS-$MAPbI_3$ can be attributed to higher carrier lifetime and mobility, reduced recombination, and ion migration, owing to larger grain size and lower density of associated defects.[37] As the PS-$MAPbI_3$ device still maintains 85% of the efficiency at 50% stretching, the rest of the measurements were carried out at similar lateral strain. As expected, an increase in the applied potential leads to both higher dark and photocurrent in $MAPbI_3$ and PS-$MAPbI_3$ photodetectors (Figure A5.4). The photoresponse of both types of photodetectors under 50% lateral strain, as a function of different illumination intensity, is presented in Figure 5.3d, where an increase in photocurrent with higher photon flux (higher intensity) is observed. As seen in Figure 5.3e, an I_{ph}/I_{dark} ratio of ~6000 is exhibited at 1.0 sun illumination which is reduced to ~20 at 0.001 mW cm^{-2}. Owing to the reduced dark currents the PS-$MAPbI_3$ device exhibits ~4 folds improvement in the I_{ph}/I_{dark} value in comparison to pristine $MAPbI_3$. The corresponding responsivity (R) and detectivity (D*) values were calculated using the following equations:

$$R = \frac{I_{ph} - I_{dark}}{P_{in}} \quad (1)$$

$$D^* = \frac{R}{\sqrt{\frac{2qI_{dark}}{A}}} \quad (2)$$

where I_{ph}, I_{dark}, P_{in}, q, and A represent photocurrent, dark current, incident illumination power, elementary charge, and effective active area of the photodetector, respectively.[252] The PS-$MAPbI_3$ photodetector exhibit a maximum responsivity Figure 5.3f) of 2.05 mA W^{-1} and detectivity (Figure 5.3g) of 0.36×10^{12} Jones at 0.001 mW cm^{-2} illumination. The pristine $MAPbI_3$ device achieves a relatively lower responsivity and detectivity of 1.36 mA W^{-1} and 0.13×10^{12} Jones, respectively.

The photoresponse cycles for the PS-$MAPbI_3$ and pristine $MAPbI_3$ photodetectors were recorded at different wavelengths spanning across the visible light spectrum while the devices were held at 50% strain, follow the pattern of the absorption spectra, and is presented in Figure 5.4a. The small current observed at 800 nm can be ascribed to the ±10 nm FWHM of the band pass filter used to record the photoresponse. The corresponding responsivity and detectivity are presented in Figures 5.4b and c, respectively. The PS-$MAPbI_3$ films exhibit relatively higher responsivity and detectivity than that observed in pristine $MAPbI_3$ films. The PS-$MAPbI_3$ photodetector attains maximum responsivity and detectivity values of 86.48 μA W^{-1} and 12.47 $\times10^9$ Jones at 400 nm. The performance is limited by the large active area of the device, the absence of charge transport layers, and the smaller average grain size due to the poor wettability of the PET substrate. The response time based on the rise and fall time of the 1 wt/v % PS-$MAPbI_3$ photodetector was determined to be 2.22 and 2.96 ms, respectively (Figure 5.4d).

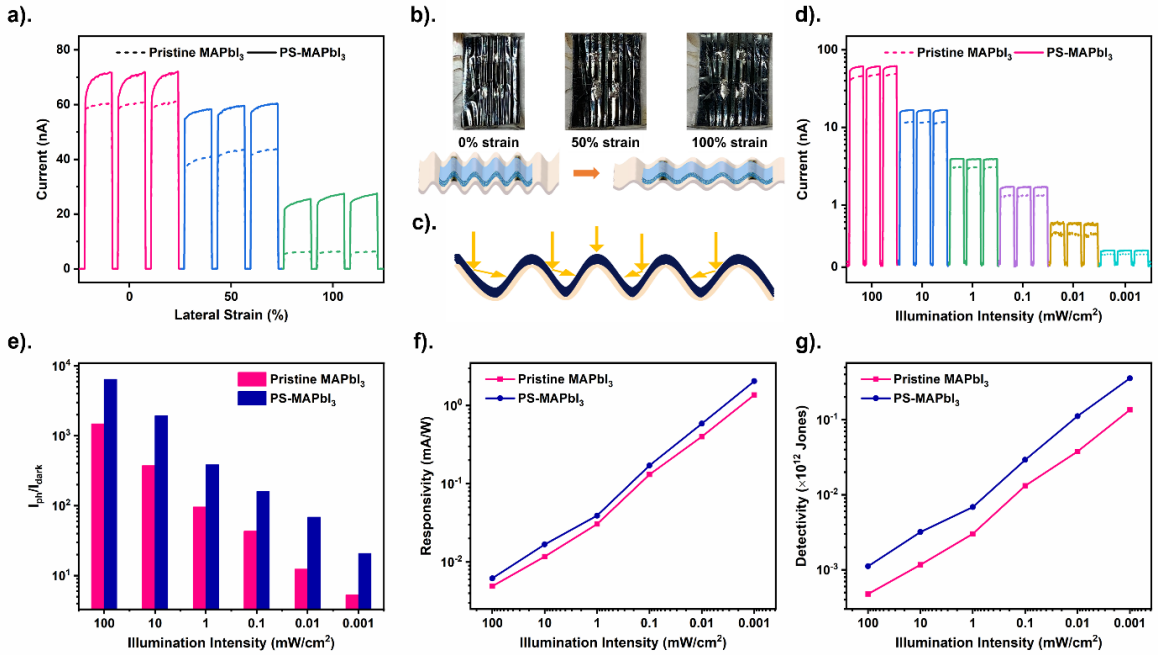

Figure 5.3 Performance, operation mechanism, and configuration of the stretchable photodetector. (a) Photocurrent response of pristine and PS-$MAPbI_3$ films stretched under variable lateral strain at 3.5 V under 1.0 sun illumination. (b) Optical images and schematic representation of variation in wrinkle radius and height as a function of lateral strain. (c) Schematic diagram showing enhanced photon trapping within hills and valleys of wrinkled photodetector at 0% strain. (d) Photocurrent, (e) light switching ratio of photocurrent to dark current, (f) responsivity, and (g) detectivity of pristine and PS-$MAPbI_3$ devices under various illumination intensities at 3.5 V under 50% strain. The distinct colors used in Figures 2a and 2d are meant to clearly distinguish between the photoresponse cycles measured under varying lateral strain and illumination intensity, respectively.

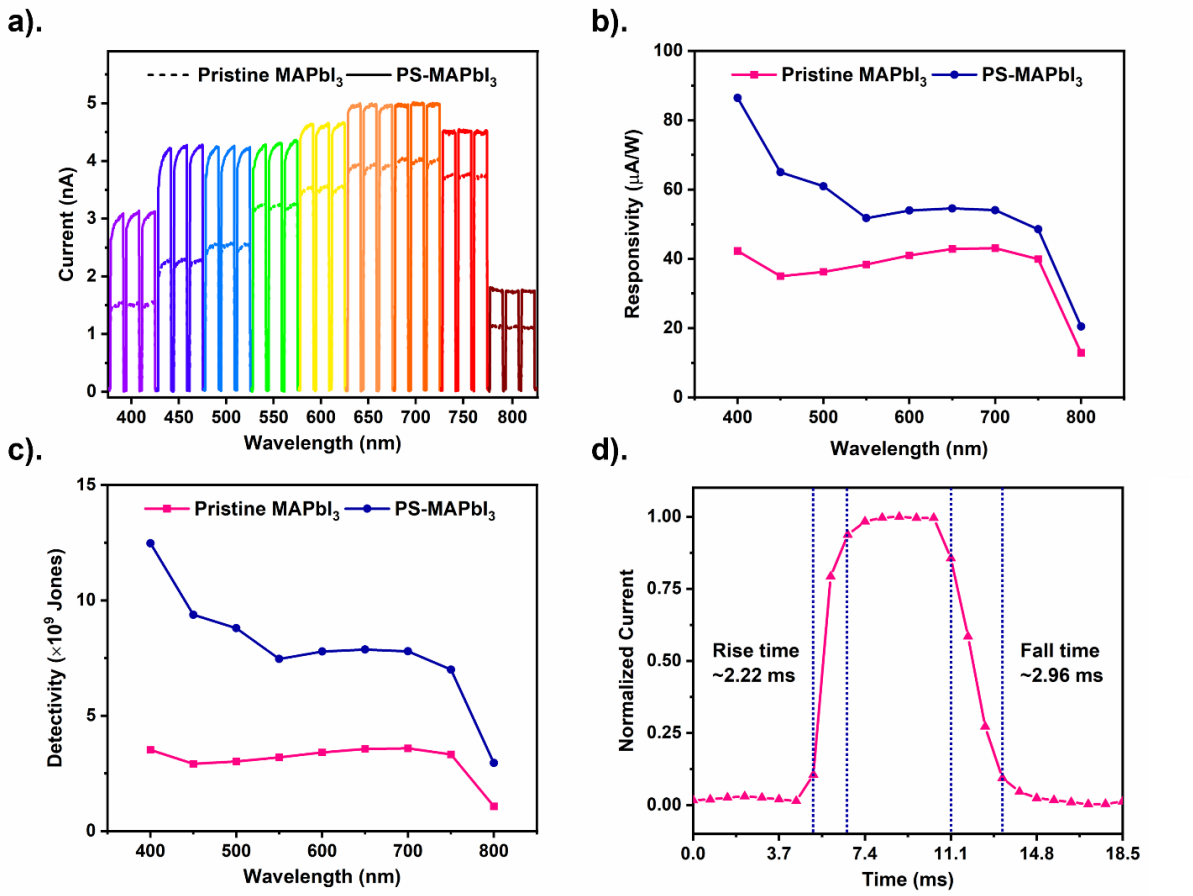

Figure 5.4 Wavelength sensitive response and speed of response of the stretchable photodetector under 50% strain. (a) Photocurrent response, (b) responsivity, and (c) detectivity of pristine and PS-$MAPbI_3$ devices under different wavelength illumination. (d) The response speed of PS-$MAPbI_3$ photodetector under 1 mW cm^{-2} 650 nm light irradiation. The different colors used in Figure 5.3a are meant to distinguish between the photoresponse cycles measured at various wavelengths spread across the visible light spectrum.

The key limitation of stretchable perovskite devices is their mechanical durability and they are typically limited to a few hundred stretching cycles at low strain (Table A5.1).[150, 232-239] To evaluate the mechanical and performance stability, the $MAPbI_3$, and PS-$MAPbI_3$ devices were subjected to 10,000 dynamic stretching and relaxation cycles under 50% lateral strain. With the increase in stretching and relaxation cycles, the performance of the perovskite photodetectors gradually decreases. As seen in Figure 5.5a, the PS-$MAPbI_3$ device maintains 98%, 90%, and 62% of its initial photocurrent value after

5, 100, and 5000 cycles, respectively. Under similar conditions, the performance of pristine $MAPbI_3$ decays significantly as the normalized photocurrent drops by 20% within the initial 5 cycles. After 10,000 cycles of stretching and relaxation, the PS-$MAPbI_3$ device maintains 52% of its performance while the performance in pristine $MAPbI_3$ deteriorates to 22%. We can observe that in pristine $MAPbI_3$, a rapid decay in performance is observed in just the first few stretching cycles. While in the PS-$MAPbI_3$ a more gradual decay in performance is observed. This distinct behavior indicates a drastic change in the $MAPbI_3$ due to the induced stress on stretching, while the PS-$MAPbI_3$ device is not prone to such a failure. The failure mechanism is observed from the FE-SEM images taken after 5 stretching cycles. For pristine $MAPbI_3$ (Figure 5.5b) we observe the formation of micron-sized cracks in the film, in high density, leading to catastrophic failure. While in the PS-$MAPbI_3$ (Figure 5.5c) the formation of cracks is very limited, and their size is significantly reduced. Instead flaking of the top layers is observed, which easily overlap with each other during stretching, maintaining the device's conductivity. Hence this leads to a relatively smaller decline in performance, as observed. The cracks serve as a preferential site for material degradation due to the release of the strain energy, causing the escape of volatile MA^+ and leaving behind PbI_2. As observed in the Raman spectra (Figure A5.5), the intensity of the sharp Pb–I liberation mode band at 85 cm^{-1} is maintained across the smooth and cracked regions of both pristine and PS-$MAPbI_3$ films, while the intensity of the broad-band corresponding to the MA^+ torsional mode in $MAPbI_3$ decreases at the cracked regions. In the case of $MAPbI_3$ films, the deterioration of the MA^+ signal at the cracks is significantly more severe than in comparison to the PS-$MAPbI_3$ film. This further confirms the basis of rapid loss in performance and stability of the $MAPbI_3$-based device.

The difference in mechanism for releasing stress (due to stretching cycles) between the two materials ($MAPbI_3$ and PS-$MAPbI_3$) points to a key difference in their mechanical properties. Figure 5.5d and e represent the images corresponding to Young's modulus of pristine $MAPbI_3$ and PS-$MAPbI_3$ films, respectively, obtained using the PF-QNM mode of an AFM. The PF-QNM AFM offers the advantage over traditional indention by avoiding plastic deformation of the sample and therefore prevents alteration of perovskite material during measurements.[253-255] The nanomechanical maps show substantial variation in local stiffness within the perovskite thin films. The pristine perovskite films show an average modulus of 11.4 GPa.[256, 257] In contrast, the PS-$MAPbI_3$ films have a lower modulus of 7.1 GPa. Interestingly, the intra-granular region in the perovskite films exhibits a lower modulus while the grain boundaries are relatively stiff.[258] Specifically, the modulus within grains in PS-$MAPbI_3$ and $MAPbI_3$ averages 4.7 and 8.1 GPa, respectively. While the modulus at grain boundaries is 12.4

GPa in PS-$MAPbI_3$ film in comparison to 18.5 GPa as observed in pristine $MAPbI_3$ films. The ease of formation and propagation of cracks in a film is indicated by its fracture toughness (K_{IC}) and critical value of the strain energy release rate (G_c). Due to the brittle nature of the perovskites, their K_{IC} and G_c values are ~0.145 $MPa.m^{1/2}$ and 1.0 J/m^2 respectively.[259, 260] While the K_{IC} and G_c values for PS are ~1.0 $MPa.m^{1/2}$ and >100 J/m^2, respectively due to its ability to dissipate mechanical energy.[261, 262] During stretching, both $MAPbI_3$ and PS-$MAPbI_3$ films experience similar strain magnitudes, given their almost identical wrinkle profile. However, due to the lower modulus of the PS-$MAPbI_3$ films, the stress generated in them will be lower. This is also evident from the formation of cracks only in the direction perpendicular to the applied strain (during stretching) in PS-$MAPbI_3$ films. While in the pristine $MAPbI_3$ films, the strain generated in both the lateral directions (from stretching in one direction and the compressive strain generated in the other lateral direction and vice versa during cycling) leads to cracking across the whole film.[263] Combined with the greater K_{IC} and G_c of the PS component, the PS-$MAPbI_3$ films can sustain the stretching by flaking and without catastrophic failure. Further evidence of the film's ability to dissipate energy and hence prevent cracking is shown in Figure 5.5f and g, the average dissipated energy is 4.73 keV for pristine $MAPbI_3$ films in comparison to 4.95 keV for PS-$MAPbI_3$ films. The images show that the applied elastic energy during PF-QNM is better dissipated by the PS-$MAPbI_3$ films, due to their viscoelastic PS component which will reduce their cracking during stretching cycles.

The photodetectors were also tested for the reliability of photoresponse and potential material degradation at high applied external bias and intense illumination (Figure 5.5h). Under a prolonged 1.0 sun illumination at 3.5 V, both pristine and PS-$MAPbI_3$ devices stretched at 50% exhibit a continuous photoresponse. Moreover, the photocurrent response in PS-$MAPbI_3$ gradually increases until getting stabilized at 50 min of light exposure at a 1.4 folds higher value (75.36 nA) in contrast to pristine $MAPbI_3$ (52.58 nA). The long-term operation stability of pristine $MAPbI_3$ and PS-$MAPbI_3$ devices stored in an ambient environment (in the air with a relative humidity of 35-40% under room light) was likewise assessed and presented in Figure 5.5i. The pristine $MAPbI_3$ device initially undergoes photoinduced and moisture-facilitated accelerated degradation in an oxygen-rich atmosphere and suffers a 50% decay in performance within 7 days of fabrication. The residual perovskite material then undergoes steady decomposition to PbI_2 and the photodetector device exhibits negligible response after 30 days.[114, 131] On the contrary, the PS-$MAPbI_3$ photodetector experiences a minimal decay of 5% within 7 days of fabrication and maintains 75% of performance even after 30 days. The enhanced

performance can be ascribed to the minimal leaching of moisture and O_2 in the polymer integrated perovskite film owing to the passivation of grain boundaries and the presence of a thin nanometer-scale interfacial layer of hydrophobic PS at the top and bottom interfaces of the device.[119]

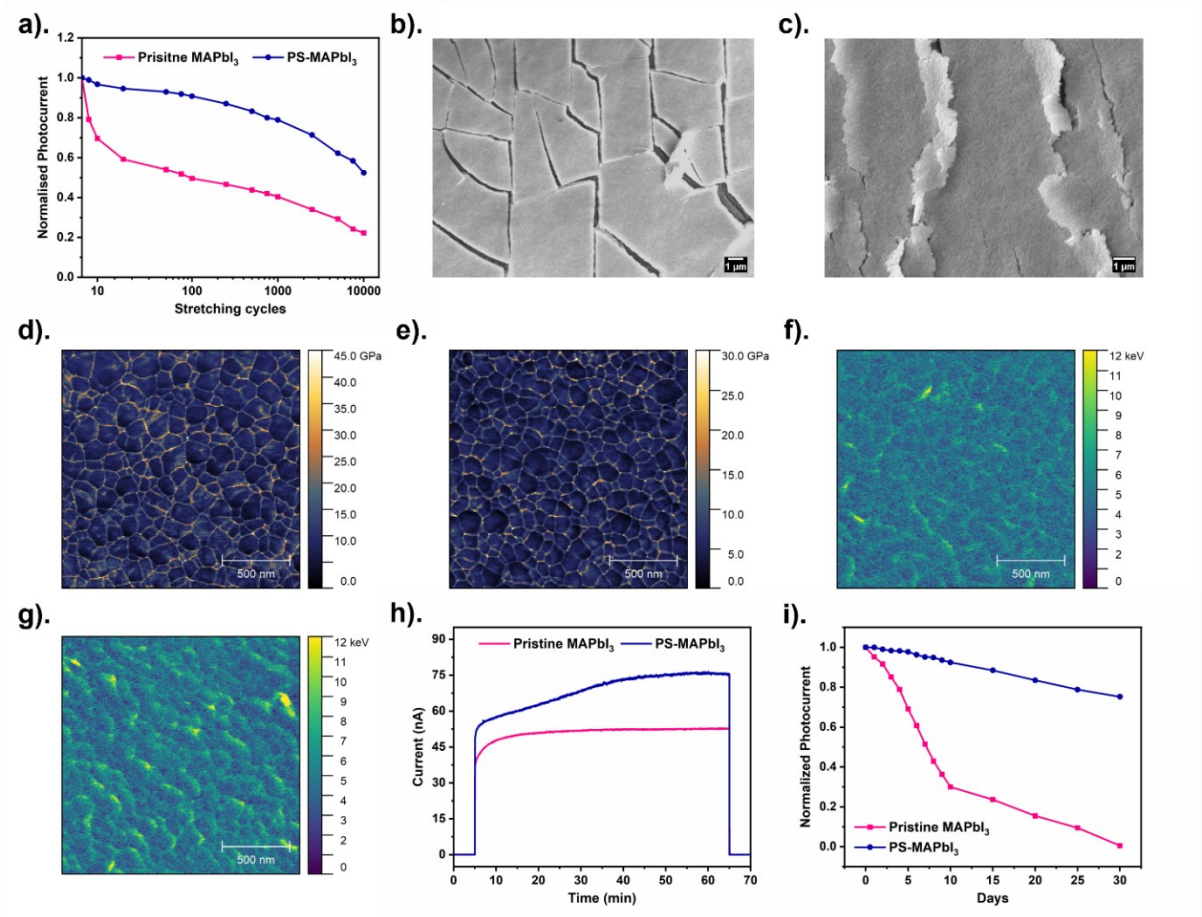

Figure 5.5 Performance during stretching cycles, mechanical properties, and stability characteristics of as-prepared stretchable devices. (a) Normalized photocurrent response of pristine and PS-$MAPbI_3$ photodetectors when subjected to 10,000 stretching cycles at 50% strain. (b-c). FE-SEM images, (d-e) Young's modulus, and (f-g) dissipation energy maps of pristine and PS-$MAPbI_3$ films, respectively. (h) Operational stability of the devices at a constant bias of 3.5 V under 100 mW cm^{-2} intensity. (i) Normalized photocurrent of the devices after aging continuously in ambient air, 35-40% relative humidity, and under room light for 720 h (30 days).

The ability of the device to function under continuous stretching cycles (10,000) also requires the stability of the electrodes. The electrodes based on Pt-Au nanochains maintain high conductivity even after ten thousand stretching cycles (Figure 5.6a). As seen in the FE-SEM image (Figure 5.6b), due to the inherently tangled nanochain mesh, very small nanoscale size cracks are formed in the electrodes in response to the stretching cycles. Due to the entangled chain structure, electrical contact is maintained between adjacent cracks, allowing the flow of charge carriers within flakes separated by a few nanometers (Figure 5.6c). Such high mechanical durability and excellent conductivity eliminate the possibility of underlying electrodes being a bottleneck in the photodetector performance.

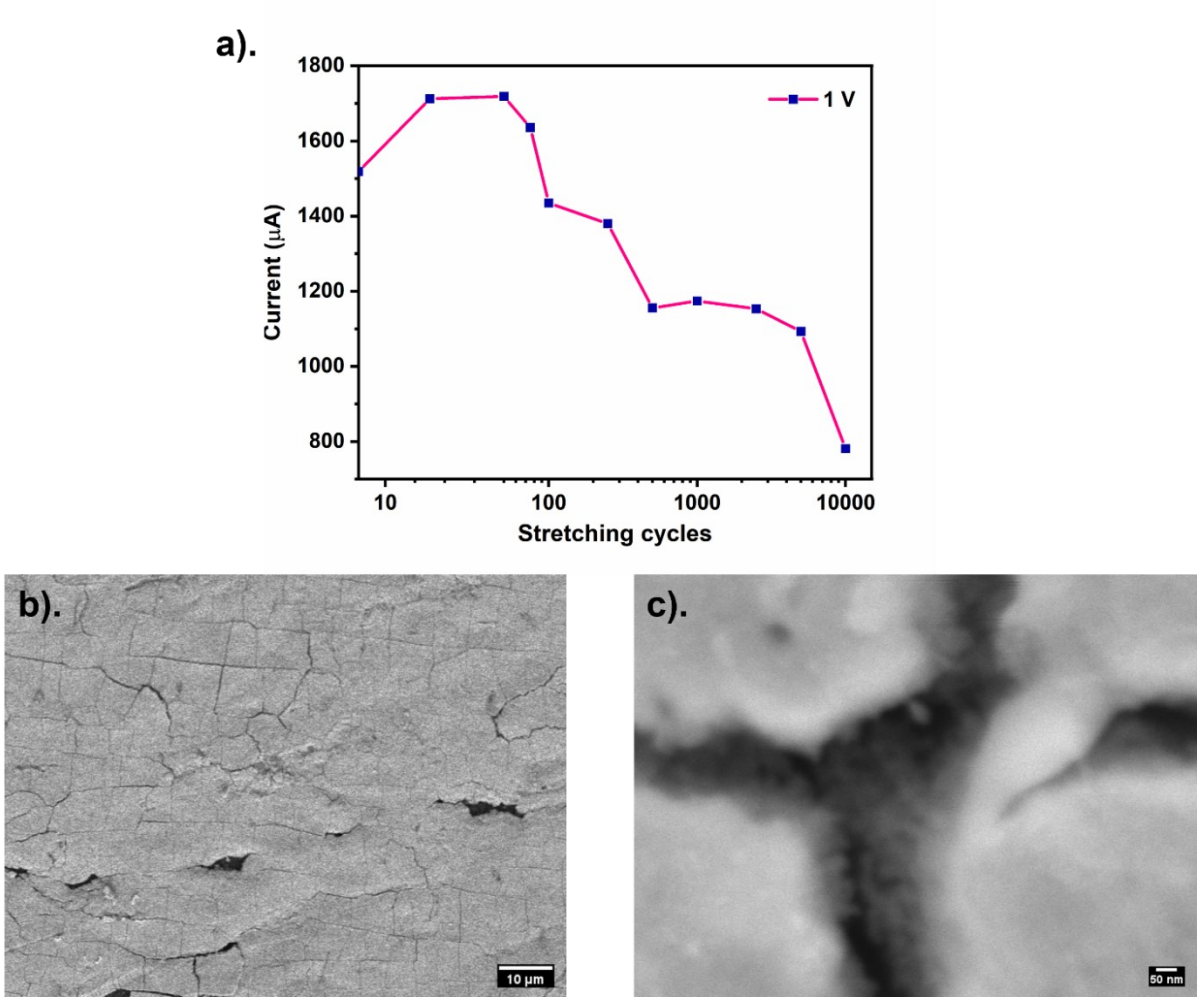

Figure 5.6 (a) The current response of Pt-Au electrodes at 1 V, sustaining high conductivity during stretching cycles. (b-c) FE-SEM images of Pt-Au electrodes after 10,000 stretching cycles. The nanochains mesh undergoes rearrangement and remains intermittently connected at cracks.

5.4 Conclusion

In conclusion, the current work presents a simple assembly of highly conductive solution-processed metallic Pt-Au nanochains-based electrodes integrated with perovskite films to yield highly stretchable wrinkled structure photodetectors with excellent mechanical durability. The polymer integrated perovskite devices (PS-$MAPbI_3$) outperform pristine $MAPbI_3$ devices and exhibit high photocurrent, ultralow dark currents, and extreme stability under high lateral strain. The 1 wt/v % PS-$MAPbI_3$ device exhibits maximum responsivity and detectivity of 2.05 mA W^{-1} and 0.36×10^{12} Jones, respectively. The lower modulus of polymer and its greater dissipation of energy enables softening of the otherwise rigid perovskite film and leads to high mechanical durability in PS-$MAPbI_3$ photodetector as it maintains 52% of device performance after 10,000 stretching cycles at a strain of 50%. The discussed low-cost, highly flexible device will serve as a strong foundation for developing portable optoelectronic devices such as LEDs and solar cells, based on the integration of organic and inorganic components. Besides, careful selection of heterogenous metal ions for self-assembling gold nanoparticle chains may further pave the way for realizing Schottky barrier facilitated perovskite-based self-powered stretchable devices.

Chapter 6
Polymer Stabilized Halide Perovskite-Based Large Area Solar Cells with Improved Device Characteristics

6.1 Introduction

Despite exhibiting stability issues in the ambient atmosphere, halide perovskite-based solar cells have reached record efficiency limits and are being seen as a potential substitute for the energy-intensive silicon photovoltaic technology.[84, 264] However, perovskite solar cells reported with such high power conversion efficiency (PCE) often have an effective active area of less than 0.1 cm^2.[265, 266] In comparison, the effective active area in commercial silicon solar panels is >200 cm^2. Small active area-based solar cells suffice the need for scientific demonstration and serve as a prototype for potential technological developments. However, they lack commercial viability. To fabricate perovskite-based solar cells for practical use, stable independent perovskite thin film-based solar cells with a bare minimum area of 1 cm^2 and high power conversion efficiency need to be fabricated.[267] Only then can such perovskite-based solar cells yield effective performance when arranged in form of a module.[268]

There exist two main factors that limit the upscaling and commercialization of perovskite-based solar cells. Firstly, the challenge of coating pinhole-free large area films, and secondly but more importantly, the degradation of perovskite in the ambient atmosphere by external (in presence of O_2, light, moisture, and temperature) and internal factors (ion migration).[83, 269] The prevalent method of spin coating is not the most feasible solution for producing large area perovskite films. Due to the uneven centrifugal force in the prevalent spin-coating process, the thicknesses at the center and the edge of the substrate turn out different, especially for large area films. The thick area at the edges shows increased nonradiative recombination loss while the thinner area at the center may show reduced light-harvesting ability and increased pinholes, leading to reduced efficiency.[270]

To address these issues and move closer toward the manufacturing of large area perovskite films, developing large area coating methods is necessary. So far, various methods have been applied to large area film fabrication, including spray coating, dip coating, slot-die coating, and blade-coating.[271, 272] Among these techniques, blade-coating has achieved the greatest success and has been most widely recognized. Blade coating offers several advantages such as the ability to be utilized with a wide range of fluids with variable viscosities, the potential of tweaking film parameters (such as film thickness),

and the feasibility of coating the entire device using the same technique (charge transport, interfacial and encapsulation layers).[273, 274] However, the majority of the reports focusing on the blade coating technique published so far either mandate an inert atmosphere or need simultaneous heating alongside film coating to evaporate the solvent.[44] This fails the aim of achieving facile and cost-effective manufacturing of large area perovskite films in an ambient atmosphere.

The current work utilizes a facile room-temperature blade coating technique for fabricating large area perovskite films in ambient conditions with an active area of 1 cm^2. To address the challenge of stability under normal operating conditions, we utilize a versatile polymer additive strategy by integrating polystyrene (PS), a commodity scale polymer having the ability to undergo interaction with both the perovskite ($MAPbI_3$) precursors. While the Lewis acid characteristics of the PbI_2 lead to cross-linking of PS primarily at the grain boundaries and interfaces of the perovskite film, the extra energy owing to the cation-π interaction between the PS and MA cation can induce thermal stability in the composite film. The polystyrene (PS)-incorporated $MAPbI_3$ (PS-$MAPbI_3$) solar cell exhibits a higher PCE of 6.85% and can sustain 82% of its initial performance for 7 days when exposed to an ambient atmosphere. In comparison, the PCE in the pristine $MAPbI_3$ device (5.04%) is reduced to 54% in the same duration. The PS-$MAPbI_3$ devices also have reduced hysteresis compared to pristine perovskite solar cells. The key to higher short-circuit current density (Jsc), open-circuit voltage (Voc), better fill factor (FF), and hence, higher PCE is the integration of PS in the perovskite films which improves crystallinity and grain size in the perovskite film leading to better mobility and carrier lifetime. The presence of insulating hydrophobic PS chains also leads to a three-layer nanoscale trilayer architecture where the thin layer of polymer present at the top and bottom interfaces act as a defensive barrier against external degradation factors such as O_2 and moisture. More importantly, the cross-linked PS omnipresent across the bulk of the perovskite interlayer passivate the trap and defect sites leading to reduced ion migration across the grain boundaries owing to its insulating nature. This simple and scalable single-step blade coating fabrication process at room temperature with the use of a low-cost polymer additive is crucial for the cost-effective commercialization of thin-film solar cells based on hybrid organolead halide perovskites.

6.2 Experimental Section

6.2.1 Synthesis of perovskite precursor solution

The pristine $MAPbI_3$ precursor solution was prepared by mixing 38.1 mg of methylammonium iodide (>99.99%, Greatcell Solar Materials) and 110.6 mg of lead iodide (>99.999% trace metals basis, Sigma-Aldrich) in a mixed solvent of 4 µl of N-Methyl-2-pyrrolidone (anhydrous, 99.5%, Sigma-Aldrich), 14 µL of dimethyl sulfoxide (anhydrous, ≥99.9%, Sigma-Aldrich) and 182 µl of N, N-dimethylformamide (anhydrous, 99.8%, Sigma-Aldrich) to get a 1.2 M solution. To obtain the polymer-perovskite solution, an optimized concentration of 2 mg of PS (average M_w 35 kDa and PDI of 1.02, Sigma-Aldrich) was introduced as an additive in the perovskite precursor solution. The solution was later stirred on a magnetic stirrer for 30 minutes to allow sufficient interaction, before blade-coating in the ambient atmosphere.

6.2.2 Fabrication of perovskite-based large area solar cells

To understand the influence of PS over the electro-optical properties of the resultant perovskite-polymer composite films when prepared over a large area, vertical solar cells in the n-i-p configuration were fabricated. For typical device fabrication, 2.5×2.5 cm indium tin oxide (ITO) coated glass substrate (20 Ω sq^{-1}, Ossila) was first sequentially washed and ultrasonicated in Millipore water, acetone, and isopropanol for 15 minutes each. After re-washing with Millipore water and drying with N_2, the ITO substrates were treated with UV Ozone to remove organic moieties. The SnO_2 solution (15% in H_2O colloidal dispersion, Alfa Aesar) was diluted at 1:6.5 by H_2O and then spin-coated on the cleaned ITO at 4000 rpm for 30 seconds. The substrate was annealed at 150°C for 30 min to form a compact SnO_2 layer. 20 µl of the perovskite precursor solution was put on edge of the substrate and a universal film applicator with a blade gap of 150 was linearly moved at a speed of 7 mm/sec. An N_2 knife was moved simultaneously along the film applicator to dry the wet film. The intermediate perovskite film was later subjected to sequential annealing at 80 °C for 2 min and 120 °C for 5 min, respectively to complete the perovskite phase transformation. Finally, a solution consisting of 72 mg of 2,2',7,7'-tetrakis(N,N-di(4-methoxyphenylamino)-9,9'-spirobifluorene (spiro-MeOTAD), 17.5 µL of lithium bis(trifluoromethanesulfonyl)imide (Li-TFSI) (520 mg Li-TSFI in 1 mL acetonitrile) and 28.8 µL of 4-tert-butyl pyridine in 1 mL of chlorobenzene, was spun at 3500 rpm for 30 sec onto the perovskite film to obtain the hole transport layer. The devices were completed by evaporating 100 nm

gold in a vacuum chamber using a shadow mask to pattern the electrodes. After gold deposition, devices were mechanically scribed into an active area of 1 cm^2.

6.2.3 Structural, microscopic, and contact angle characterization

The grazing incidence X-ray diffraction (GIXRD) patterns of obtained samples were measured using a PANalytical X'Pert Pro MRD diffractometer with Cu Kα radiation (λ = 1.54 Å) at an incidence angle of 0.4°. The X-ray diffraction (XRD) was characterized using PANalytical Empyrean diffractometer with Cu Kα radiation (λ = 1.54 Å). A Zeiss Ultra plus field emission scanning electron microscopy (FE-SEM) equipped with energy-dispersive X-ray spectroscopy (EDX) was used to examine the surface topology and average grain size distribution in the pristine and polymer integrated perovskite films. The contact angles were measured using a standard automated contact angle goniometer (Rame-Hart, Model 190 CA) with deionized water.

6.2.4 Electrical measurements

The current density-voltage (*J-V*) characteristics of the vertical device configuration of ITO/SnO_2/$MAPbI_3$ (polymer-$MAPbI_3$)/spiro-MeOTAD/Au large area solar cell was measured in the ambient atmosphere using a CompactStat electrochemical interface & impedance analyzer under simulated AM 1.5 global irradiation (100 mW cm^{-2}) generated using a Xenon-lamp based solar simulator (Newport Oriel Instrument 67005, 150 W Solar Simulator). Before the device measurement, the solar simulator was calibrated using an NREL-certified KG5 silicon reference cell to minimize any spectral mismatch. All *J-V* measurements were recorded from 1.2 to -0.2 V at a scan rate of 100 mV s^{-1} and step size of 10 mV. The hysteresis index of the devices was calculated by: Hysteresis index = $(PCE_{reverse}-PCE_{forward})/PCE_{reverse}$.[275] The long-term stability test of the devices was tested by aging the devices in an ambient atmosphere under room light with 30−40% relative humidity. The humidity was measured by a portable RH sensor.

6.3 Results And Discussion

Figure 6.1a represents an optical image of an as-fabricated perovskite film. The quality of the perovskite film depends heavily on the deposition conditions. Most of the previous reports focusing on large area coating typically employ a hot-casting method where the substrate and perovskite solution is heated during the coating process.[276-281] The heat induces the direct formation of the perovskite phase by skipping the intermediate wet film phase. However, it may lead to enhanced heterogeneous nucleation

leading to smaller grain size and enhanced grain boundaries in the as-fabricated perovskite films, and simultaneously compromises the feasibility of device fabrication. On the contrary, in this work an air blade, a pressurized air plenum with a narrow nozzle through which pressurized N_2 flows, has been utilized. The constant linear flow of N_2 serves three purposes: 1) It allows uniform spreading of the perovskite solution over the substrate, 2) It aids in evaporation of the perovskite precursor solution (without requiring heating) inducing slow nucleation in the wet film, and 3). It alleviates the requirement of an antisolvent treatment of the as-fabricated films.[282] Further, the use of a mixture of perovskite precursor solvents facilitates the coating of the perovskite solution at room temperature. Owing to their relatively lower vapor pressure, the addition of N-methyl-2-pyrrolidone (0.29 mmHg, 20 °C) and dimethyl sulfoxide (0.42 mmHg, 20 °C) in the N, N-dimethylformamide solvent (2.7 mmHg, 20 °C) delays the overall evaporation of the solvent mixture.[283] Hence, the processing time within which the intermediate wet film needs to be annealed to complete the perovskite phase transformation is increased. Such retarded crystallization leads to large grain size and higher crystallinity in the as-fabricated perovskite films as evident from the X-ray diffraction patterns.

The X-ray diffraction (XRD) pattern of the pristine and PS-$MAPbI_3$ film, as seen in Figure 6.1b, representative of diffraction by the bulk film material, showcases sharp diffraction peaks corresponding to the (1 1 0), (2 2 0), and (3 1 0) lattice planes of the $MAPbI_3$. While no impurity peaks are observed in the bulk XRD pattern, an additional diffraction peak at 2θ of 12.7° is observed in the grazing incidence X-ray diffraction (GIXRD) pattern (Figure 6.1c). This can be accredited to the formation of PbI_2 at the perovskite interface owing to limited degradation occurring during the fabrication and measurement of the films in the ambient atmosphere.[131, 156] The absence of the PbI_2 impurity peak in the XRD occurring from the bulk perovskite material confirms that the degradation of perovskite films is limited to the top interface. Both bulk and GIXRD patterns confirm that the addition of PS does not alter the tetragonal phase of the perovskite. However, the intensity of the PbI_2 impurity peak observed in the GIXRD pattern of PS-$MAPbI_3$ film reduces significantly. This confirms improved perovskite phase transformation in the PS-$MAPbI_3$ films and the ability of PS present at the perovskite top interface to act as an effective barrier against external degradation factors. This is in line with our previous work, where it has been shown that the PS and perovskite form a nanoscale tri-layer architecture where the hydrophobic polymer forms a thin layer at the bottom and top interfaces while the $MAPbI_3$ forms the bulk of the interlayer.[119] Further, the FWHM values for the diffraction peak intensity in the GIXRD pattern increase in comparison to that observed in the bulk XRD pattern. This

can be ascribed to the crystallization of the perovskite material occurring in the bottom-to-top direction similar to the transfer of heat energy during the annealing of the perovskite thin film. This is reflected in the reduced crystallinity of the interfacial perovskite grains with respect to the underlying grains.

The observance of PbI_2 in the GIXRD pattern is significant since previous reports highlighting N_2-assisted blade coating of perovskite films solely utilize bulk XRD (and not GIXRD) and hence, the as-fabricated perovskite films cannot be conclusively considered to be free of interfacial degradation.[284] Further, those involve the use of additives as high as 20% which can alter the overall stoichiometry and arguably lead to the formation of mixed perovskite.[285, 286]

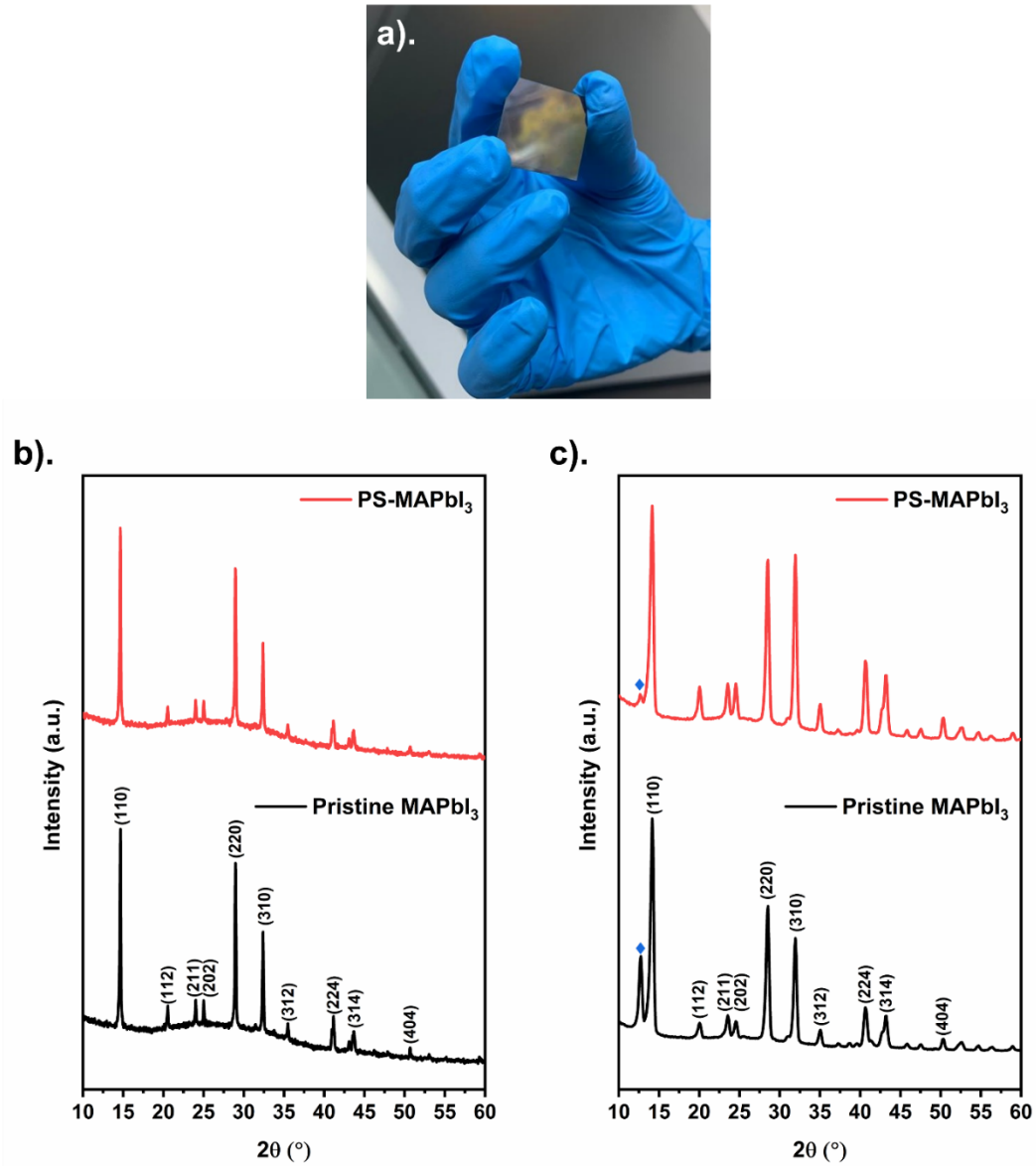

Figure 6.1 (a) Optical image of a room temperature blade coated perovskite films. (b) Bulk and (c) GIXRD pattern of pristine $MAPbI_3$ and PS-$MAPbI_3$ film.

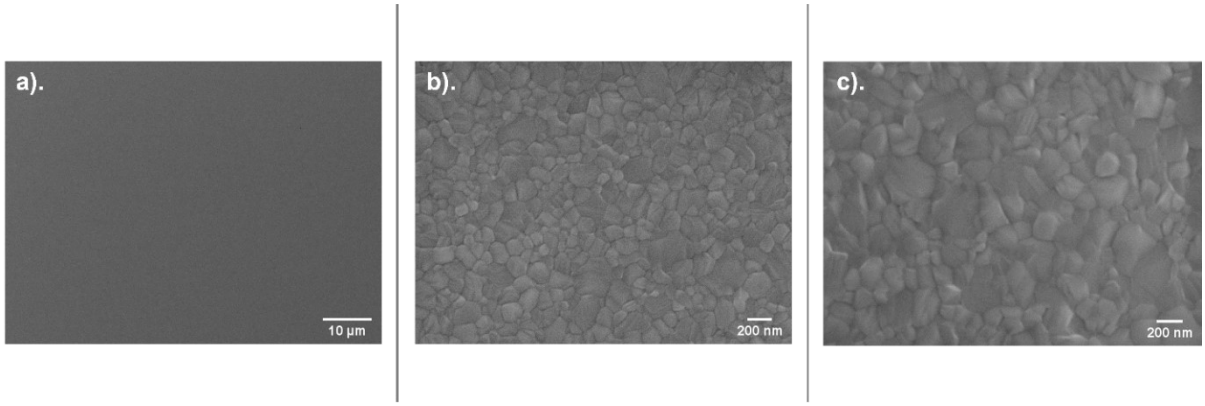

Figure 6.2 Scanning electron micrographs of room temperature blade coated perovskite films: (a) Pinhole-free compact uniform film over a large area, (b) Pristine $MAPbI_3$, and (c) PS-$MAPbI_3$.

The top surface scanning electron microscopy (SEM) image shows the formation of uniform compact pin-hole-free perovskite film over the entire large area substrate (Figure 6.2a). Considering the naturally formed grooves on top of the perovskite films representative of the grain boundaries, the average grain size observed in pristine $MAPbI_3$ is 103 nm (Figure 6.2b and Figure A6.1a). The integration of PS in the perovskite films leads to an increase in the average grain size to 180 nm (Figure 6.2c and Figure A6.1b). This relative increase in the grain size follows the increase in the crystallite size (65.42 nm in pristine $MAPbI_3$ and 81.78 nm in PS-$MAPbI_3$) calculated using Scherrer's equation based on the X-ray diffraction pattern. There exists specific molecular-level interaction between perovskite precursors and PS which has been previously characterized by Raman spectroscopy, gel permeation chromatography, and the growth of single perovskite crystals.[37, 75] Such direct interaction of the PS chains with the perovskite precursors modulates the crystallization kinetics favorably to allow complete phase transformation and improves grain growth in the PS-$MAPbI_3$ film as confirmed by the GIXRD pattern and SEM images.[74]

Figure 6.3a shows the effect of the polymer additive on the current density-voltage (*J-V*) in pristine and polymer-perovskite films. The pristine $MAPbI_3$ exhibits Jsc and Voc values of 9.55 mA/cm^2 and 1.03 V. The Jsc and Voc value enhances with the integration of polymer in the PS-$MAPbI_3$ composite films. The PS-$MAPbI_3$ large area solar cell displays higher Jsc and Voc values of 12.75 mA cm^{-2} and 1.05 V, respectively with a significantly alleviated hysteresis effect. The FF and PCE values increase from 0.49 and 5.04% in pristine $MAPbI_3$ to 0.50 and 6.85%, respectively in the PS-$MAPbI_3$ device. The forward and reverse *J–V* scans of the 1 wt/v % PS films show a 3.5-fold reduced hysteresis index of 0.04

compared to 0.14 for pure $MAPbI_3$ (Figure A6.2). The detailed parameters for the hysteresis analysis are listed in Table A6.1. The considerable reduction in the hysteresis can be ascribed to the insulating nature of PS which leads to reduced ion migration across the grain boundaries as discussed below.

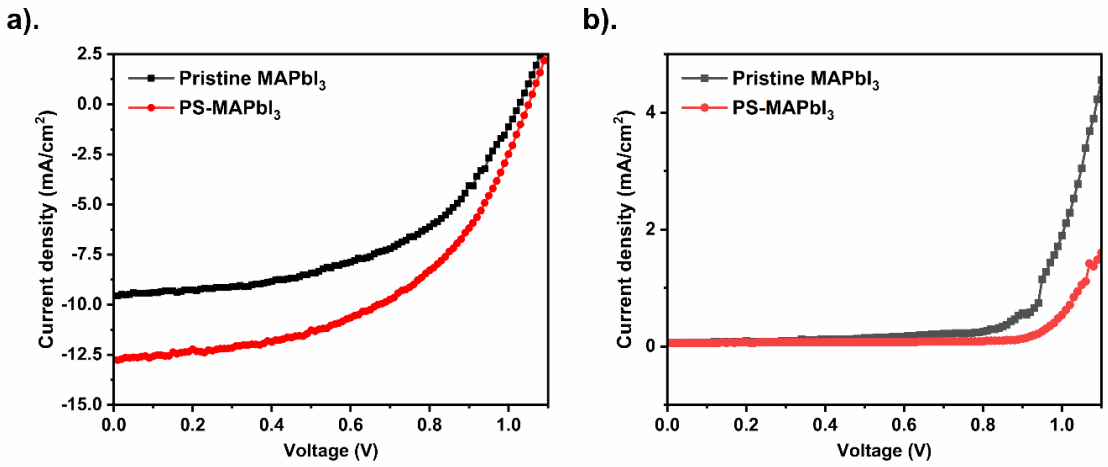

Figure 6.3 Effect of cross-linked PS chains on the perovskite photovoltaics performance. *J-V* characteristics of pristine and PS-$MAPbI_3$ large area solar cells in (a) light and (b) dark.

The dark currents observed in perovskite devices can be considered direct representative of the inherent ion migration effect. The mobile MA^+ and I^- ions with low activation energy drift towards electrodes with opposite polarity often leading to ion depletion and negatively affecting the stoichiometry of the $MAPbI_3$ eventually leading to internal degradation of the perovskite film. The *J–V* curves measured in the dark (Figure 6.3b) show that the current density decreases in the polymer-perovskite hybrid film, revealing that the electrically insulating nature of PS reduces the ion migration effects in these devices.[118]

Similar to the previously published work from our group, the PS-$MAPbI_3$ solar cells exhibit better figures of merits in comparison to the pristine $MAPbI_3$ devices. However, the electro-optical properties observed for the blade-coated devices are relatively poorer than that observed for the solar cells with smaller active areas fabricated using the conventional spin coating technique.[37] This is not surprising though, as, in the current case of large area solar cells, although the perovskite layer has been coated utilizing the air knife-assisted blade coating technique, the charge transport layers coated using the spin coating technique can limit the overall performance due to retarded charge transfer across the non-

uniform perovskite/ transport layer interface. There also exists considerable scope for enhancement in the device characteristics by optimization of the parameters associated with the blade coating technique.

Despite exhibiting high photovoltaic efficiency, a critical factor in the long-term operation of perovskite-based solar cells is their long-term stability. Degradation in perovskite films results from two primary factors, the first from exposure to environmental elements such as oxygen and moisture and the second due to internal degradation via ion migration. To assess the ability of the perovskite films to survive in presence of ambient moisture, contact angle measurements were utilized to assess their hydrophobicity. The contact angle (Figure 6.4a and b) and thus the hydrophobicity was observed to increase in the polymer-perovskite films (71.6°) with respect to the pristine $MAPbI_3$ film (62°). The improved contact angle in the perovskite films with the presence of PS additive compliments the XRD data and suggests that its hydrophobic nature can effectively provide a cushion against external degradation factors and suppress moisture invasion. Upon exposing these as-fabricated films in an ambient atmosphere for a week in room light, the normalized PCE in pristine $MAPbI_3$ reduces to 70% within two days and 54% within 7 days (Figure 6.4c). In comparison, the PS-$MAPbI_3$ device as the polymer-perovskite solar cell maintains 82% of its initial PCE for 7 days. The improved stability of the PS-$MAPbI_3$ solar cell can be ascribed to the combined effect of two factors. Firstly, the crucial role of the interfacial PS (hydrophobic)-rich layer which acts as a barrier against oxygen and moisture, and secondly, the passivation of grain boundaries across the perovskite-rich interlayer.

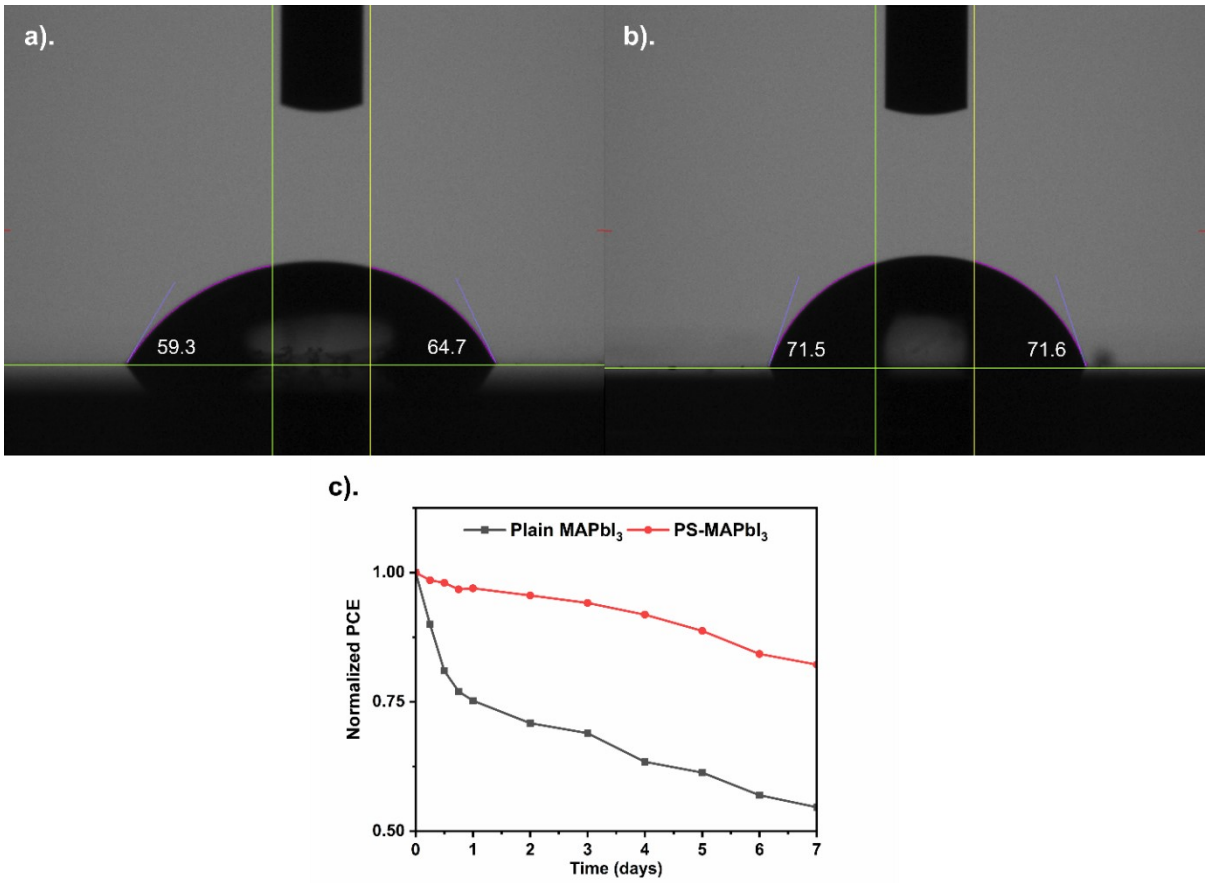

Figure 6.4 Enhanced device stability owing to the hydrophobic nature of PS chains. Contact angle images of (a) pristine $MAPbI_3$ and (b) PS-$MAPbI_3$ film and (c) Trend of normalized power conversion efficiency for pristine and polymer-perovskite solar cells after aging in ambient atmosphere.

6.4 Conclusion

In conclusion, the current work presents a single-step facile blade coating method for integrating a commodity scale polymer, PS within perovskite films to yield uniform compact pin-hole free large area perovskite films. The polymer integrated perovskite devices outperform the pristine $MAPbI_3$ devices and exhibit high Jsc (12.75 mA/cm^2) and Voc (1.05 V), lower dark currents, and high PCE (6.85%). The improved performance in the PS-$MAPbI_3$ can primarily be ascribed to the improved crystallinity, larger grain size, and reduced ion migration across the grain boundaries owing to the passivation of trap and defect states by the cross-linked PS. The hydrophobic nature of PS enables prevention against moisture seepage in the ambient atmosphere as the PS-$MAPbI_3$-based solar cell maintains 82% of its

initial device performance for 7 days despite the absence of an encapsulation layer. The discussed facile cost-effective blade coating fabrication method for integrating PS additive in perovskite films serves the dual purpose of addressing the challenges of developing large area perovskite film-based devices which can survive in the ambient atmosphere without compromising on efficiency. The versatile polymer-perovskite additive strategy and room temperature blade coating technique can thus be effectively combined for fabricating perovskite-based large area solar cells, LEDs, display devices, sensors, and self-powered applications, bringing them one step closer to commercial production.

Chapter 7
Conclusion and Future Work

7.1 Conclusion

The excellent inherent electro-optical properties of organolead halide perovskites including direct band gap, absorption across the entire visible range, high absorption coefficient, impressive carrier mobility and lifetime, and low-temperature solution processibility make them an optimum material choice for developing cost-effective highly efficient photosensitive devices. The major challenge of stability associated with these perovskite-based devices has been effectively addressed in this thesis by capitalizing on the specific molecular-level interaction between PS and $MAPbI_3$ precursors. The favorable alteration in structural, spectroscopic, mechanical, and electro-optical characteristics of these polymer-perovskite hybrid films will pave the way for bringing these perovskite-based devices to the commercial market. The viscoelastic nature and lower modulus of the PS additive can be capitalized to extend the polymer-perovskite films beyond rigid substrates and realize flexibles with enhanced durability by preventing their catastrophic failure. Such a single-step strategy also provides the potential of being upscaled for developing large area devices.

Chapter 2 establishes that CO gas molecules interact strongly with the top interface of $MAPbI_3$ film and lead to a significant change in the physicochemical properties and energy level alignment. It is realized that short exposure to CO induces n-type doping at the perovskite top interface, while longer exposure leads to excessive loss of MA^+ leaving behind residual PbI_2. Hence, while a short burst of CO can be utilized to enhance the self-powered ability in the $MAPbI_3$ films owing to enhanced extraction of charge carriers at the top interface due to the formation of a p-n junction, longer exposure proves detrimental to the device's performance and stability.

In Chapter 3, it was deduced that the structural, morphological, spectroscopic, hydrophobicity and electro-optical properties of the perovskite can be tuned by utilizing polymers of contrasting nature. The hydrophilic polar PEG and the hydrophobic non-polar PS are utilized in the block co-polymer system to elucidate their contribution when present together. It is understood that hydrophobic PS is mandatory to produce ambient atmosphere stable perovskite films.

Chapter 4 establishes that the molecular weight or the chain length determines the rearrangement of the polymer across the depth of the perovskite film as a function of its mobility and volume. The molecular

weight hence plays a key role in altering the perovskite crystallization kinetics and affects its grain size. The insulating nature of the polymer further modulates the electronic charge transport and ion migration. Owing to a combination of these effects, utilization of 35 kDa molecular weight of PS leads to optimal performance in the as-fabricated polymer-perovskite hybrid devices.

Chapter 5 highlights that the rigid and brittle polycrystalline perovskite films can be softened by PS additive engineering. The lower mechanical modulus and viscoelastic nature of the polymer are effectively used to realize a stretchable perovskite-based photodetector that can survive 10000 stretching cycles while maintaining 52% of initial performance. The key to improved stability in PS-$MAPbI_3$ devices lies in the enhanced dissipation of the mechanical energy and the contrasting failure mechanism in the pristine and polymer-perovskite films.

Chapter 6 showcases the versatile nature of the PS additive strategy to be extended beyond the conventional spin coating technique and realize blade coating of large area perovskite films at room temperature.

In conclusion, the facile polymer additive strategy of using low-cost PS to fabricate stable and efficient electro-optical devices ranging from self-powered devices, and stretchable photodetectors to large area solar cells, will serve as a crucial step for bringing the field of perovskite-based advanced optoelectronics one step closer towards commercialization. I believe that this research work will be of widespread interest to the research community and will pave the way for scalable fabrication of stable perovskite thin films and enhancing their application in the fields of solar cells, sensors, and self-powered devices, detectors, and LEDs.

7.2 Future Work

Moving forward, it will be necessary to perform an in-depth analysis of the role of PS in modulating the structural and optoelectronic properties of PS-$MAPbI_3$. To assess the exact mechanism of PbI_2 initiated cross-linking of PS, the H atom present at the α and β carbon atoms of the aliphatic chain of the PS can be substituted by another atomic cluster. The added steric hindrance can be effectively utilized in combination with a change in molecular weight characterized by gel permeation chromatography to understand the PbI_2-catalyzed cross-linking mechanism. Another interesting future direction can be the extension of the PS additive strategy for stabilizing and improving the electro-optical properties of mixed cation lead halide perovskites ($MA_{1-x-y}FA_xCs_yPbI_3$). In addition, computing

the specific interaction energy values of cation-π interaction between MAI and PS can open doors to tailor the properties of organolead halide perovskites in a better manner.

The presence of ferroelectricity in $MAPbI_3$ has been long argued and it will be of significant interest to examine the change in self-powered behavior in $MAPbI_3$-based devices when combined with ferroelectric materials such as ferroelectric nematic liquid crystals and ferroelectric polymers. Extensive research needs to be carried out to understand if the origin of the anomalous photovoltaic behavior and material deterioration mechanism in halide perovskites stems from it.

To minimize the gap between the translation of perovskite-based devices from laboratory to industrial scale, it is crucial for tackling the scalability, reliability (or durability), and environmental sustainability challenges associated with the perovskite-based optoelectronic devices. So far, only the photosensitive perovskite layer of the entire device structure is being coated utilizing large area coating methods such as blade coating. However, the electron and hole transport layers are still being deposited by the traditional spin coating technique limiting the overall feasibility of the device manufacturing. Hence, the room temperature blade coating discussed in Chapter 6 and other scalable processing routes must be explored concurrently to be able to achieve coating of the entire device stack over a large area with efficient materials utilization without incurring cost addition.

Lead is considered a cumulative toxicant that may adversely affect multiple body systems, including the neurologic, hematologic, gastrointestinal, cardiovascular, and renal systems. The neurodevelopmental association observed in infants and children exposed to lead, even at the lowest measurable levels, led leading international governing bodies i.e., the United States Environmental Protection Agency (U.S. EPA) and the World Health Organization (WHO), to state that a threshold for the adverse health effects of lead has not been identified. However, it is to be noted that the amount of lead present in the perovskite solar cells is below that produced annually by the coal industry for generating an equivalent amount of electricity. Nevertheless, to avoid the leaching of PbI_2 in water bodies, several strategies may be employed to minimize the risk to human health. Complete encapsulation of the entire device without adding much to cost and compromising its efficiency can serve as the most feasible solution. Additionally, the Pb ion in the perovskite can be substituted with other nontoxic elements (such as tin) to fabricate lead-free perovskites. The possibility of mitigating challenges associated with the instability of Sn-based perovskite (oxidation from Sn^{2+} to Sn^{4+}) by facile PS additive technique carries huge potential.

Letters of Copyright Permission

CCC RightsLink

Home | Help | Email Support | Avi Mathur

Under the spotlight: The organic–inorganic hybrid halide perovskite for optoelectronic applications

Author:
Qi Chen,Nicholas De Marco,Yang (Michael) Yang,Tze-Bin Song,Chun-Chao Chen,Hongxiang Zhao,Ziruo Hong,Huanping Zhou,Yang Yang

Publication: Nano Today

Publisher: Elsevier

Date: June 2015

Published by Elsevier Ltd.

Creative Commons Attribution-NonCommercial-No Derivatives License (CC BY NC ND)

This article is published under the terms of the Creative Commons Attribution-NonCommercial-No Derivatives License (CC BY NC ND).
For non-commercial purposes you may copy and distribute the article, use portions or extracts from the article in other works, and text or data mine the article, provided you do not alter or modify the article without permission from Elsevier. You may also create adaptations of the article for your own personal use only, but not distribute these to others. You must give appropriate credit to the original work, together with a link to the formal publication through the relevant DOI, and a link to the Creative Commons user license above. If changes are permitted, you must indicate if any changes are made but not in any way that suggests the licensor endorses you or your use of the work.

Permission is not required for this non-commercial use. For commercial use please continue to request permission via RightsLink.

BACK CLOSE WINDOW

CCC | Marketplace™

This is a License Agreement between Avi Mathur ("User") and Copyright Clearance Center, Inc. ("CCC") on behalf of the Rightsholder identified in the order details below. The license consists of the order details, the Marketplace Order General Terms and Conditions below, and any Rightsholder Terms and Conditions which are included below.

All payments must be made in full to CCC in accordance with the Marketplace Order General Terms and Conditions below.

Order Date	15-Aug-2022	Type of Use	Republish in a thesis/dissertation
Order License ID	1257996-1	Publisher	Royal Society of Chemistry
ISSN	2050-7526	Portion	Chapter/article

LICENSED CONTENT

Publication Title	Journal of materials chemistry. C, Materials for optical and electronic devices	Rightsholder	Royal Society of Chemistry
Article Title	Carbon monoxide induced self-doping in methylammonium lead iodide films and associated long-term degradation effects	Publication Type	Journal
		Start Page	7485
		End Page	7493
Author/Editor	Royal Society of Chemistry (Great Britain)	Issue	19
Date	01/01/2012	Volume	10
Language	English		
Country	United Kingdom of Great Britain and Northern Ireland		

REQUEST DETAILS

Portion Type	Chapter/article	Rights Requested	Main product, any product related to main product, and other compilations/derivative products
Page range(s)	All		
Total number of pages	10	Distribution	Worldwide
Format (select all that apply)	Print, Electronic	Translation	Original language of publication
Who will republish the content?	Academic institution	Copies for the disabled?	No
Duration of Use	Life of current edition	Minor editing privileges?	Yes
Lifetime Unit Quantity	More than 2,000,000	Incidental promotional use?	No
		Currency	CAD

NEW WORK DETAILS

Title	Polymer additive engineering of organolead halide perovskites: effect on device characteristics and scalable manufacturing	Institution name	University of Waterloo
		Expected presentation date	2022-10-13
Instructor name	Vivek Maheshwari		

ADDITIONAL DETAILS

Order reference number	N/A	The requesting person / organization to appear on the license	Avi Mathur

REUSE CONTENT DETAILS

Title, description or numeric reference of the portion(s)	Full article	Title of the article/chapter the portion is from	Carbon monoxide induced self-doping in methylammonium lead iodide films and associated long-term degradation effects
Editor of portion(s)	Mathur, Avi; Maheshwari, Vivek	Author of portion(s)	Mathur, Avi; Maheshwari, Vivek
Volume of serial or monograph	10	Issue, if republishing an article from a serial	19
Page or page range of portion	7485-7493	Publication date of portion	2022-01-01

Soft Polymer–Organolead Halide Perovskite Films for Highly Stretchable and Durable Photodetectors with Pt–Au Nanochain-Based Electrodes

Author: Avi Mathur, Hua Fan, Vivek Maheshwari
Publication: Applied Materials
Publisher: American Chemical Society
Date: Dec 1, 2021

References

1. A. Bhalla, R. Guo and R. Roy, *Mater. Res. Innovations*, 2000, **4**, 3-26.
2. K. P. Ong, T. W. Goh, Q. Xu and A. Huan, *J. Phys. Chem. A*, 2015, **119**, 11033-11038.
3. F. Chen, Universita'degli Studi di Cagliari, 2015.
4. J. M. Frost and A. Walsh, in *Organic-Inorganic Halide Perovskite Photovoltaics*, Springer, 2016, pp. 1-17.
5. Q. Chen, N. De Marco, Y. M. Yang, T.-B. Song, C.-C. Chen, H. Zhao, Z. Hong, H. Zhou and Y. Yang, *Nano Today*, 2015, **10**, 355-396.
6. D. Weber, *Zeitschrift für Naturforschung B*, 1978, **33**, 862-865.
7. D. Weber, *Zeitschrift für Naturforschung B*, 1978, **33**, 1443-1445.
8. S. Pang, H. Hu, J. Zhang, S. Lv, Y. Yu, F. Wei, T. Qin, H. Xu, Z. Liu and G. Cui, *Chem. Mater.*, 2014, **26**, 1485-1491.
9. G. E. Eperon, S. D. Stranks, C. Menelaou, M. B. Johnston, L. M. Herz and H. J. Snaith, *Energy Environ. Sci.*, 2014, **7**, 982-988.
10. D. B. Mitzi, *J. Chem. Soc., Dalton Trans.*, 2001, 1-12.
11. G. Kieslich, S. Sun and A. K. Cheetham, *Chemical Science*, 2014, **5**, 4712-4715.
12. C. Bernal and K. Yang, *J. Phys. Chem. C*, 2014, **118**, 24383-24388.
13. F. Hao, C. C. Stoumpos, D. H. Cao, R. P. Chang and M. G. Kanatzidis, *Nat. Photonics*, 2014, **8**, 489.
14. Y. Ogomi, A. Morita, S. Tsukamoto, T. Saitho, N. Fujikawa, Q. Shen, T. Toyoda, K. Yoshino, S. S. Pandey and T. Ma, *J. Phys. Chem. Lett.*, 2014, **5**, 1004-1011.
15. G. Xing, N. Mathews, S. Sun, S. S. Lim, Y. M. Lam, M. Grätzel, S. Mhaisalkar and T. C. Sum, *Science*, 2013, **342**, 344-347.
16. S. D. Stranks, G. E. Eperon, G. Grancini, C. Menelaou, M. J. Alcocer, T. Leijtens, L. M. Herz, A. Petrozza and H. J. Snaith, *Science*, 2013, **342**, 341-344.

17. E. Edri, S. Kirmayer, A. Henning, S. Mukhopadhyay, K. Gartsman, Y. Rosenwaks, G. Hodes and D. Cahen, *Nano Lett.*, 2014, **14**, 1000-1004.

18. C. S. Ponseca Jr, T. J. Savenije, M. Abdellah, K. Zheng, A. Yartsev, T. r. Pascher, T. Harlang, P. Chabera, T. Pullerits and A. Stepanov, *J. Am. Chem. Soc.*, 2014, **136**, 5189-5192.

19. J. H. Noh, S. H. Im, J. H. Heo, T. N. Mandal and S. I. Seok, *Nano Lett.*, 2013, **13**, 1764-1769.

20. G. Niu, W. Li, F. Meng, L. Wang, H. Dong and Y. Qiu, *J. Mater. Chem. A*, 2014, **2**, 705-710.

21. Z. Fan, H. Xiao, Y. Wang, Z. Zhao, Z. Lin, H.-C. Cheng, S.-J. Lee, G. Wang, Z. Feng and W. A. Goddard III, *Joule*, 2017, **1**, 548-562.

22. J. M. Frost, K. T. Butler, F. Brivio, C. H. Hendon, M. Van Schilfgaarde and A. Walsh, *Nano Lett.*, 2014, **14**, 2584-2590.

23. B. Philippe, B.-W. Park, R. Lindblad, J. Oscarsson, S. Ahmadi, E. M. Johansson and H. k. Rensmo, *Chem. Mater.*, 2015, **27**, 1720-1731.

24. G. Abdelmageed, L. Jewell, K. Hellier, L. Seymour, B. Luo, F. Bridges, J. Z. Zhang and S. Carter, *Appl. Phys. Lett.*, 2016, **109**, 233905.

25. C. Eames, J. M. Frost, P. R. Barnes, B. C. O'regan, A. Walsh and M. S. Islam, *Nat. Commun.*, 2015, **6**, 7497.

26. Z. Xiao, Y. Yuan, Y. Shao, Q. Wang, Q. Dong, C. Bi, P. Sharma, A. Gruverman and J. Huang, *Nature materials*, 2015, **14**, 193.

27. S. Bae, S. Kim, S.-W. Lee, K. J. Cho, S. Park, S. Lee, Y. Kang, H.-S. Lee and D. Kim, *J. Phys. Chem. Lett.*, 2016, **7**, 3091-3096.

28. T. A. Berhe, W.-N. Su, C.-H. Chen, C.-J. Pan, J.-H. Cheng, H.-M. Chen, M.-C. Tsai, L.-Y. Chen, A. A. Dubale and B.-J. Hwang, *Energy Environ. Sci.*, 2016, **9**, 323-356.

29. N. Ahn, D.-Y. Son, I.-H. Jang, S. M. Kang, M. Choi and N.-G. Park, *Journal of the American Chemical Society*, 2015, **137**, 8696-8699.

30. L. Zhang, X. Liu, J. Li and S. McKechnie, *Sol. Energy Mater. Sol. Cells*, 2018, **175**, 1-19.

31. Y. Wu, F. Xie, H. Chen, X. Yang, H. Su, M. Cai, Z. Zhou, T. Noda and L. Han, *Advanced materials*, 2017, **29**, 1701073.

32. T. Li, Y. Pan, Z. Wang, Y. Xia, Y. Chen and W. Huang, *J. Mater. Chem. A*, 2017, **5**, 12602-12652.

33. X. Li, W. Zhang, Y.-C. Wang, W. Zhang, H.-Q. Wang and J. Fang, *Nat. Commun.*, 2018, **9**, 3806.

34. L. Zuo, H. Guo, S. Jariwala, N. De Marco, S. Dong, R. DeBlock, D. S. Ginger, B. Dunn, M. Wang and Y. Yang, *Sci. Adv.*, 2017, **3**, e1700106.

35. Y. Zhao, J. Wei, H. Li, Y. Yan, W. Zhou, D. Yu and Q. Zhao, *Nat. Commun.*, 2016, **7**, 10228.

36. N. Gaylord, D. Hoffenberg, B. Matyska and K. Mach, *Journal of Polymer Science Part A-1: Polymer Chemistry*, 1968, **6**, 269-289.

37. R. Saraf and V. Maheshwari, *ACS Appl. Energy Mater.*, 2019, **2**, 2214-2222.

38. D. A. Dougherty, *Acc. Chem. Res.*, 2012, **46**, 885-893.

39. A. S. Mahadevi and G. N. Sastry, *Chem. Rev.*, 2012, **113**, 2100-2138.

40. P. L. Qin, G. Yang, Z. w. Ren, S. H. Cheung, S. K. So, L. Chen, J. Hao, J. Hou and G. Li, *Adv. Mater.*, 2018, **30**, 1706126.

41. Z. Li, Y. Zhao, X. Wang, Y. Sun, Z. Zhao, Y. Li, H. Zhou and Q. Chen, *Joule*, 2018, **2**, 1559-1572.

42. Z. Song, C. L. McElvany, A. B. Phillips, I. Celik, P. W. Krantz, S. C. Watthage, G. K. Liyanage, D. Apul and M. J. Heben, *Energy Environ. Sci.*, 2017, **10**, 1297-1305.

43. S. L. Hamukwaya, H. Hao, Z. Zhao, J. Dong, T. Zhong, J. Xing, L. Hao and M. M. Mashingaidze, *Coatings*, 2022, **12**, 252.

44. M. Yang, D. H. Kim, T. R. Klein, Z. Li, M. O. Reese, B. J. Tremolet de Villers, J. J. Berry, M. F. Van Hest and K. Zhu, *ACS Energy Lett.*, 2018, **3**, 322-328.

45. D. Yang, R. Yang, S. Priya and S. Liu, *Angew. Chem. Int. Ed.*, 2019, **58**, 4466-4483.

46. J. Yu, M. Wang and S. Lin, *ACS Nano*, 2016, **10**, 11044-11057.

47. B. Susrutha, L. Giribabu and S. P. Singh, *Chem. Commun.*, 2015, **51**, 14696-14707.

48. F. Di Giacomo, A. Fakharuddin, R. Jose and T. M. Brown, *Energy Environ. Sci.*, 2016, **9**, 3007-3035.

49. S. Srivastava, A. Behera and R. Biswal, *Micro and Nanosystems*, 2022, **14**, 133-143.

50. T. Ibn-Mohammed, S. Koh, I. Reaney, A. Acquaye, G. Schileo, K. Mustapha and R. Greenough, *Renewable and Sustainable Energy Reviews*, 2017, **80**, 1321-1344.

51. X. Tian, S. D. Stranks and F. You, *Sci. Adv.*, 2020, **6**, eabb0055.

52. H. S. Ullal and B. von Roedern, *Thin film CIGS and CdTe photovoltaic technologies: commercialization, critical issues, and applications*, National Renewable Energy Lab.(NREL), Golden, CO (United States), 2007.

53. F. Azri, A. Meftah, N. Sengouga and A. Meftah, *Solar energy*, 2019, **181**, 372-378.

54. N. K. Tailor, M. Abdi-Jalebi, V. Gupta, H. Hu, M. I. Dar, G. Li and S. Satapathi, *J. Mater. Chem. A*, 2020, **8**, 21356-21386.

55. T. Webb, S. J. Sweeney and W. Zhang, *Adv. Funct. Mater.*, 2021, **31**, 2103121.

56. A. Rajagopal, K. Yao and A. K. Y. Jen, *Adv. Mater.*, 2018, **30**, 1800455.

57. W. Chi and S. K. Banerjee, *Chem. Mater.*, 2021, **33**, 1540-1570.

58. Z. Saki, M. M. Byranvand, N. Taghavinia, M. Kedia and M. Saliba, *Energy Environ. Sci.*, 2021, **14**, 5690-5722.

59. Q. Fang, Y. Shen, S. Zhang, X. Yang, L. Duan, L. Chen, S. Xu, M. Gao and H. Pan, *J. Colloid Interface Sci.*, 2021, **594**, 47-53.

60. F. A. de Souza, G. Sivaraman, J. Hertkorn, R. G. Amorim, M. Fyta and W. L. Scopel, *J. Mater. Chem. A*, 2019, **7**, 8905-8911.

61. X. Chong, Y. Zhang, E. Li, K.-J. Kim, P. R. Ohodnicki, C.-h. Chang and A. X. Wang, *ACS sensors*, 2018, **3**, 230-238.

62. M. Rajapakse, G. Anderson, C. Zhang, R. Musa, J. Walter, M. Yu, G. Sumanasekera and J. B. Jasinski, *PCCP*, 2020, **22**, 5949-5958.

63. M. Wang, Z. Zang, B. Yang, X. Hu, K. Sun and L. Sun, *Sol. Energy Mater. Sol. Cells*, 2018, **185**, 117-123.

64. M. Wang, H. Wang, W. Li, X. Hu, K. Sun and Z. Zang, *J. Mater. Chem. A*, 2019, **7**, 26421-26428.

65. C. Zhang, H. Wang, H. Li, Q. Zhuang, C. Gong, X. Hu, W. Cai, S. Zhao, J. Chen and Z. Zang, *J. Energy Chem.*, 2021, **63**, 452-460.

66. X. Hu, H. Wang, M. Wang and Z. Zang, *Solar Energy*, 2020, **206**, 816-825.

67. H. Wang and D. H. Kim, *Chem. Soc. Rev.*, 2017, **46**, 5204-5236.

68. C. Xie, C. K. Liu, H. L. Loi and F. Yan, *Adv. Funct. Mater.*, 2020, **30**, 1903907.

69. X.-K. Liu, W. Xu, S. Bai, Y. Jin, J. Wang, R. H. Friend and F. Gao, *Nature Materials*, 2021, **20**, 10-21.

70. M.-H. Park, J. S. Kim, J.-M. Heo, S. Ahn, S.-H. Jeong and T.-W. Lee, *ACS Energy Lett.*, 2019, **4**, 1134-1149.

71. C. P. Veeramalai, S. Feng, X. Zhang, S. Pammi, V. Pecunia and C. Li, *Photonics Res.*, 2021, **9**, 968-991.

72. G. Wu, X. Dong, J. Xiu, Y. Yu, M. Gu, T. B. Tang, Z. Zuo, Y. Liu and G. Cui, *PCCP*, 2021, **23**, 17242-17247.

73. Y. Han, S. Meyer, Y. Dkhissi, K. Weber, J. M. Pringle, U. Bach, L. Spiccia and Y.-B. Cheng, *J. Mater. Chem. A*, 2015, **3**, 8139-8147.

74. A. Mathur, H. Fan and V. Maheshwari, *ACS Appl. Mater. Interfaces*, 2021, **13**, 58956-58965.

75. R. Saraf, A. Mathur and V. Maheshwari, *ACS Appl. Mater. Interfaces*, 2020, **12**, 25011-25019.

76. O. R. Yamilova, A. V. Danilov, M. Mangrulkar, Y. S. Fedotov, S. Y. Luchkin, S. D. Babenko, S. I. Bredikhin, S. M. Aldoshin, K. J. Stevenson and P. A. Troshin, *J. Phys. Chem. Lett.*, 2019, **11**, 221-228.

77. L. Zhang and P. H.-L. Sit, *J. Mater. Chem. A*, 2017, **5**, 23976-23986.

78. T. Y. Yang, G. Gregori, N. Pellet, M. Grätzel and J. Maier, *Angew. Chem. Int. Ed.*, 2015, **54**, 7905-7910.

79. A. Nur'aini and I. Oh, *RSC Adv.*, 2020, **10**, 12982-12987.

80. G. Li, Y. Zhang, J. Lin, X. Xu, S. Liu, J. Fang, C. Jing and J. Chu, *J. Phys. Chem. Lett.*, 2021, **12**, 11339-11345.

81. K.-Y. Lee, J.-C. Hsieh, C.-A. Chen, W.-L. Chen, H.-F. Meng, C.-J. Lu, S.-F. Horng and H.-W. Zan, *Sensors Actuators B: Chem.*, 2021, **326**, 128988.

82. X. Fu, S. Jiao, N. Dong, G. Lian, T. Zhao, S. Lv, Q. Wang and D. Cui, *RSC Adv.*, 2018, **8**, 390-395.

83. F. Huang, M. Li, P. Siffalovic, G. Cao and J. Tian, *Energy Environ. Sci.*, 2019, **12**, 518-549.

84. A. Mathur, H. Fan and V. Maheshwari, *Mater. Adv.*, 2021, **2**, 5274-5299.

85. S. Ippili, V. Jella, A. M. Thomas and S.-G. Yoon, *Nanoenergy Advances*, 2021, **1**, 3-31.

86. S. Wang, Y. Jiang, E. J. Juarez-Perez, L. K. Ono and Y. Qi, *Nat. Energy*, 2016, **2**, 1-8.

87. A. Senocrate, T. Acartürk, G. Y. Kim, R. Merkle, U. Starke, M. Grätzel and J. Maier, *J. Mater. Chem. A*, 2018, **6**, 10847-10855.

88. N. Aristidou, I. Sanchez-Molina, T. Chotchuangchutchaval, M. Brown, L. Martinez, T. Rath and S. A. Haque, *Angew. Chem.*, 2015, **127**, 8326-8330.

89. N. Aristidou, C. Eames, I. Sanchez-Molina, X. Bu, J. Kosco, M. S. Islam and S. A. Haque, *Nat. Commun.*, 2017, **8**, 1-10.

90. X. Tang, M. Brandl, B. May, I. Levchuk, Y. Hou, M. Richter, H. Chen, S. Chen, S. Kahmann and A. Osvet, *J. Mater. Chem. A*, 2016, **4**, 15896-15903.

91. R. Dong, Y. Fang, J. Chae, J. Dai, Z. Xiao, Q. Dong, Y. Yuan, A. Centrone, X. C. Zeng and J. Huang, *Adv. Mater.*, 2015, **27**, 1912-1918.

92. Q. Lv, W. He, Z. Lian, J. Ding, Q. Li and Q. Yan, *CrystEngComm*, 2017, **19**, 901-904.

93. S. Matteucci, Y. Yampolskii, B. D. Freeman and I. Pinnau, in *Materials Science of Membranes for Gas and Vapor Separation*, 2006, pp. 1-47.

94. K. Ho, M. Wei, E. H. Sargent and G. C. Walker, *ACS Energy Lett.*, 2021, **6**, 934-940.

95. Y. Li, Z. Zhao, F. Lin, X. Cao, X. Cui and J. Wei, *Small*, 2017, **13**, 1604125.

96. A. Alberti, C. Bongiorno, E. Smecca, I. Deretzis, A. La Magna and C. Spinella, *Nat. Commun.*, 2019, **10**, 1-11.

97. J. Euvrard, O. Gunawan and D. B. Mitzi, *Adv. Energy Mater.*, 2019, **9**, 1902706.

98. S. P. Harvey, Z. Li, J. A. Christians, K. Zhu, J. M. Luther and J. J. Berry, *ACS Appl. Mater. Interfaces*, 2018, **10**, 28541-28552.

99. R. Saraf, T. Tsui and V. Maheshwari, *J. Mater. Chem. A*, 2019, **7**, 14192-14198.

100. M. Spina, A. Karimi, W. Andreoni, C. A. Pignedoli, B. Náfrádi, L. Forró and E. Horváth, *Appl. Phys. Lett.*, 2017, **110**, 121903.

101. W. Veiga, Lepienski and CM, *Materials Science and Engineering: A*, 2002, **335**, 6-13.

102. W.-C. Liao, B. H. Liu and C.-C. Leu, *Appl. Surf. Sci.*, 2020, **507**, 145078.

103. B. N. Reddy, P. N. Kumar and M. Deepa, *Chemphyschem*, 2015, **16**, 377-389.

104. D. Shin, F. Zu, A. V. Cohen, Y. Yi, L. Kronik and N. Koch, *Adv. Mater.*, 2021, **33**, 2100211.

105. J. Yang, Z. Yuan, X. Liu, S. Braun, Y. Li, J. Tang, F. Gao, C. Duan, M. Fahlman and Q. Bao, *ACS Appl. Mater. Interfaces*, 2018, **10**, 16225-16230.

106. C. Li, J. Wei, M. Sato, H. Koike, Z.-Z. Xie, Y.-Q. Li, K. Kanai, S. Kera, N. Ueno and J.-X. Tang, *ACS Appl. Mater. Interfaces*, 2016, **8**, 11526-11531.

107. L. A. Frolova, N. N. Dremova and P. A. Troshin, *Chem. Commun.*, 2015, **51**, 14917-14920.

108. Q. Wang, Y. Shao, H. Xie, L. Lyu, X. Liu, Y. Gao and J. Huang, *Appl. Phys. Lett.*, 2014, **105**, 163508.

109. O. S. Game, G. J. Buchsbaum, Y. Zhou, N. P. Padture and A. I. Kingon, *Adv. Funct. Mater.*, 2017, **27**, 1606584.

110. S. E. O'Kane, G. Richardson, A. Pockett, R. G. Niemann, J. M. Cave, N. Sakai, G. E. Eperon, H. J. Snaith, J. M. Foster and P. J. Cameron, *J. Mater. Chem. C*, 2017, **5**, 452-462.

111. W. Zhu, S. Wang, X. Zhang, A. Wang, C. Wu and F. Hao, *Small*, **n/a**, 2105783.

112. W. Ke, C. Xiao, C. Wang, B. Saparov, H. S. Duan, D. Zhao, Z. Xiao, P. Schulz, S. P. Harvey and W. Liao, *Adv. Mater.*, 2016, **28**, 5214-5221.

113. M. N. F. Hoque, R. He, J. Warzywoda and Z. Fan, *ACS Appl. Mater. Interfaces*, 2018, **10**, 30322-30329.

114. D. Bryant, N. Aristidou, S. Pont, I. Sanchez-Molina, T. Chotchunangatchaval, S. Wheeler, J. R. Durrant and S. A. Haque, *Energy Environ. Sci.*, 2016, **9**, 1655-1660.

115. R. Ahuja, H. Arwin, A. Ferreira da Silva, C. Persson, J. M. Osorio-Guillén, J. Souza de Almeida, C. Moyses Araujo, E. Veje, N. Veissid and C. An, *J. Appl. Phys.*, 2002, **92**, 7219-7224.

116. R. Saraf, L. Pu and V. Maheshwari, *Adv. Mater.*, 2018, **30**, 1705778.

117. Y. Yuan, T. Li, Q. Wang, J. Xing, A. Gruverman and J. Huang, *Sci. Adv.*, 2017, **3**, e1602164.

118. R. Saraf and V. Maheshwari, *ACS Appl. Mater. Interfaces*, 2018, **10**, 21066-21072.

119. A. Mathur, A. Li and V. Maheshwari, *J. Phys. Chem. Lett.*, 2021, **12**, 1481-1489.

120. J. Muenter, *J. Mol. Spectrosc.*, 1975, **55**, 490-491.

121. M.-C. Shih, S.-S. Li, C.-H. Hsieh, Y.-C. Wang, H.-D. Yang, Y.-P. Chiu, C.-S. Chang and C.-W. Chen, *Nano Lett.*, 2017, **17**, 1154-1160.

122. Q. Chen, H. Zhou, T.-B. Song, S. Luo, Z. Hong, H.-S. Duan, L. Dou, Y. Liu and Y. Yang, *Nano Lett.*, 2014, **14**, 4158-4163.

123. G. Paul, S. Chatterjee, H. Bhunia and A. J. Pal, *J. Phys. Chem. C*, 2018, **122**, 20194-20199.

124. M. Jiang, Y. Wu, Y. Zhou and Z. Wang, *AIP Advances*, 2019, **9**, 085301.

125. J. Chang, H. Zhu, J. Xiao, F. H. Isikgor, Z. Lin, Y. Hao, K. Zeng, Q.-H. Xu and J. Ouyang, *J. Mater. Chem. A*, 2016, **4**, 7943-7949.

126. H. Wang, Z. Wang, Z. Yang, Y. Xu, Y. Ding, L. Tan, C. Yi, Z. Zhang, K. Meng and G. Chen, *Adv. Mater.*, 2020, **32**, 2000865.

127. T. P. Gujar, T. Unger, A. Schönleber, M. Fried, F. Panzer, S. van Smaalen, A. Köhler and M. Thelakkat, *PCCP*, 2018, **20**, 605-614.

128. B. Roose, K. Dey, Y.-H. Chiang, R. H. Friend and S. D. Stranks, *J. Phys. Chem. Lett.*, 2020, **11**, 6505-6512.

129. H. Y. Wang, M. Y. Hao, J. Han, M. Yu, Y. Qin, P. Zhang, Z. X. Guo, X. C. Ai and J. P. Zhang, *Chemistry–A European Journal*, 2017, **23**, 3986-3992.

130. G.-H. Kim and D. S. Kim, *Joule*, 2021, **5**, 1033-1035.

131. S. Kundu and T. L. Kelly, *EcoMat*, 2020, **2**, e12025.

132. K. Kim, J. Han, S. Maruyama, M. Balaban and I. Jeon, *Sol. RRL*, 2021, **5**, 2000783.

133. J.-S. Park, J. Calbo, Y.-K. Jung, L. D. Whalley and A. Walsh, *ACS Energy Lett.*, 2019, **4**, 1321-1327.

134. A. F. Castro-Méndez, J. Hidalgo and J. P. Correa-Baena, *Adv. Energy Mater.*, 2019, **9**, 1901489.

135. Y. Ma, Y. Cheng, X. Xu, M. Li, C. Zhang, S. H. Cheung, Z. Zeng, D. Shen, Y. M. Xie and K. L. Chiu, *Adv. Funct. Mater.*, 2021, **31**, 2006802.

136. Y. Xu, G. Liu, J. Hu, G. Wang, M. Chen, Y. Chen, M. Li, H. Zhang and Y. Chen, *J. Phys. Chem. Lett.*, 2022, **13**, 3754-3762.

137. L. Ma, Z. Yan, X. Zhou, Y. Pi, Y. Du, J. Huang, K. Wang, K. Wu, C. Zhuang and X. Han, *Nat. Commun.*, 2021, **12**, 1-10.

138. H. Zhang, J. Shi, L. Zhu, Y. Luo, D. Li, H. Wu and Q. Meng, *Nano Energy*, 2018, **43**, 383-392.

139. M.-C. Wu, Y.-Y. Li, S.-H. Chan, K.-M. Lee and W.-F. Su, *Sol. RRL*, 2020, **4**, 2000093.

140. L. Zheng, K. Wang, T. Zhu, Y. Yang, R. Chen, K. Gu, C. Liu and X. Gong, *ACS Appl. Energy Mater.*, 2020, **3**, 5902-5912.

141. Y. Cai, Z. Zhang, Y. Zhou, H. Liu, Q. Qin, X. Lu, X. Gao, L. Shui, S. Wu and J. Liu, *Electrochim. Acta*, 2018, **261**, 445-453.

142. Q. Dong, Z. Wang, K. Zhang, H. Yu, P. Huang, X. Liu, Y. Zhou, N. Chen and B. Song, *Nanoscale*, 2016, **8**, 5552-5558.

143. Y. Zhang, X. Zhuang, K. Zhou, C. Cai, Z. Hu, J. Zhang and Y. Zhu, *J. Mater. Chem. C*, 2017, **5**, 9037-9043.

144. J. Yan, N. Li, Y. Ai, Z. Wang, W. Yang, M. Zhao, C. Shou, B. Yan, J. Sheng and J. Ye, *Sustainable Energy & Fuels*, 2019, **3**, 3448-3454.

145. J. Yang, Q. Cao, Z. He, X. Pu, T. Li, B. Gao and X. Li, *Nano Energy*, 2021, **82**, 105731.

146. Y. Zhou, Y. Yin, X. Zuo, L. Wang, T.-D. Li, Y. Xue, A. Subramanian, Y. Fang, Y. Guo and Z. Yang, *Chem. Mater.*, 2021, **33**, 6120-6135.

147. Y. Zong, Y. Zhou, Y. Zhang, Z. Li, L. Zhang, M.-G. Ju, M. Chen, S. Pang, X. C. Zeng and N. P. Padture, *Chem*, 2018, **4**, 1404-1415.

148. C. Wang, Z. Song, D. Zhao, R. A. Awni, C. Li, N. Shrestha, C. Chen, X. Yin, D. Li and R. J. Ellingson, *Sol. RRL*, 2019, **3**, 1900078.

149. W. Xiang, Q. Chen, Y. Wang, M. Liu, F. Huang, T. Bu, T. Wang, Y.-B. Cheng, X. Gong and J. Zhong, *J. Mater. Chem. A*, 2017, **5**, 5486-5494.

150. X. Hu, Z. Huang, F. Li, M. Su, Z. Huang, Z. Zhao, Z. Cai, X. Yang, X. Meng and P. Li, *Energy Environ. Sci.*, 2019, **12**, 979-987.

151. G. Liu, C. Liu, Z. Lin, J. Yang, Z. Huang, L. Tan and Y. Chen, *ACS Appl. Mater. Interfaces*, 2020, **12**, 14049-14056.

152. J. C. da Silva, F. L. de Araujo, R. Szostak, P. E. Marchezi, R. F. Moral, J. N. de Freitas and A. F. Nogueira, *J. Mater. Chem. C*, 2020, **8**, 9697-9706.

153. Y. You, W. Tian, M. Wang, F. Cao, H. Sun and L. Li, *Adv. Mater. Interfaces*, 2020, **7**, 2000537.

154. L. Song, X. Guo, Y. Hu, Y. Lv, J. Lin, Z. Liu, Y. Fan and X. Liu, *J. Phys. Chem. Lett.*, 2017, **8**, 4148-4154.

155. M. Kim, S. G. Motti, R. Sorrentino and A. Petrozza, *Energy Environ. Sci.*, 2018, **11**, 2609-2619.

156. A. Mathur and V. Maheshwari, *J. Mater. Chem. C*, 2022, **10**, 7485-7493.

157. J. Wei, F. Guo, X. Wang, K. Xu, M. Lei, Y. Liang, Y. Zhao and D. Xu, *Adv. Mater.*, 2018, **30**, 1805153.

158. Z. Liu, P. Liu, T. He, L. Zhao, X. Zhang, J. Yang, H. Yang, H. Liu, R. Qin and M. Yuan, *ACS Appl. Mater. Interfaces*, 2020, **12**, 26670-26679.

159. M. J. Reddy, J. S. Kumar, U. S. Rao and P. P. Chu, *Solid State Ionics*, 2006, **177**, 253-256.

160. L. Lyu, Y. Gao, Y. Wang, L. Xiao, J. Lu and L. Zhuang, *Chem. Phys. Lett.*, 2019, **723**, 102-110.

161. S. Li, K. Jiang, J. Wang, C. Zuo, Y. H. Jo, D. He, X. Xie and Z. Xue, *Macromolecules*, 2019, **52**, 7234-7243.

162. R. Saraf, L. Pu and V. Maheshwari, *Adv. Mater.*, 2018, **30**, 1705778.

163. Y. Zhao, J. Wei, H. Li, Y. Yan, W. Zhou, D. Yu and Q. Zhao, *Nat. Commun.*, 2016, **7**, 1-9.

164. Y. C. Zhou, Y. F. Yin, X. H. Zuo, L. K. Wang, T. D. Li, Y. Y. Zhou, N. P. Padture, Z. H. Yang, Y. C. Guo, Y. Xue, K. Kisslinger, M. Cotlet, C. Y. Nam and M. H. Rafailovich, *Chem. Mater.*, 2020, **32**, 5104-5117.

165. L. J. Zuo, H. X. Guo, D. W. deQuilettes, S. Jariwala, N. De Marco, S. Q. Dong, R. DeBlock, D. S. Ginger, B. Dunn, M. K. Wang and Y. Yang, *Sci. Adv.*, 2017, **3**, 11.

166. J. M. Yang, S. B. Xiong, T. Y. Qu, Y. X. Zhang, X. X. He, X. W. Guo, Q. H. Zhao, S. Braun, J. Q. Chen, J. H. Xu, Y. Q. Li, X. J. Liu, C. G. Duan, J. X. Tang, M. Fahlman and Q. Bao, *ACS Appl. Mater. Interfaces*, 2019, **11**, 13491-13498.

167. H. Y. Zheng, X. X. Xu, S. D. Xu, G. Z. Liu, S. H. Chen, X. X. Zhang, T. W. Chen and X. Pan, *J. Mater. Chem. C*, 2019, **7**, 4441-4448.

168. D. Wang, L. Zhang, K. M. Deng, W. N. Zhang, J. Song, J. H. Wu and Z. Lan, *Energy Technol.*, 2018, **6**, 2380-2386.

169. H. P. Kim, A. R. bin Mohd Yusoff and J. Jang, *Nanoscale Adv.*, 2019, **1**, 76-85.

170. Y.-Y. Kim, J. D. Carloni, B. Demarchi, D. Sparks, D. G. Reid, M. E. Kunitake, C. C. Tang, M. J. Duer, C. L. Freeman and B. Pokroy, *Nature materials*, 2016, **15**, 903.

171. K. Naka and Y. Chujo, *Chem. Mater.*, 2001, **13**, 3245-3259.

172. G. Falini, S. Albeck, S. Weiner and L. Addadi, *Science*, 1996, **271**, 67-69.

173. R. Tannenbaum, *Langmuir*, 1997, **13**, 5056-5060.

174. N. Hosoda and T. Kato, *Chem. Mater.*, 2001, **13**, 688-693.

175. D. Barbieri, H. P. Yuan, X. M. Luo, S. Fare, D. W. Grijpma and J. D. de Bruijn, *Acta Biomater.*, 2013, **9**, 9401-9413.

176. N. Y. Ning, F. Luo, K. Wang, Q. Zhang, F. Chen, R. N. Du, C. Y. An, B. F. Pan and Q. Fu, *J. Phys. Chem. B*, 2008, **112**, 14140-14148.

177. M. Minelli, M. G. De Angelis, F. Doghieri, M. Marini, M. Toselli and F. Pilati, *Eur. Polym. J.*, 2008, **44**, 2581-2588.

178. A. Saxena, B. P. Tripathi and V. K. Shahi, *J. Phys. Chem. B*, 2007, **111**, 12454-12461.

179. K. Shin, S. Obukhov, J.-T. Chen, J. Huh, Y. Hwang, S. Mok, P. Dobriyal, P. Thiyagarajan and T. P. Russell, *Nat. Mater.*, 2007, **6**, 961-965.

180. J. I. Langford and A. J. C. Wilson, *J. Appl. Crystallogr.*, 1978, **11**, 102-113.

181. R. Saraf, A. Mathur and V. Maheshwari, *ACS Appl. Mater. Interfaces*, 2020, DOI: 10.1021/acsami.0c04346.

182. C. Stavrakas, S. J. Zelewski, K. Frohna, E. P. Booker, K. Galkowski, K. Ji, E. Ruggeri, S. Mackowski, R. Kudrawiec, P. Plochocka and S. D. Stranks, *Adv. Energy Mater.*, 2019, **9**, 1901883.

183. X. D. Li, W. X. Zhang, Y. C. Wang, W. J. Zhang, H. Q. Wang and J. F. Fang, *Nat. Commun.*, 2018, **9**, 10.

184. S. Jariwala, H. Sun, G. W. Adhyaksa, A. Lof, L. A. Muscarella, B. Ehrler, E. C. Garnett and D. S. Ginger, *Joule*, 2019, **3**, 3048-3060.

185. Y. Liu, L. Collins, R. Proksch, S. Kim, B. R. Watson, B. Doughty, T. R. Calhoun, M. Ahmadi, A. V. Ievlev and S. Jesse, *Nat. Mater.*, 2018, **17**, 1013-1019.

186. Y. Zhou, O. S. Game, S. Pang and N. P. Padture, *J. Phys. Chem. Lett.*, 2015, **6**, 4827-4839.

187. Y. Liu, M. Lorenz, A. V. Ievlev and O. S. Ovchinnikova, *Adv. Funct. Mater.*, 2020, **30**, 2002201.

188. M. Ralaiarisoa, Y. Busby, J. Frisch, I. Salzmann, J.-J. Pireaux and N. Koch, *PCCP*, 2017, **19**, 828-836.

189. D. Wei, F. Ma, R. Wang, S. Dou, P. Cui, H. Huang, J. Ji, E. Jia, X. Jia and S. Sajid, *Adv. Mater.*, 2018, **30**, 1707583.

190. L. Weng, P. Bertrand, J. Stone-Masui and W. Stone, *Surf. Interface Anal.*, 1994, **21**, 387-394.

191. F. Petrat, D. Wolany, B. Schwede, L. Wiedmann and A. Benninghoven, *Surf. Interface Anal.*, 1994, **21**, 274-282.

192. S. Higashi, T. Yamamuro, T. Nakamura, Y. Ikada, S.-H. Hyon and K. Jamshidi, *Biomaterials*, 1986, **7**, 183-187.

193. J. Barbé, V. Kumar, M. J. Newman, H. K. Lee, S. M. Jain, H. Chen, C. Charbonneau, C. Rodenburg and W. C. Tsoi, *Sustainable Energy & Fuels*, 2018, **2**, 905-914.

194. Y. Yuan, J. Chae, Y. Shao, Q. Wang, Z. Xiao, A. Centrone and J. Huang, *Adv. Energy Mater.*, 2015, **5**, 1500615.

195. L. M. Garten, D. T. Moore, S. U. Nanayakkara, S. Dwaraknath, P. Schulz, J. Wands, A. Rockett, B. Newell, K. A. Persson and S. Trolier-McKinstry, *Sci. Adv.*, 2019, **5**, eaas9311.

196. Y. Kutes, L. Ye, Y. Zhou, S. Pang, B. D. Huey and N. P. Padture, *J. Phys. Chem. Lett.*, 2014, **5**, 3335-3339.

197. Y. Rakita, O. Bar-Elli, E. Meirzadeh, H. Kaslasi, Y. Peleg, G. Hodes, I. Lubomirsky, D. Oron, D. Ehre and D. Cahen, *PNAS*, 2017, **114**, E5504-E5512.

198. D. T. Gentekos, R. J. Sifri and B. P. Fors, *Nature Reviews Materials*, 2019, 1-14.

199. N. Davidson, L. Fetters, W. Funk, N. Hadjichristidis and W. Graessley, *Macromolecules*, 1987, **20**, 2614-2619.

200. Y. H. Ma, Y. H. Cheng, X. W. Xu, M. L. Li, C. J. Zhang, S. H. Cheung, Z. X. Zeng, D. Shen, Y. M. Xie, K. L. Chiu, F. Lin, S. K. So, C. S. Lee and S. W. Tsang, *Adv. Funct. Mater.*, 2020, DOI: 10.1002/adfm.202006802, 9.

201. T. S. Sherkar, C. Momblona, L. n. Gil-Escrig, J. Ávila, M. Sessolo, H. J. Bolink and L. J. A. Koster, *ACS Energy Lett.*, 2017, **2**, 1214-1222.

202. T. Niu, J. Lu, R. Munir, J. Li, D. Barrit, X. Zhang, H. Hu, Z. Yang, A. Amassian and K. Zhao, *Adv. Mater.*, 2018, **30**, 1706576.

203. Q. Wang, B. Chen, Y. Liu, Y. Deng, Y. Bai, Q. Dong and J. Huang, *Energy Environ. Sci.*, 2017, **10**, 516-522.

204. A. Fakharuddin, M. Seybold, A. Agresti, S. Pescetelli, F. Matteocci, M. I. Haider, S. T. Birkhold, H. Hu, R. Giridharagopal and M. Sultan, *ACS Appl. Mater. Interfaces*, 2018, **10**, 42542-42551.

205. M. Li, X. Yan, Z. Kang, Y. Huan, Y. Li, R. Zhang and Y. Zhang, *ACS Appl. Mater. Interfaces*, 2018, **10**, 18787-18795.

206. F. Tan, H. Tan, M. I. Saidaminov, M. Wei, M. Liu, A. Mei, P. Li, B. Zhang, C. S. Tan and X. Gong, *Adv. Mater.*, 2019, **31**, 1807435.

207. J. Dong, D. Song, J. Meng, Y. Lu, Y. Li, B. Qiao, S. Zhao and Z. Xu, *J. Mater. Chem. C*, 2020, **8**, 6743-6748.

208. Q. Zhang, S. Xiong, J. Ali, K. Qian, Y. Li, W. Feng, H. Hu, J. Song and F. Liu, *J. Mater. Chem. C*, 2020, **8**, 5467-5475.

209. Q. Wang, Q. Dong, T. Li, A. Gruverman and J. Huang, *Adv. Mater.*, 2016, **28**, 6734-6739.

210. Z. Dai, S. K. Yadavalli, M. Hu, M. Chen, Y. Zhou and N. P. Padture, *Scr. Mater.*, 2020, **185**, 47-50.

211. L.-J. Ji, S.-J. Sun, Y. Qin, K. Li and W. Li, *Coord. Chem. Rev.*, 2019, **391**, 15-29.

212. Z. Wu, P. Li, Y. Zhang and Z. Zheng, *Small Methods*, 2018, **2**, 1800031.

213. J. He, R. G. Nuzzo and J. A. Rogers, *Proc. IEEE*, 2015, **103**, 619-632.

214. W. Jang, B. G. Kim, S. Seo, A. Shawky, M. S. Kim, K. Kim, B. Mikladal, E. I. Kauppinen, S. Maruyama and I. Jeon, *Nano Today*, 2021, **37**, 101081.

215. J. Zhao, Z. Chi, Z. Yang, X. Chen, M. S. Arnold, Y. Zhang, J. Xu, Z. Chi and M. P. Aldred, *Nanoscale*, 2018, **10**, 5764-5792.

216. J. H. Koo, D. C. Kim, H. J. Shim, T. H. Kim and D. H. Kim, *Adv. Funct. Mater.*, 2018, **28**, 1801834.

217. Y. Zhao, C. Li, J. Jiang, B. Wang and L. Shen, *Small*, 2020, **16**, 2001534.

218. N. Ma, J. Jiang, Y. Zhao, L. He, Y. Ma, H. Wang, L. Zhang, C. Shan, L. Shen and W. Hu, *Nano Energy*, 2021, **86**, 106113.

219. C. Li, H. Wang, F. Wang, T. Li, M. Xu, H. Wang, Z. Wang, X. Zhan, W. Hu and L. Shen, *Light: Science & Applications*, 2020, **9**, 1-8.

220. L. He, D. Wang, Y. Zhao, Y. Zhang, W. Wei and L. Shen, *J. Mater. Chem. C*, 2021.

221. K.-G. Lim, T.-H. Han and T.-W. Lee, *Energy Environ. Sci.*, 2021, **14**, 2009-2035.

222. Y. Wang, X. Li, Y. Hou, C. Yin and Z. Yin, *Frontiers of Materials Science*, 2021, 1-25.

223. L. Jiang, J. Lu, S. R. Raga, J. Sun, X. Lin, W. Huang, F. Huang, U. Bach and Y.-B. Cheng, *Nano Energy*, 2019, **58**, 687-694.

224. F. Huang, L. Jiang, A. R. Pascoe, Y. Yan, U. Bach, L. Spiccia and Y.-B. Cheng, *Nano Energy*, 2016, **27**, 509-514.

225. W. Deng, F. Li, J. Li, M. Wang, Y. Hu and M. Liu, *Nano Energy*, 2020, **70**, 104505.

226. H. S. Jung, G. S. Han, N.-G. Park and M. J. Ko, *Joule*, 2019, **3**, 1850-1880.

227. P. Jia, M. Lu, S. Sun, Y. Gao, R. Wang, X. Zhao, G. Sun, V. L. Colvin and W. W. Yu, *Adv. Mater. Interfaces*, 2021, **8**, 2100441.

228. J.-H. Kim, H.-J. Seok, H.-J. Seo, T.-Y. Seong, J. H. Heo, S.-H. Lim, K.-J. Ahn and H.-K. Kim, *Nanoscale*, 2018, **10**, 20587-20598.

229. X. Meng, Z. Cai, Y. Zhang, X. Hu, Z. Xing, Z. Huang, Z. Huang, Y. Cui, T. Hu and M. Su, *Nat. Commun.*, 2020, **11**, 1-10.

230. G. Lee, M.-c. Kim, Y. W. Choi, N. Ahn, J. Jang, J. Yoon, S. M. Kim, J.-G. Lee, D. Kang and H. S. Jung, *Energy Environ. Sci.*, 2019, **12**, 3182-3191.

231. Z. Wang, L. Zeng, C. Zhang, Y. Lu, S. Qiu, C. Wang, C. Liu, L. Pan, S. Wu and J. Hu, *Adv. Funct. Mater.*, 2020, **30**, 2001240.

232. J. Han, J.-S. Nam, K. Kim, E. J. Choi, J.-M. Lee, S. Maruyama, I. Jeon and J.-W. Oh, *Mater. Adv.*, 2021, **2**, 488-496.

233. X. Meng, Z. Xing, X. Hu, Z. Huang, T. Hu, L. Tan, F. Li and Y. Chen, *Angew. Chem. Int. Ed.*, 2020, **59**, 16602-16608.

234. P. Ma, Y. Lou, S. Cong, Z. Lu, K. Zhu, J. Zhao and G. Zou, *Adv. Energy Mater.*, 2020, **10**, 1903357.

235. J. Qi, H. Xiong, C. Hou, Q. Zhang, Y. Li and H. Wang, *Nanoscale*, 2020, **12**, 3646-3656.

236. W. Wang, G. Li, Z. Jiang, Y. Zhang, T. Hu, J. Yi and Z. Chu, *Opt. Mater.*, 2021, **114**, 110926.

237. H. Li, W. Wang, Y. Yang, Y. Wang, P. Li, J. Huang, J. Li, Y. Lu, Z. Li and Z. Wang, *ACS Nano*, 2020, **14**, 1560-1568.

238. Y.-H. Chen, M. Kataria, H.-I. Lin, C. R. Paul Inbaraj, Y.-M. Liao, H.-W. Hu, T.-J. Chang, C.-H. Lu, W.-H. Shih and W.-H. Wang, *ACS Appl. Electron. Mater.*, 2019, **1**, 1517-1526.

239. J. Ding, H. Fang, Z. Lian, Q. Lv, J.-L. Sun and Q. Yan, *Nanoscale*, 2018, **10**, 10538-10544.

240. L. Pu, H. Fan and V. Maheshwari, *Catal. Sci. Technol.*, 2020, **10**, 2020-2028.

241. C. Mayousse, C. Celle, A. Fraczkiewicz and J.-P. Simonato, *Nanoscale*, 2015, **7**, 2107-2115.

242. N. Grillet, D. Manchon, E. Cottancin, F. Bertorelle, C. Bonnet, M. Broyer, J. Lermé and M. Pellarin, *J. Phys. Chem. C*, 2013, **117**, 2274-2282.

243. Y. Shi, L. He, Q. Deng, Q. Liu, L. Li, W. Wang, Z. Xin and R. Liu, *Micromachines*, 2019, **10**, 330.

244. J. Li, J. Mayer and E. Colgan, *J. Appl. Phys.*, 1991, **70**, 2820-2827.

245. H. Fan and V. Maheshwari, *Adv. Mater. Technol.*, 2020, **5**, 2000090.

246. D. Wang, Y. Zhang, X. Lu, Z. Ma, C. Xie and Z. Zheng, *Chem. Soc. Rev.*, 2018, **47**, 4611-4641.

247. B. V. Derjaguin, V. M. Muller and Y. P. Toporov, *J. Colloid Interface Sci.*, 1975, **53**, 314-326.

248. H. Jiang, D.-Y. Khang, J. Song, Y. Sun, Y. Huang and J. A. Rogers, *Proc. Natl. Acad. Sci.*, 2007, **104**, 15607-15612.

249. D. Y. Khang, J. A. Rogers and H. H. Lee, *Adv. Funct. Mater.*, 2009, **19**, 1526-1536.

250. R. Saraf, H. Fan and V. Maheshwari, *npj Flexible Electron.*, 2020, **4**, 1-8.

251. H. W. Hu, G. Haider, Y. M. Liao, P. K. Roy, R. Ravindranath, H. T. Chang, C. H. Lu, C. Y. Tseng, T. Y. Lin and W. H. Shih, *Adv. Mater.*, 2017, **29**, 1703549.

252. L. Dou, Y. M. Yang, J. You, Z. Hong, W.-H. Chang, G. Li and Y. Yang, *Nat. Commun.*, 2014, **5**, 1-6.

253. Y. Liu, I. Sokolov, M. E. Dokukin and Y. Xiong, *Nanoscale*, 2020, **12**, 12432-12443.

254. D. J. Fairfield, H. Sai, A. Narayanan, J. V. Passarelli, M. Chen, J. Palasz, L. C. Palmer, M. R. Wasielewski and S. I. Stupp, *J. Mater. Chem. A*, 2019, **7**, 1687-1699.

255. W.-C. Liao, B. H. Liu and C.-C. Leu, *Appl. Surf. Sci.*, 2021, **545**, 149081.

256. Y. Rakita, S. R. Cohen, N. K. Kedem, G. Hodes and D. Cahen, *MRS Commun.*, 2015, **5**, 623-629.

257. E. M. Hutter, L. A. Muscarella, F. Wittmann, J. Versluis, L. McGovern, H. J. Bakker, Y.-W. Woo, Y.-K. Jung, A. Walsh and B. Ehrler, *Cell Rep. Phys. Sci.*, 2020, **1**, 100120.

258. I. Mela, C. Poudel, M. Anaya, G. Delport, K. Frohna, S. Macpherson, T. A. Doherty, A. Scheeder, S. D. Stranks and C. F. Kaminski, *Adv. Funct. Mater.*, 2021, 2100293.

259. N. Rolston, A. D. Printz, J. M. Tracy, H. C. Weerasinghe, D. Vak, L. J. Haur, A. Priyadarshi, N. Mathews, D. J. Slotcavage and M. D. McGehee, *Adv. Energy Mater.*, 2018, **8**, 1702116.

260. N. Rolston, B. L. Watson, C. D. Bailie, M. D. McGehee, J. P. Bastos, R. Gehlhaar, J.-E. Kim, D. Vak, A. T. Mallajosyula and G. Gupta, *Extreme Mech. Lett.*, 2016, **9**, 353-358.

261. A. Serrano, G. Welsch and R. Gibala, *Polym. Eng. Sci.*, 1982, **22**, 946-949.

262. E. Plati and J. Williams, *Polym. Eng. Sci.*, 1975, **15**, 470-477.

263. X. Hu, Y. Dou, J. Li and Z. Liu, *Small*, 2019, **15**, 1804805.

264. C. Case, N. Beaumont and D. Kirk, *ACS Energy Lett.*, 2019, **4**, 2760-2762.

265. F. Wang, Y. Cao, C. Chen, Q. Chen, X. Wu, X. Li, T. Qin and W. Huang, *Adv. Funct. Mater.*, 2018, **28**, 1803753.

266. L. Qiu, L. K. Ono and Y. Qi, *Mater. Today Energy*, 2018, **7**, 169-189.

267. A. Extance, *Nature*, 2019, **570**, 429-433.

268. L. Qiu, S. He, L. K. Ono, S. Liu and Y. Qi, *ACS Energy Lett.*, 2019, **4**, 2147-2167.

269. Y. Yang and J. You, *Nature*, 2017, **544**, 155-156.

270. Y. Xiao, C. Zuo, J. X. Zhong, W. Q. Wu, L. Shen and L. Ding, *Adv. Energy Mater.*, 2021, **11**, 2100378.

271. N.-G. Park and K. Zhu, *Nat. Rev. Mater.*, 2020, **5**, 333-350.

272. Y. S. Jung, K. Hwang, Y. J. Heo, J. E. Kim, D. Vak and D. Y. Kim, *Adv. Opt. Mater.*, 2018, **6**, 1701182.

273. J. X. Zhong, W. Q. Wu, L. Ding and D. B. Kuang, *Energy & Environmental Materials*, 2021, **4**, 277-283.

274. J. Cheng, F. Liu, Z. Tang and Y. Li, *Energy Technology*, 2021, **9**, 2100204.

275. J. Jiang, Q. Wang, Z. Jin, X. Zhang, J. Lei, H. Bin, Z. G. Zhang, Y. Li and S. Liu, *Adv. Energy Mater.*, 2018, **8**, 1701757.

276. Y. Deng, Q. Dong, C. Bi, Y. Yuan and J. Huang, *Adv. Energy Mater.*, 2016, **6**, 1600372.

277. S. Tang, Y. Deng, X. Zheng, Y. Bai, Y. Fang, Q. Dong, H. Wei and J. Huang, *Adv. Energy Mater.*, 2017, **7**, 1700302.

278. W. Q. Wu, P. N. Rudd, Q. Wang, Z. Yang and J. Huang, *Adv. Mater.*, 2020, **32**, 2000995.

279. W.-Q. Wu, P. N. Rudd, Z. Ni, C. H. Van Brackle, H. Wei, Q. Wang, B. R. Ecker, Y. Gao and J. Huang, *J. Am. Chem. Soc.*, 2020, **142**, 3989-3996.

280. X. Zheng, Y. Deng, B. Chen, H. Wei, X. Xiao, Y. Fang, Y. Lin, Z. Yu, Y. Liu and Q. Wang, *Adv. Mater.*, 2018, **30**, 1803428.

281. M. He, B. Li, X. Cui, B. Jiang, Y. He, Y. Chen, D. O'Neil, P. Szymanski, M. A. Ei-Sayed and J. Huang, *Nat. Commun.*, 2017, **8**, 1-10.

282. B. Chen, J. Y. Zhengshan, S. Manzoor, S. Wang, W. Weigand, Z. Yu, G. Yang, Z. Ni, X. Dai and Z. C. Holman, *Joule*, 2020, **4**, 850-864.

283. M. Yang, Z. Li, M. O. Reese, O. G. Reid, D. H. Kim, S. Siol, T. R. Klein, Y. Yan, J. J. Berry and M. F. Van Hest, *Nat. Energy*, 2017, **2**, 1-9.

284. J. Ding, Q. Han, Q.-Q. Ge, D.-J. Xue, J.-Y. Ma, B.-Y. Zhao, Y.-X. Chen, J. Liu, D. B. Mitzi and J.-S. Hu, *Joule*, 2019, **3**, 402-416.

285. Z. Ouyang, M. Yang, J. B. Whitaker, D. Li and M. F. van Hest, *ACS Appl. Energy Mater.*, 2020, **3**, 3714-3720.

286. Y. Deng, C. H. Van Brackle, X. Dai, J. Zhao, B. Chen and J. Huang, *Sci. Adv.*, 2019, **5**, eaax7537.

287. S. Rentenberger, A. Vollmer, E. Zojer, R. Schennach and N. Koch, *J. Appl. Phys.*, 2006, **100**, 053701.

288. W. N. Hansen and K. B. Johnson, *Surf. Sci.*, 1994, **316**, 373-382.

289. A. Salker, N.-J. Choi, J.-H. Kwak, B.-S. Joo and D.-D. Lee, *Sensors Actuators B: Chem.*, 2005, **106**, 461-467.

290. H.-J. Lin, J. P. Baltrus, H. Gao, Y. Ding, C.-Y. Nam, P. Ohodnicki and P.-X. Gao, *ACS Appl. Mater. Interfaces*, 2016, **8**, 8880-8887.

291. S. B. Karki, R. K. Hona and F. Ramezanipour, *J. Electron. Mater.*, 2020, **49**, 1557-1567.

292. M. Nayakasinghe, Y. Han, N. Sivapragasam, D. S. Kilin and U. Burghaus, *Chem. Commun.*, 2018, **54**, 9949-9952.

293. D. Tevault and K. Nakamoto, *Inorg. Chem.*, 1976, **15**, 1282-1287.

294. S. Karthika, T. Radhakrishnan and P. Kalaichelvi, *Cryst. Growth Des.*, 2016, **16**, 6663-6681.

295. R. H. Fowler and L. Nordheim, *Proc. R. Soc. Lond. A*, 1928, **119**, 173-181.

Appendices

Appendix for Chapter 2

Interpretation of work function from AM-KPFM

The KPFM measures the contact potential difference (V_{CPD}) between the conductive tip and the sample:

$$V_{CPD} = \frac{(\Phi_{tip} - \Phi_{sample})}{e}$$

Where ϕ_{tip} and ϕ_{sample} represent the work function of the conductive tip and sample, respectively, and can be approximated as their respective Fermi level positions. A freshly cleaved highly oriented pyrolytic graphite (HOPG) with a stable work function (4.65 eV) was used as a reference sample to calibrate the work function of the KPFM probe. The absolute surface work function of the sample was then calculated by the following equation:

$$\Phi_{sample} = 4.65\ eV + V_{CPD(HOPG)} - V_{CPD(sample)}$$

Further, to confirm the reliability of the technique in accurately determining the work function, a V_{CPD} map of a gold electrode patterned over a Si/SiO_2 wafer was acquired, as seen in Fig. S4. The calculated work function of gold (4.7 eV) matches well with the value reported in the literature for the gold surface exposed to the ambient atmosphere.[287, 288]

Potential Interaction Mechanism of CO and Perovskite

For perovskite film processed in an ambient atmosphere, molecular O_2 can dissociatively adsorb on the perovskite surface in form of reactive atomic oxygen species (O_2^-, O^- and O^{2-}).[289] We hypothesize that when such perovskite surface is exposed to CO, the reducing tendency of the CO allows it to react with pre-adsorbed reactive oxygen species leading to the formation of CO_2 by following reactions:[290, 291]

$$CO + O^- \rightarrow CO_2 + e^-$$

$$CO + 2O^- \rightarrow CO_3^{2-} \rightarrow CO_2 + \frac{1}{2}O_2 + 2e^-$$

Previous studies suggest that CO_2 and moisture can form carbonic acid and later lead to the formation of bicarbonate and hydronium ions on the perovskite surface. The bicarbonate and hydronium ion may replace the corresponding I^- and MA^+ ions in the perovskite crystal structure leading to material

degradation and leaving behind PbI_2. The PbI_2 may form a stable complex of dicarboxyoxylead or $Pb(HCO_3)_2$.[292] The presence of the PbI_2CO complex has also been reported in previous studies.[293]

$$CO_2 + H_2O \rightarrow H_2CO_3$$

$$H_2CO_3 + H_2O \rightarrow HCO_3^- + H_3O^+$$

Alternatively, under light, iodide ions in the perovskite may undergo an oxidation process[24], with the released proton forming volatile formaldehyde as follows:

$$CH_3NH_3PbI_3 \leftrightharpoons PbI_2 + CH_3NH_3I$$

$$2CH_3NH_3I + CO \xrightarrow{h\vartheta} 2CH_3NH_2 + HCHO + I_2$$

More detailed studies are required to ascertain the exact nature of the interaction between CO and $MAPbI_3$.

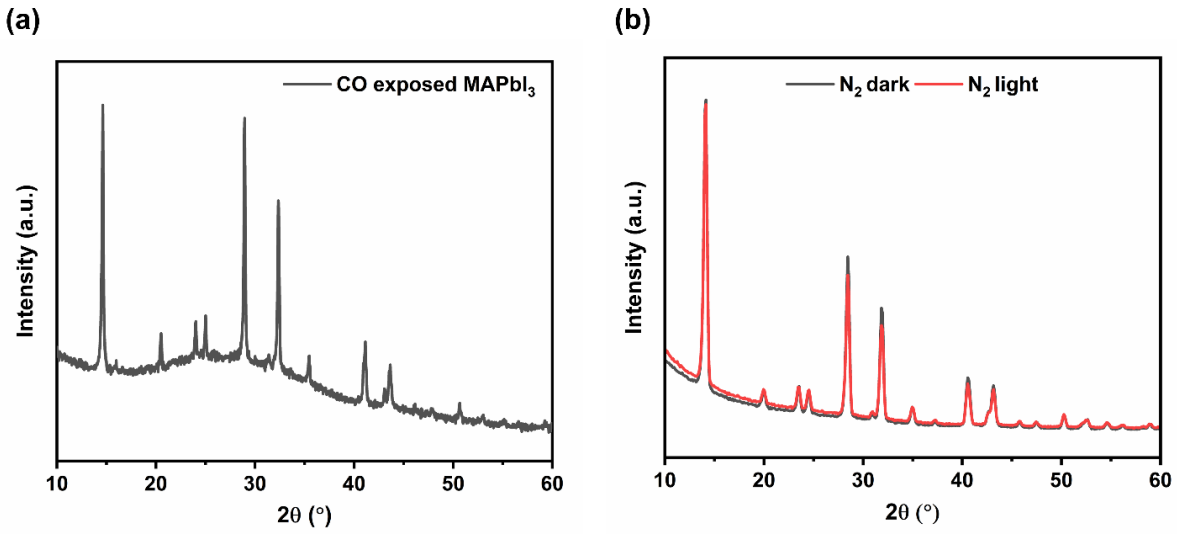

Figure A2.1 (a) Bulk XRD pattern of the $MAPbI_3$ film exposed to the CO environment confirming the absence of PbI_2 diffraction peak. Similarly, the PbI_2 impurity peak is not observed in the (b) GIXRD pattern of perovskite film stored in the N_2 atmosphere in dark and light.

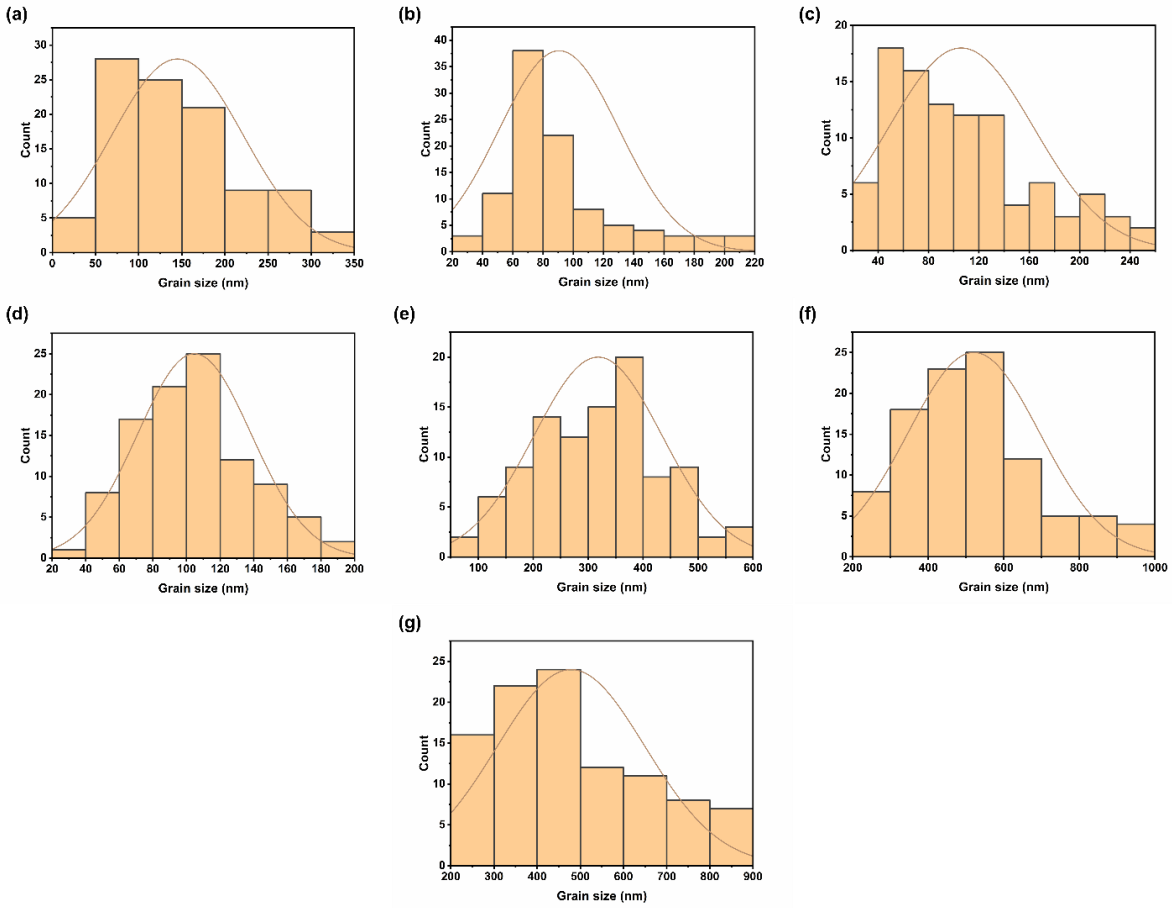

Figure A2.2 Grain size distribution observed in (a) pristine perovskite film and $MAPbI_3$ film exposed to CO in dark for (b) 1 hour, (c) 3 hours, and (d) 1 hour with poling. Grain size distribution in perovskite film exposed to CO in light for (e) 1 hour, (f) 1 hour with poling, and (g) 3 hours.

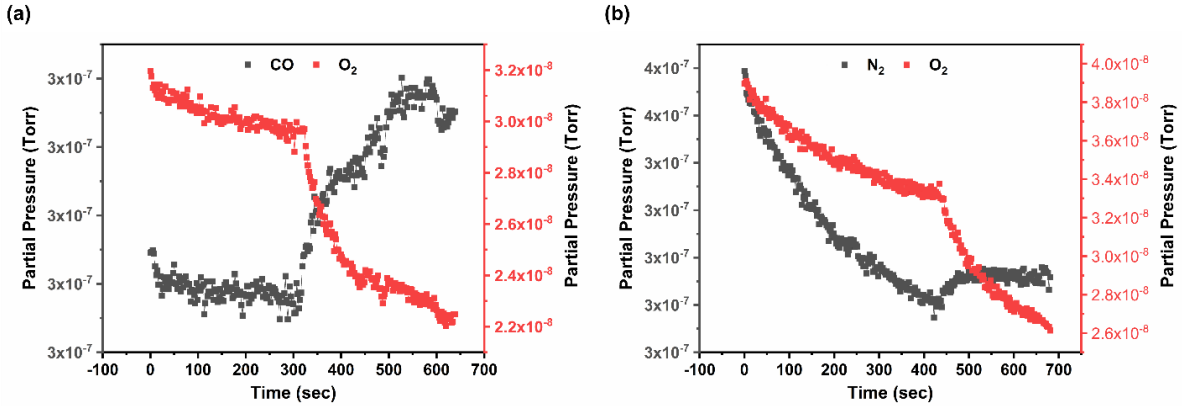

Figure A2.3 Analysis of gases present in the sealed beaker where (a) a bare glass substrate is stored in the CO atmosphere and (b) $MAPbI_3$ film is stored in the N2 atmosphere.

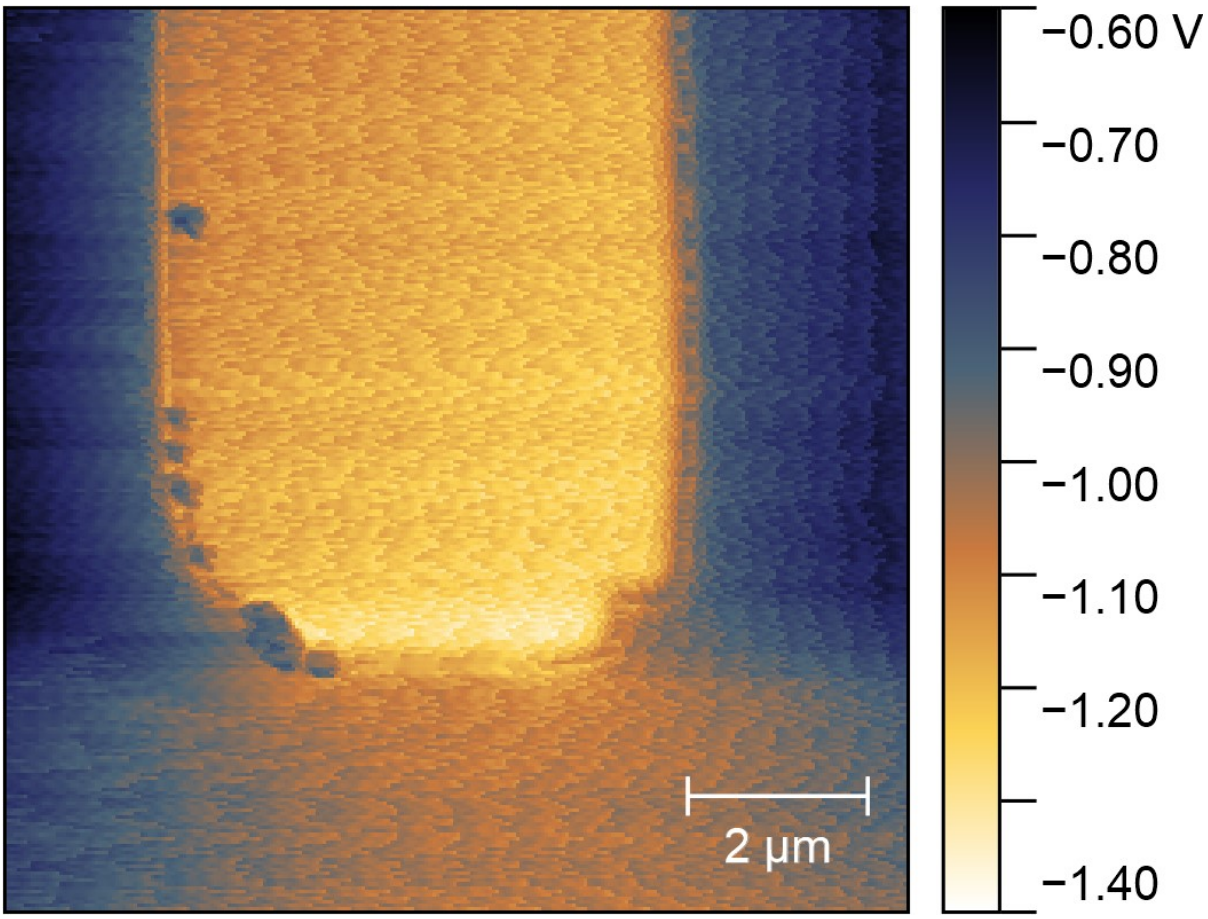

Figure A2.4 Surface potential map of gold electrode patterned over a Si/SiO_2 wafer. The corresponding work function value is calculated to be 4.7 eV.

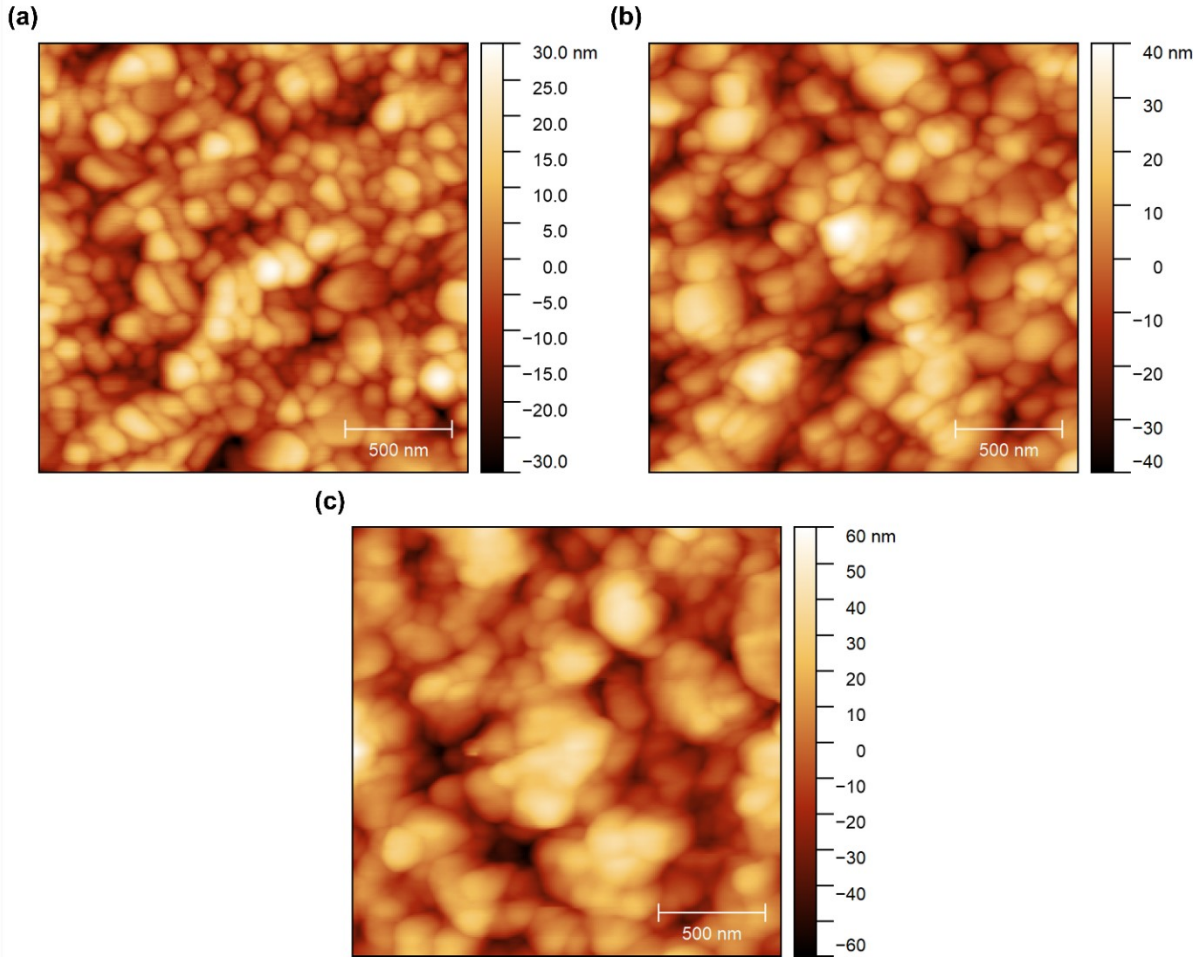

Figure A2.5 AFM topography maps indicate an increase in surface roughness of the perovskite film over time when exposed to CO for (a) 0, (b) 6, and (c) 24 hours.

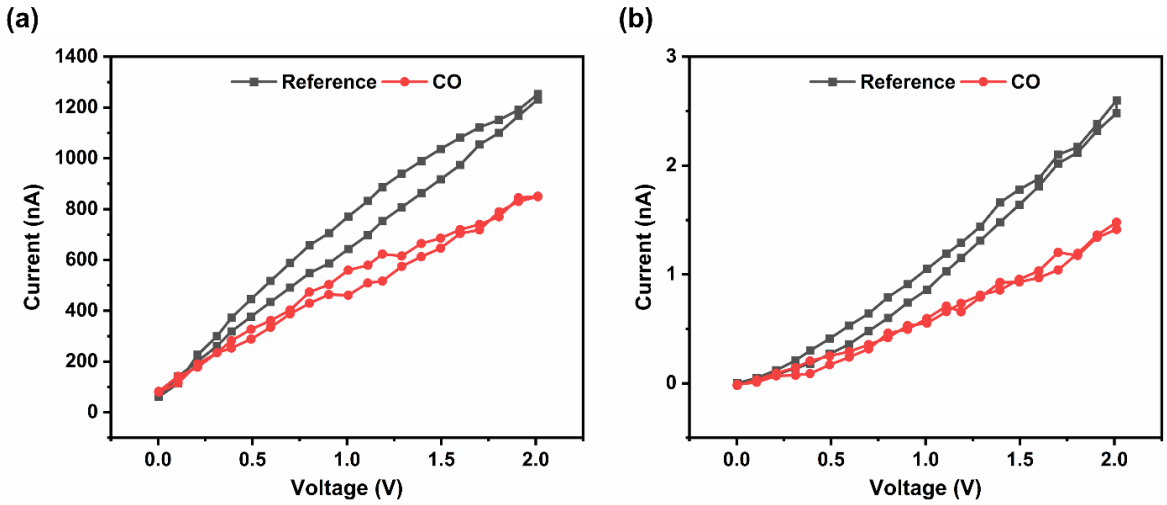

Figure A2.6 *I-V* curves of perovskite films exposed to ambient (reference) and CO atmosphere under (a) 1.0 sun illumination and in (b) dark.

Appendix for Chapter 3

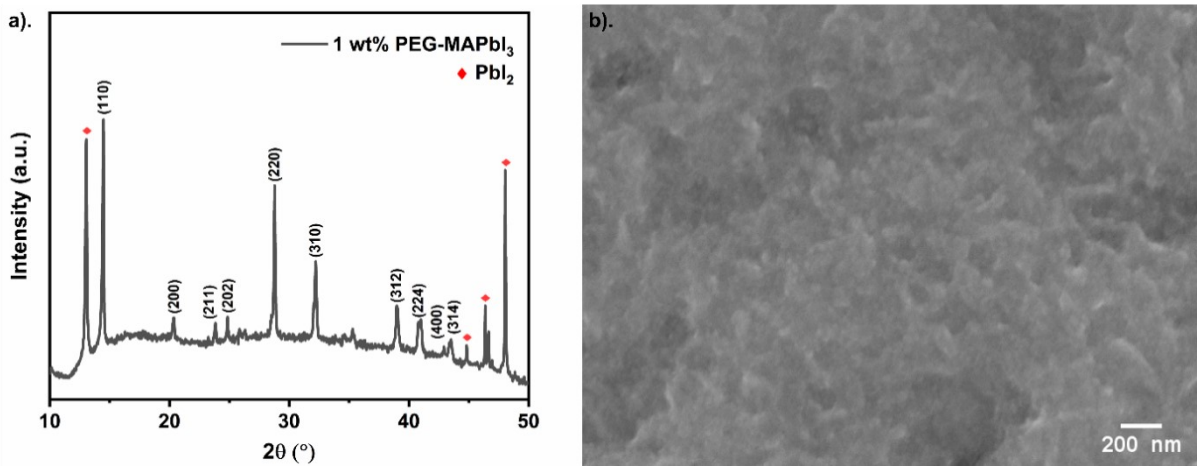

Figure A3.1 (a) XRD pattern and (b) SEM image of 1 wt/v % PEG-$MAPbI_3$ film.

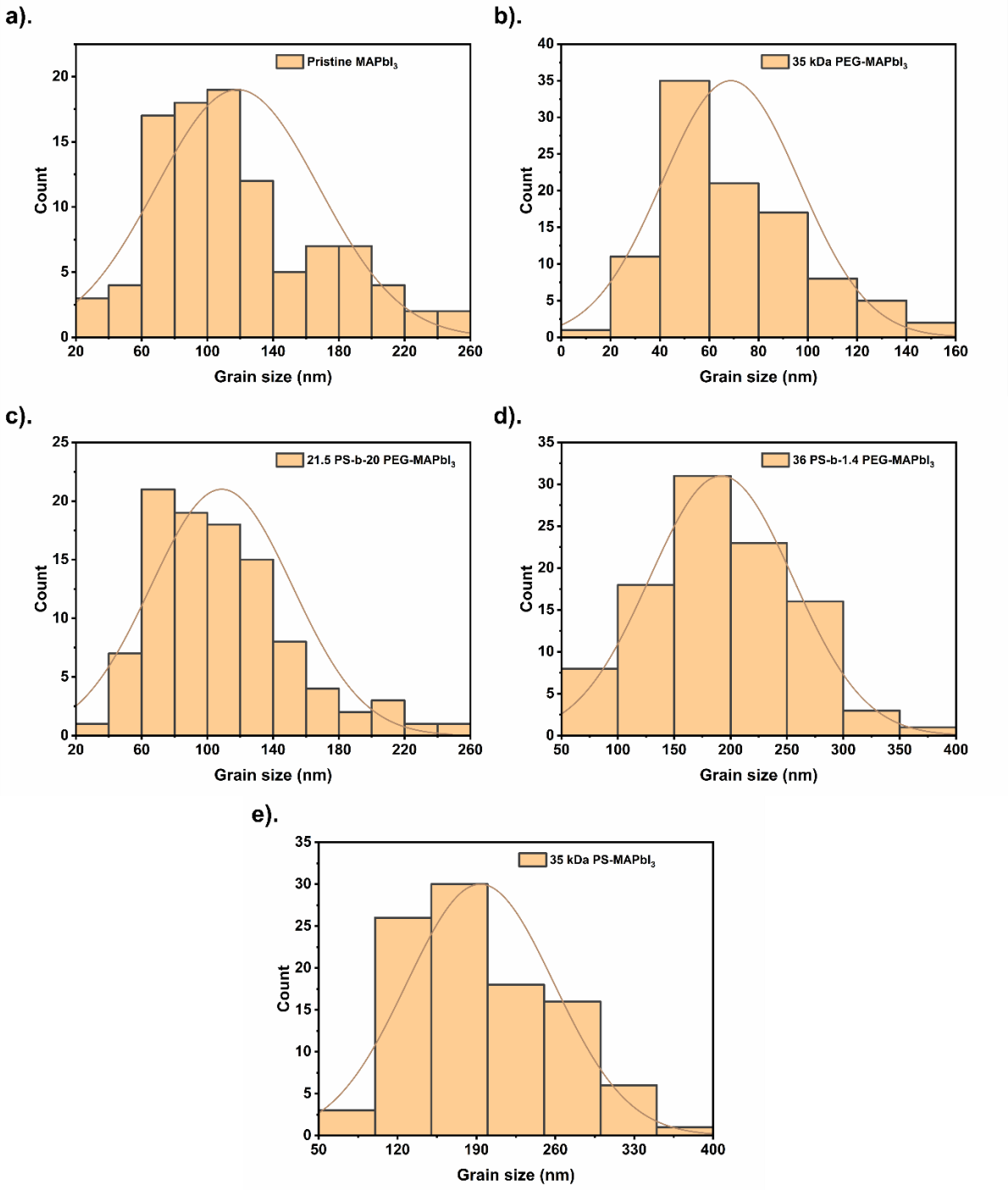

Figure A3.2 Grain size distribution in (a) pristine $MAPbI_3$, (b) 35 kDa PEG-$MAPbI_3$, (c) 21.5 PS-b-20 PEG-$MAPbI_3$, (d) 36 PS-b-1.4 PEG-$MAPbI_3$ and (e) 35 kDa PS-$MAPbI_3$.

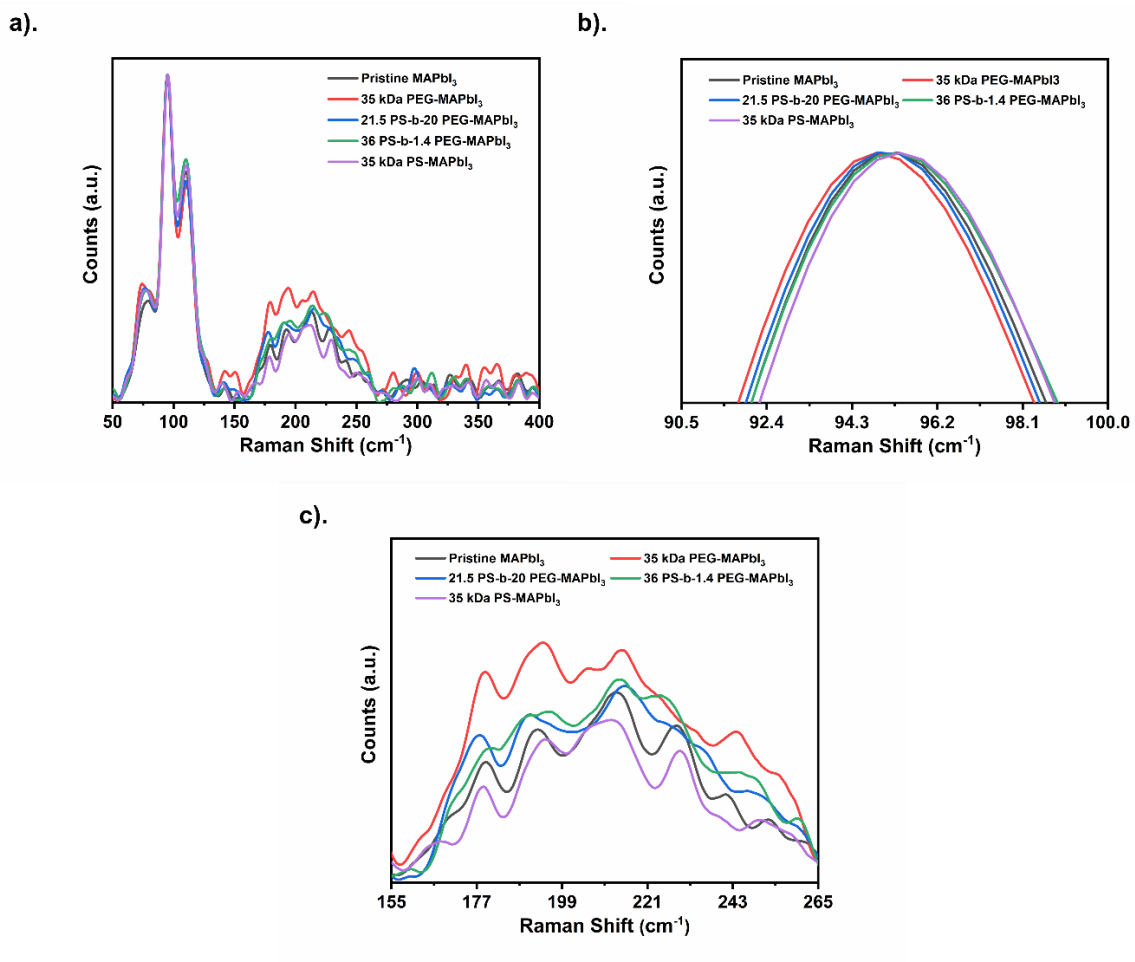

Figure 3.3 (a). Raman spectra of pristine and polymer-$MAPbI_3$ films. (b) Shifting of Pb-I liberation mode to higher wavenumber with an increase in PS content in the polymer-perovskite films and (c) Variation in Raman peaks corresponding to the torsional mode of MA^+ in polymer-$MAPbI_3$ films.

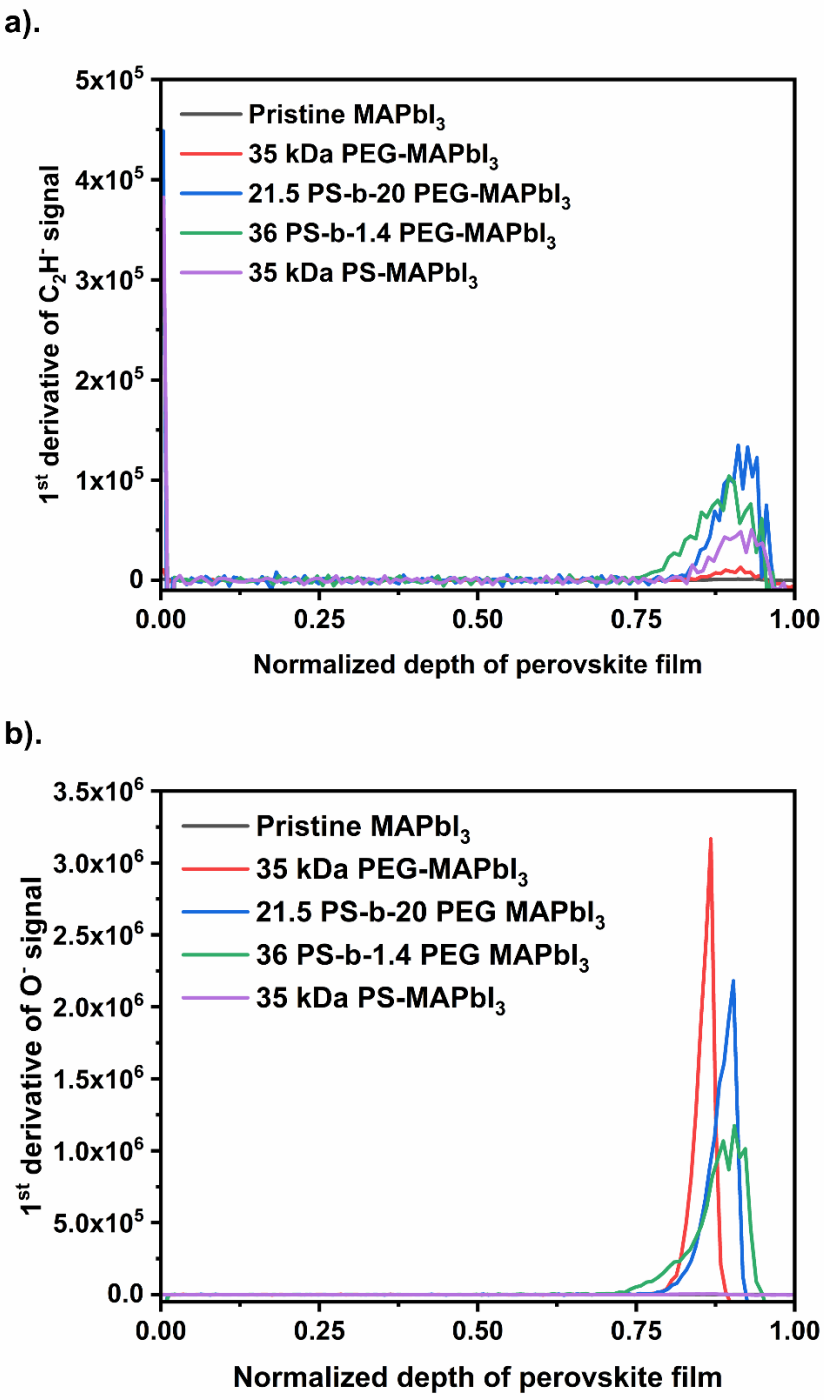

Figure A3.4 First derivative curves of the (a) C_2H^- and (b) O^- signals representative of the distribution of PS and PEG, respectively across the depth of the pristine and polymer-perovskite films.

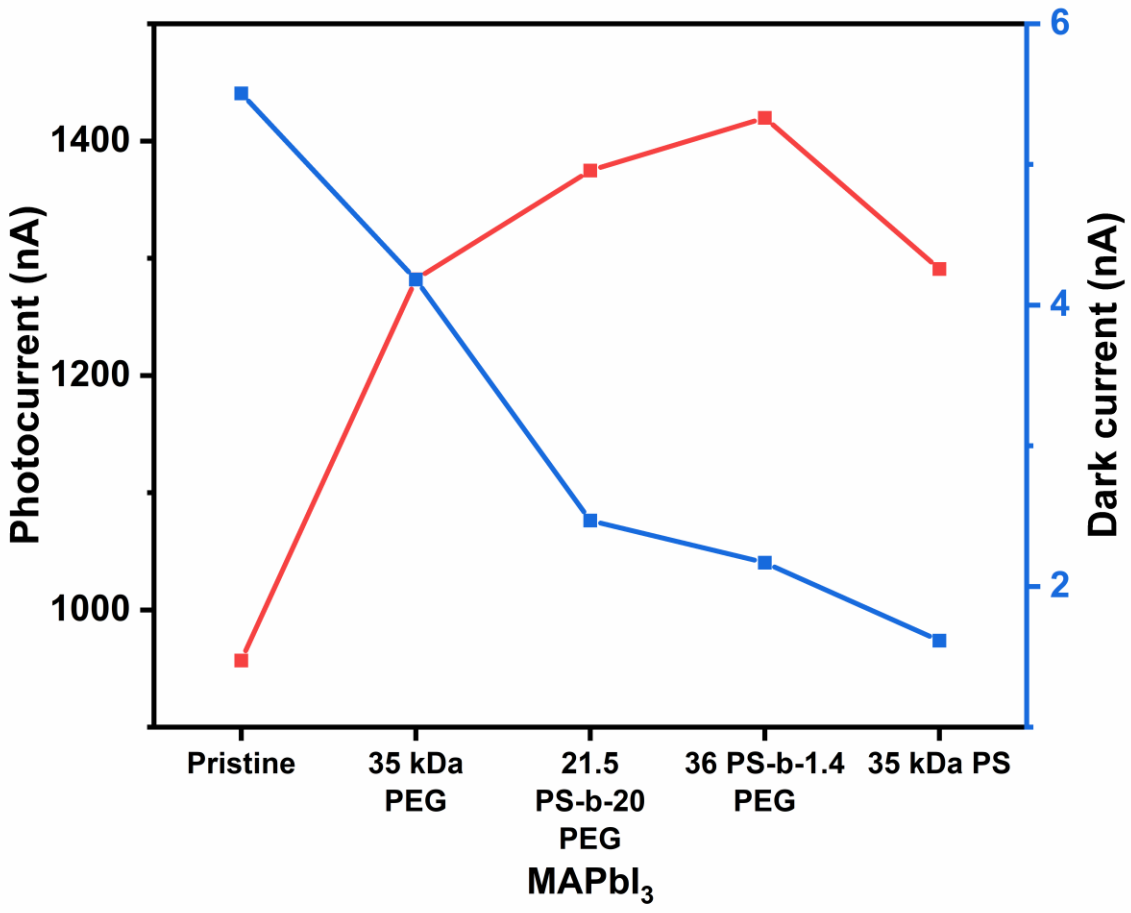

Figure A3.5 The trend of photocurrent and dark current values in pristine and polymer-$MAPbI_3$ films.

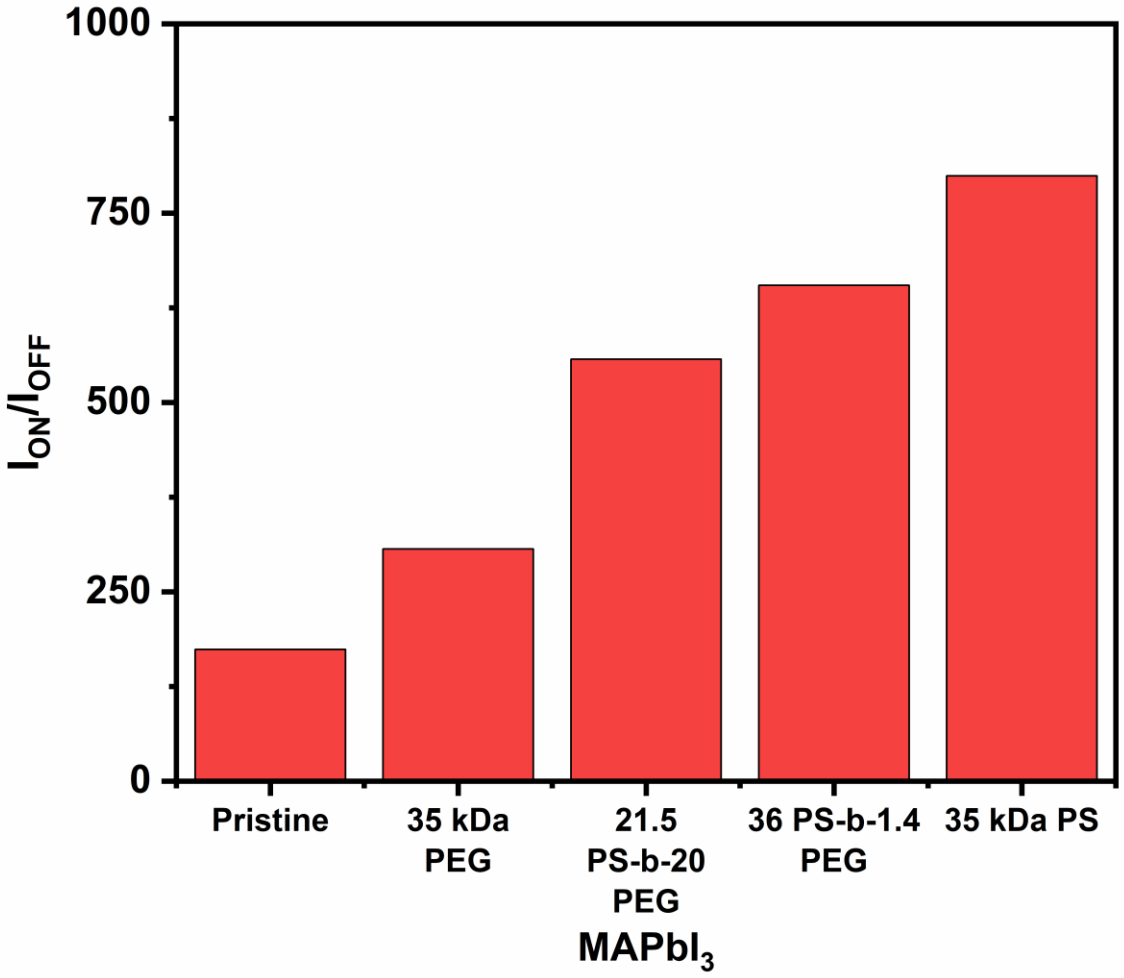

Figure A3.6 The ratio of photocurrent/dark current for pristine and polymer-perovskite films with different homopolymer and block copolymer additives.

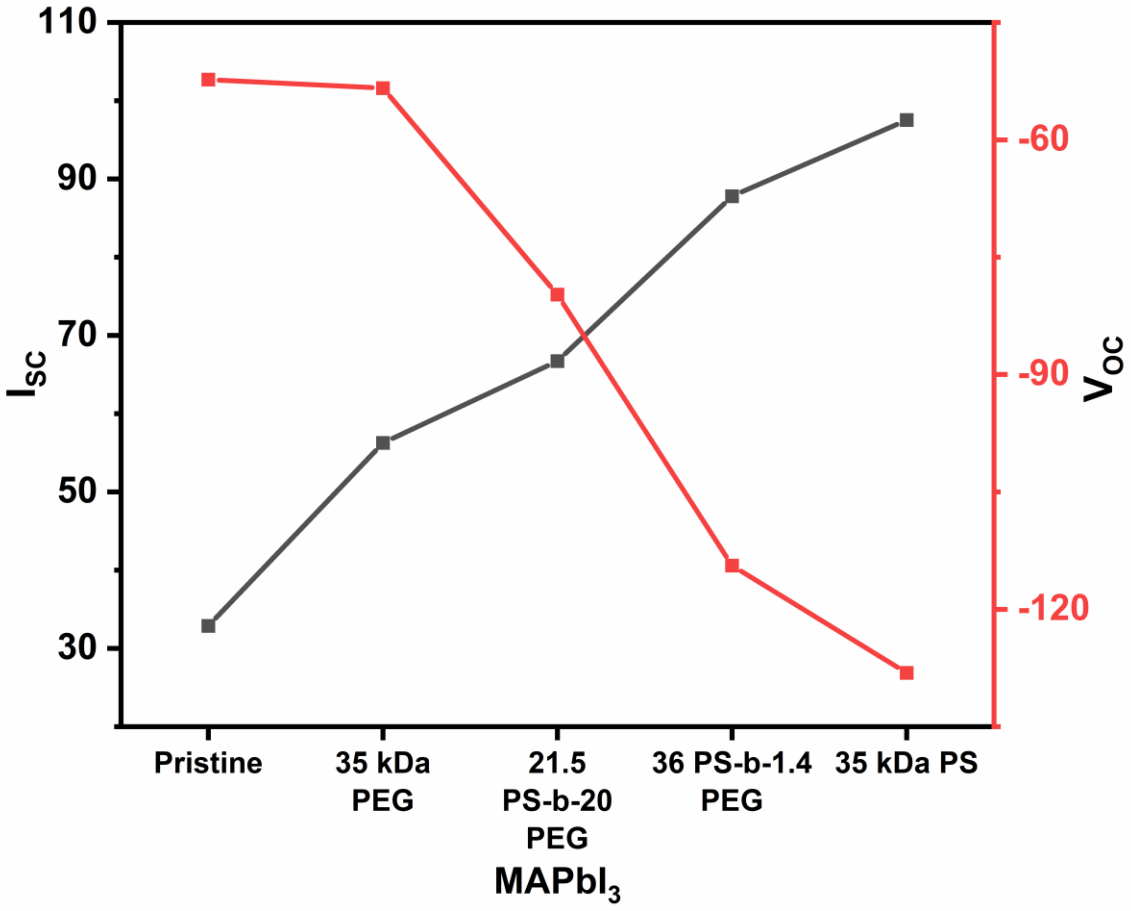

Figure A3.7 The trend of short-circuit current (Isc) and open-circuit voltage (Voc) values in pristine and polymer-$MAPbI_3$ films.

Appendix for Chapter 4

Modeling the effect of PS chains on $MAPbI_3$

The viscosity (η) of the polymer chains determines their mobility and in confined spaces scales based on the relationship shown in Equation 1.

$$\eta = K.Mw^{1.4} \quad \text{Equation A4.1}$$

The inclusion of the PS chains in the perovskite is directly affected by the viscosity of the chains. The number of PS chains in the perovskite layer, n, can be calculated based on the ToF-SIMS PS signal (C_2^-), C_{ps}, and the Mw of the PS used. This relationship is shown in Equation 2 below:

$$\mathrm{n} = \mathrm{Ki}.(\mathrm{Cps}/\mathrm{Mw}) \quad \text{Equation A4.2}$$

where K_i is a constant that relates the ToF-SIMS C_2^- signal to the concentration of the PS groups in the perovskite.

The number of polymer chains in the perovskite, n, is modeled as being inversely proportional to the corresponding chain viscosity, as shown in Equation 3.

$$n = \frac{a'}{\eta} + b = \mathrm{a}.Mw^{-1.4} + b \quad \text{Equation A4.3}$$

This equation accurately models the concentration of the PS chains in the perovskite as measured by the signal in ToF-SIMS.

The effect due to the presence of the polymer chains on the rate of nucleation R_N, for the inorganic phase, can be modeled as follows[294]:

$$R_N = C.\frac{kT}{3\pi\lambda^3\eta}.exp\left(-\frac{\Delta G^*}{kT}\right) \quad \text{Equation A4.4}$$

Here the key parameters are: C is the concentration of the species, k is the Boltzmann constant, T is the temperature, ΔG* is the energy barrier for nucleation, λ is the size of the species and η is the viscosity of the solvent.

Since our primary factor is the molecular weight of the polymer (Mw), it has two effects on the rate of nucleation: One, the viscosity changes based on the Mw of the polymer used during synthesis. Since

the concentration (based on the monomer) is the same for all samples, this dependence can be written as[179]:

$$\eta = K.Mw^{1.4} \quad \text{Equation A4.5}$$

Second, the change in the energy barrier due to the interaction between the PS chains and the perovskite is modeled as:

$$\Delta G^* = a_o - \frac{b_o}{1 - c_o x} \quad \text{Equation A4.6}$$

Here x is the total volume of the polymer chains in the solution.

$$x = n.(Mw)^{1.74} \quad \text{Equation A4.7}$$

where n is the number of polymer chains in the matrix (derived from the ToF-SIMS signal) and $(Mw)^{1.74}$ term[199] captures the scaling of the volume of polymer chains based on their Mw.

n α (signal in ToF-SIMS)/(Mw of the polymer used)

Based on this modulation, the energy barrier without any polymer addition is given by:

$$\Delta G^* = a_o - b_o \quad \text{Equation A4.8}$$

The electronic current across the perovskite films will depend inversely on the density of the grain boundaries, as they act as barriers for charge transport. The density of the grain boundaries is directly proportional to the rate of nucleation R_N; therefore, we can write:

$$\left(\frac{1}{I}\right) \propto \frac{K_1}{\eta}.exp\left(-a_1 + \frac{b_1}{1 - c_o x}\right) \quad \text{Equation A4.9}$$

The second effect due to the presence of the polymer chains in the perovskite matrix is that the local electric field across the grain boundaries for charge transport is altered. The polymer chains are dielectric in nature and hence are considered a tunneling barrier. The current is hence related to the size of this barrier based on the following equation[295]:

$$I \propto K.\exp\left(-\frac{E_c.x}{V}\right) \quad \text{Equation A4.10}$$

Here E_C is the critical field for tunneling, and K is a constant dependent on other material characteristics. V is the applied potential and x is the volume of the polymer in the perovskite matrix which has been defined above.

Combining the two effects we get the net effect from the inclusion of the polymer in the perovskite as:

$$\frac{1}{I} \propto \frac{K_o}{\eta}.exp\left(-a_1 + \frac{b_1}{1-c_o x}\right)\exp\left(\frac{E_c.x}{V}\right) \quad \text{Equation A4.11}$$

Rearranging the terms and combining the constants we can write the final relationship as:

$$\ln\left(\frac{\eta}{I}\right) = a' + \frac{b_1}{1-c_o x} + d'x \quad \text{Equation A4.12}$$

which can then be simplified to:

$$\ln\left(\frac{\eta}{I}\right) = \frac{\alpha + \beta x + \gamma x^2}{1-c_o x} \quad \text{Equation A4.13}$$

This basic structure of dependence will be followed for dark current due to electronic charges, ionic currents from ion migration, and photocurrent. The difference will arise in the sign associated with the terms (α, β, γ, c_o). E.g., in the case of ionic currents since the grain boundaries serve as paths for ion migration they will increase with the rate of nucleation, and hence the associated term will have the opposite sign compared to the dark current and photocurrent.

Based on this we fit the three currents to this model.

$$\ln\left(\frac{\eta}{I_{ion}}\right) = \frac{\alpha + \beta x + \gamma x^2}{1-c_o x} \quad \text{Equation A4.14}$$

$$\ln\left(\frac{\eta}{I_{dark}}\right) = \frac{\alpha + \beta x + \gamma x^2}{1-c_o x} \quad \text{Equation A4.15}$$

$$\ln\left(\frac{\eta}{I_{Ph}}\right) = \frac{\alpha + \beta x + \gamma x^2}{1-c_o x} \quad \text{Equation A4.16}$$

The mode fits the response from $MAPbI_3$ as seen in Figure 4.6 in the main text. It illustrates that the effect of the polymer is based on two important aspects, the modulation of the crystallization kinetics and the insulating nature of the PS.

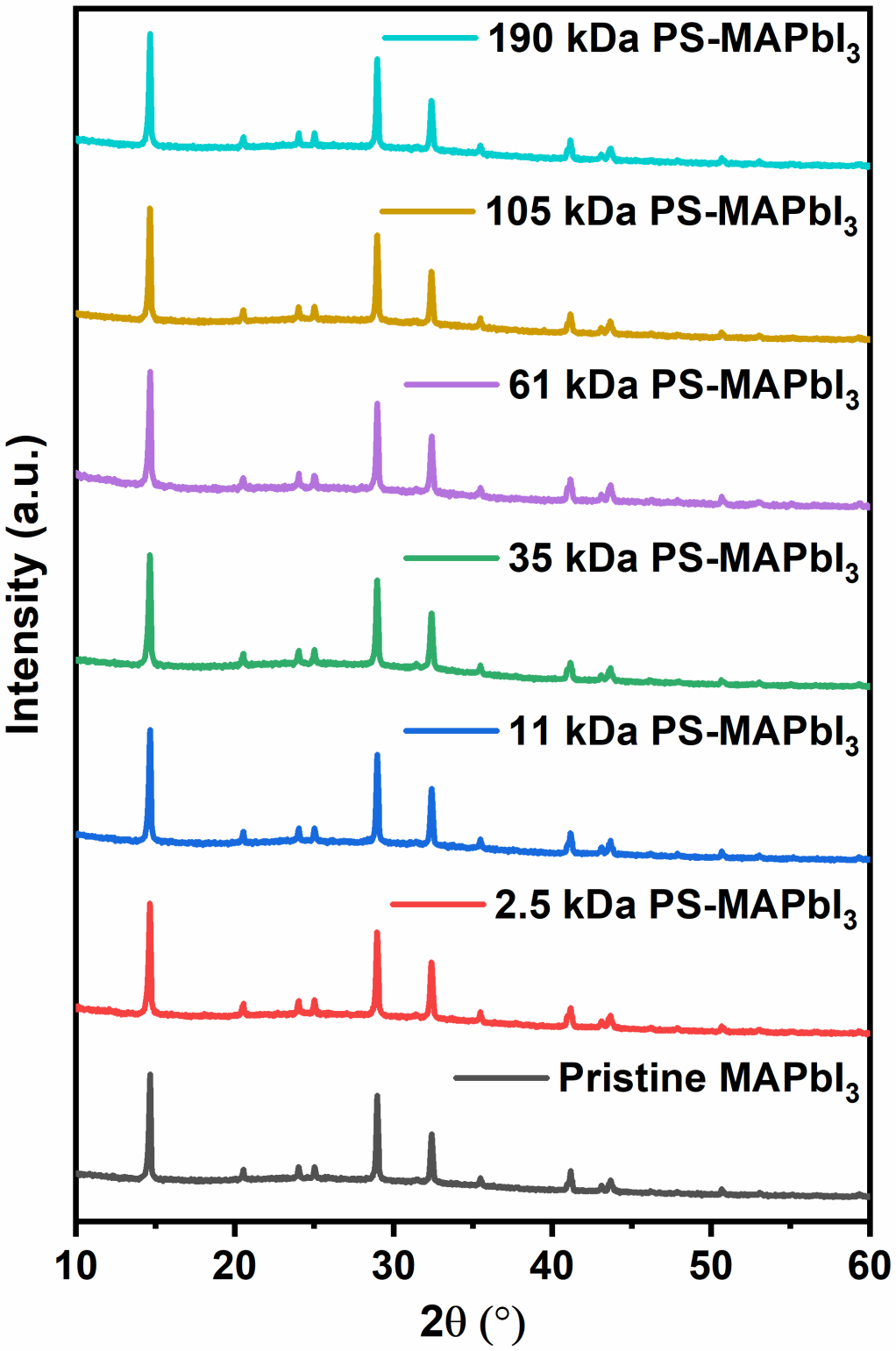

Figure A4.1 X-ray diffraction pattern of pristine $MAPbI_3$ and PS-$MAPbI_3$ with varying polymer Mw.

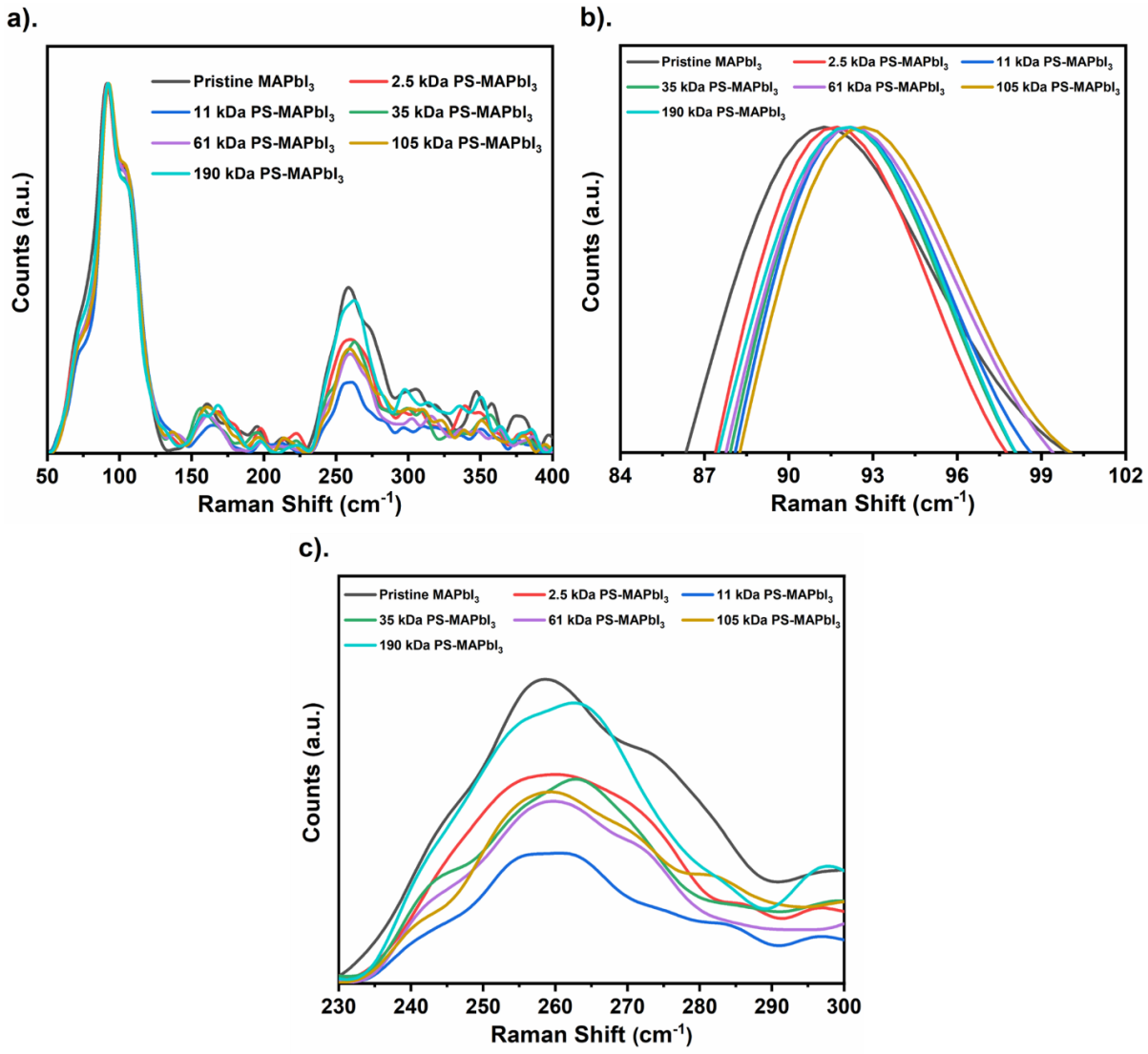

Figure A4.2 (a) Raman spectra of pristine $MAPbI_3$ and PS-$MAPbI_3$ films of varying Mw. (b) Shifting of Pb-I liberation mode to higher wavenumber in PS-$MAPbI_3$ films with an increase in Mw of PS and (c) Variation in Raman peaks corresponding to the torsional mode of MA^+ in PS-$MAPbI_3$ films.

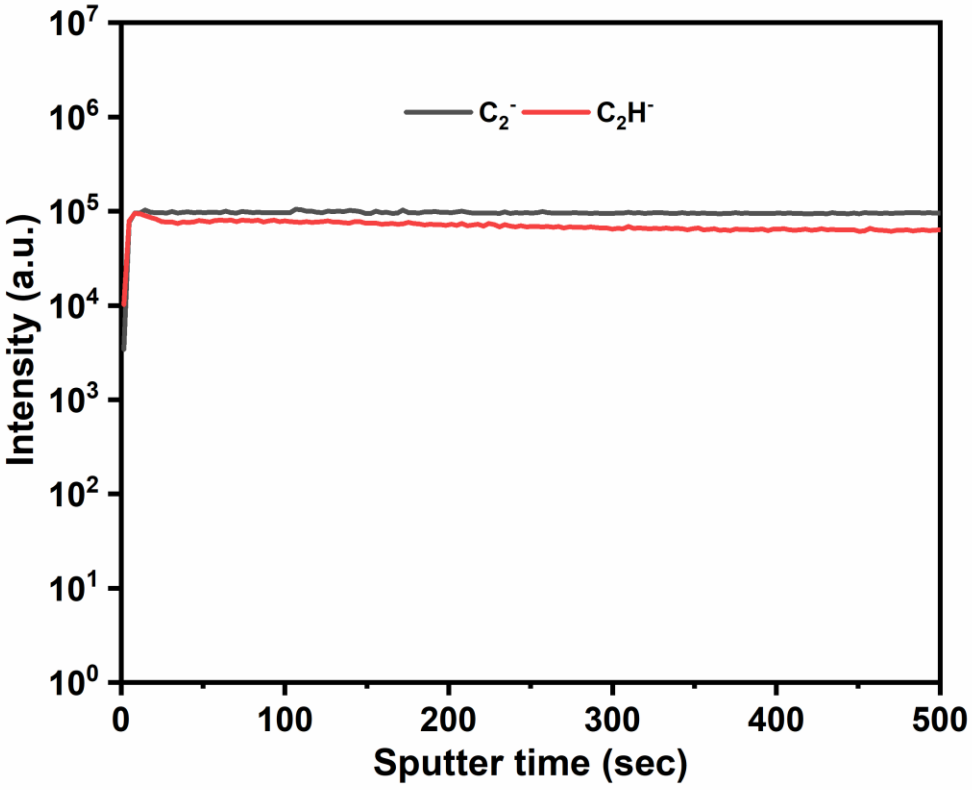

Figure A4.3 ToF-SIMS depth profiling of pristine PS film.

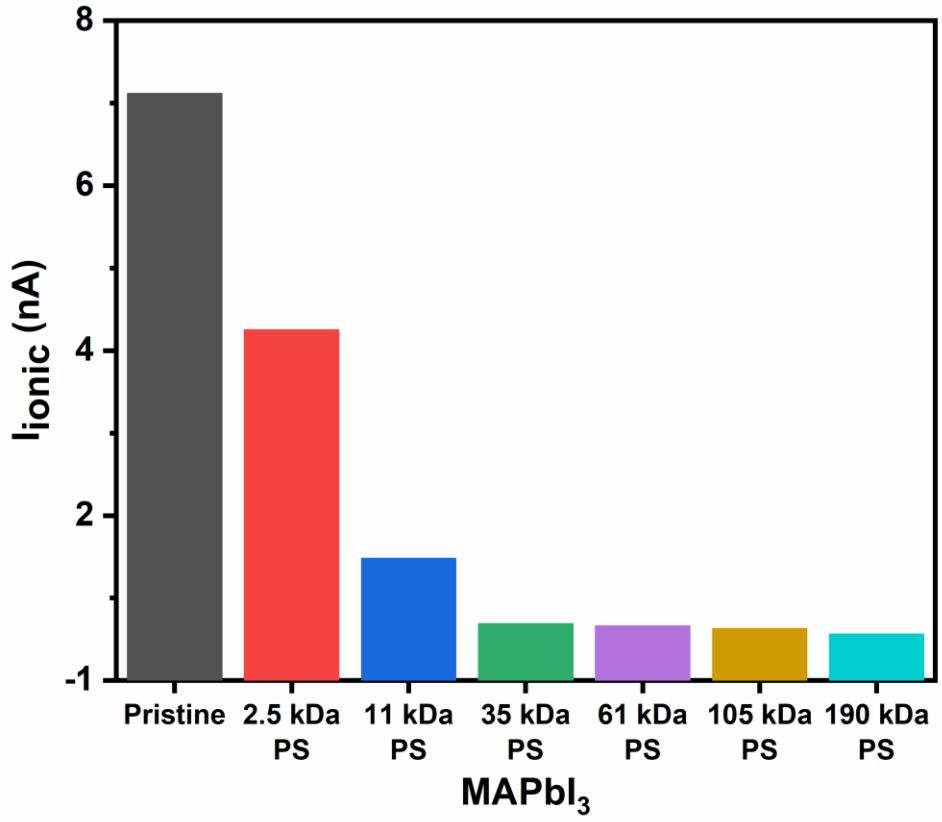

Figure A4.4 The decrease in ionic current in PS-$MAPbI_3$ films with an increase in Mw of PS. The ionic current is representative of ion migration and can be measured in terms of decay from the initial to a final stable value of the dark current.

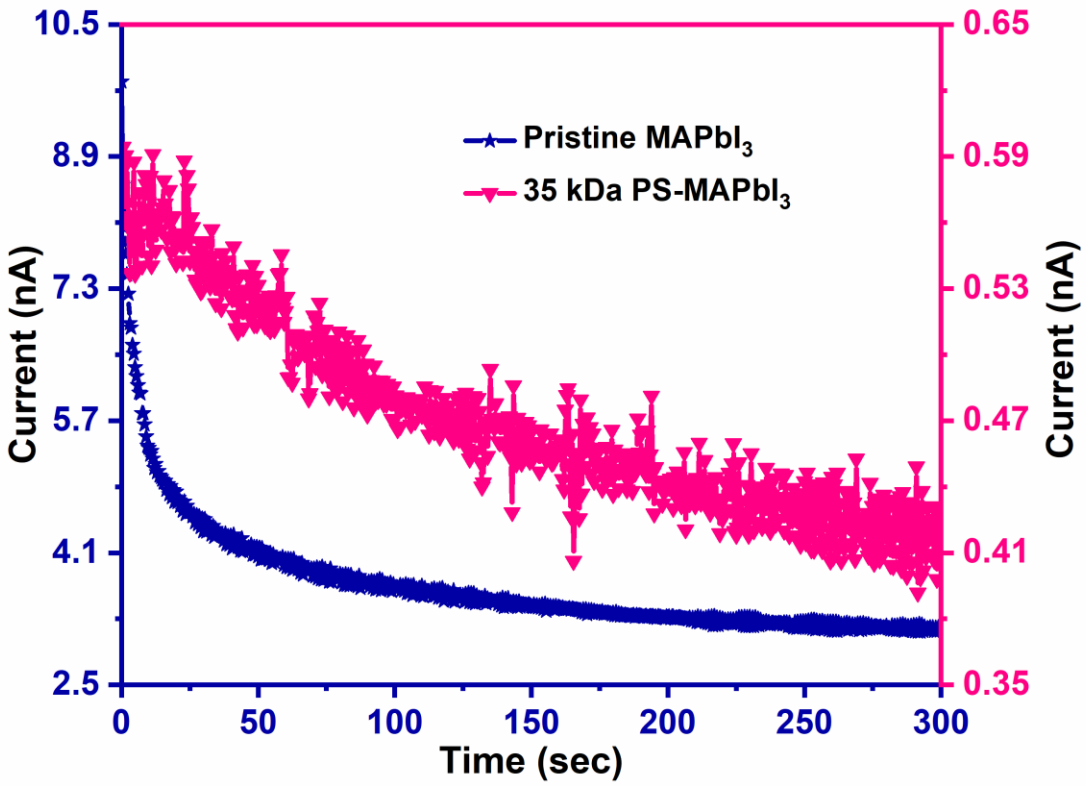

Figure A4.5 The decay of dark current in pristine and 35 kDa PS-$MAPbI_3$.

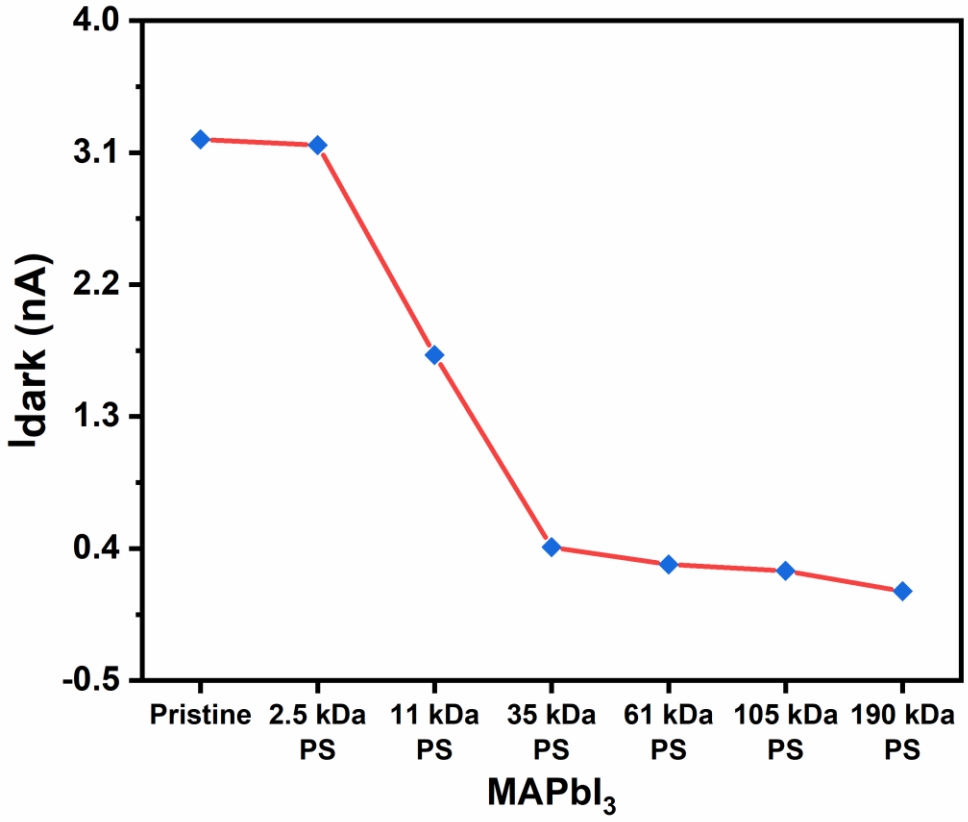

Figure A4.6 The trend of final values of dark current in pristine and PS-$MAPbI_3$.

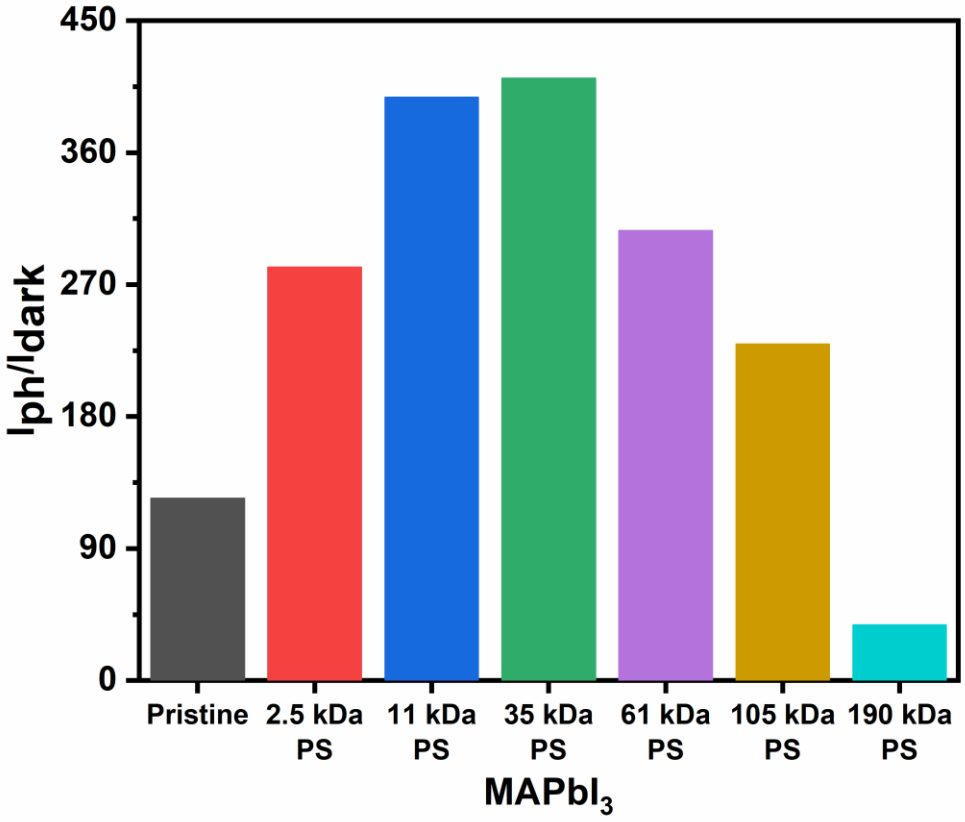

Figure A4.7 The ratio of photocurrent/dark current for pristine and PS-$MAPbI_3$ with varying Mw.

Table A4.1 Crystallite grain size in pristine $MAPbI_3$ and PS-$MAPbI_3$ films with varying Mw, calculated using Scherrer's equation for 2θ of 14.66° corresponding to the (1 1 0) lattice plane.

Absorber Material	FWHM	Crystallite size (nm)
Pristine MAPbI3	0.13904	60.19
2.5 kDa PS-$MAPbI_3$	0.13958	59.91
11 kDa PS-$MAPbI_3$	0.13019	64.28
35 kDa PS-$MAPbI_3$	0.1215	68.88
61 kDa PS-$MAPbI_3$	0.12793	65.42
105 kDa PS-$MAPbI_3$	0.13732	60.94
190 kDa PS-$MAPbI_3$	0.14224	58.84

Appendix for Chapter 5

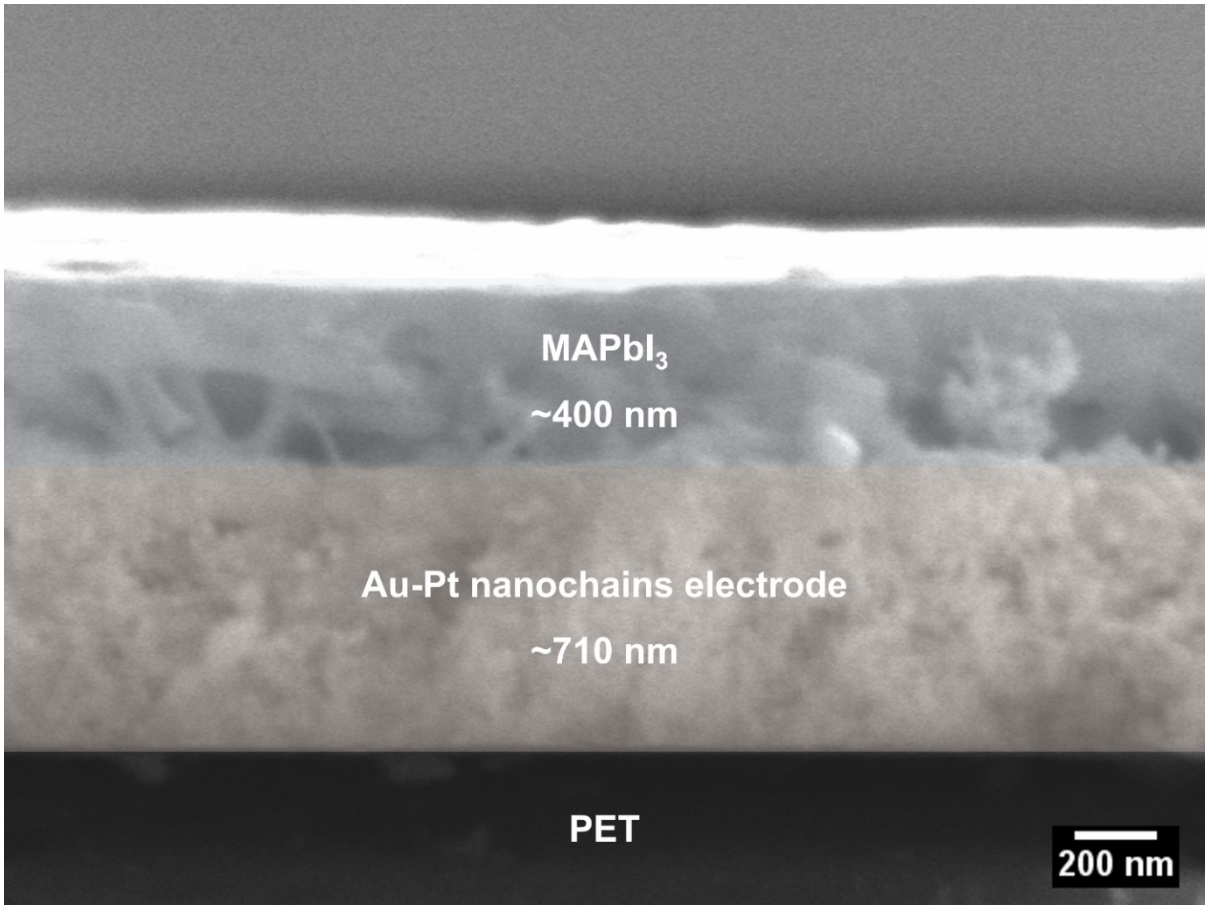

Figure A5.1 Cross-section FE-SEM image of perovskite and nanochains electrode deposited over PET substrate.

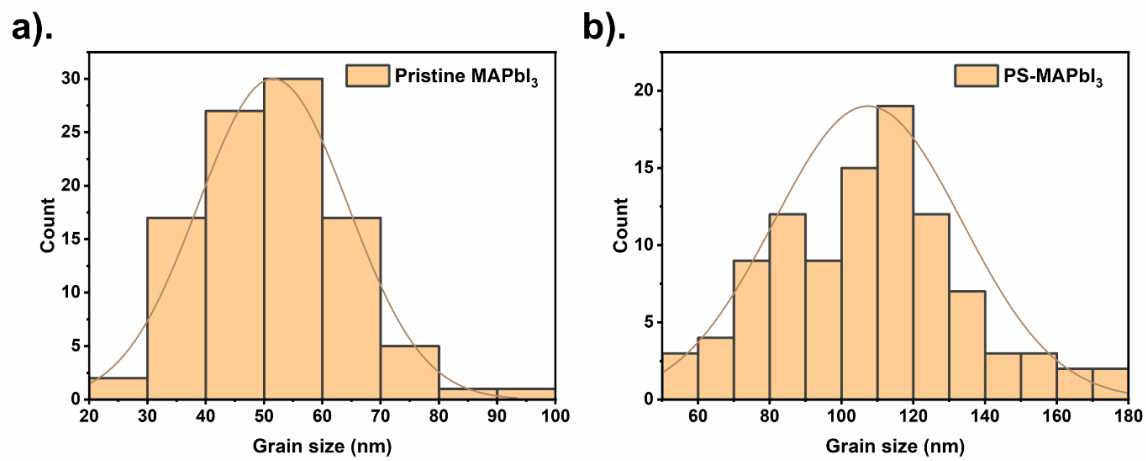

Figure A5.2 Grain size distribution in pristine and PS-$MAPbI_3$ films. The average grain size of pristine and PS-$MAPbI_3$ film is observed as 50 nm and 110 nm, respectively.

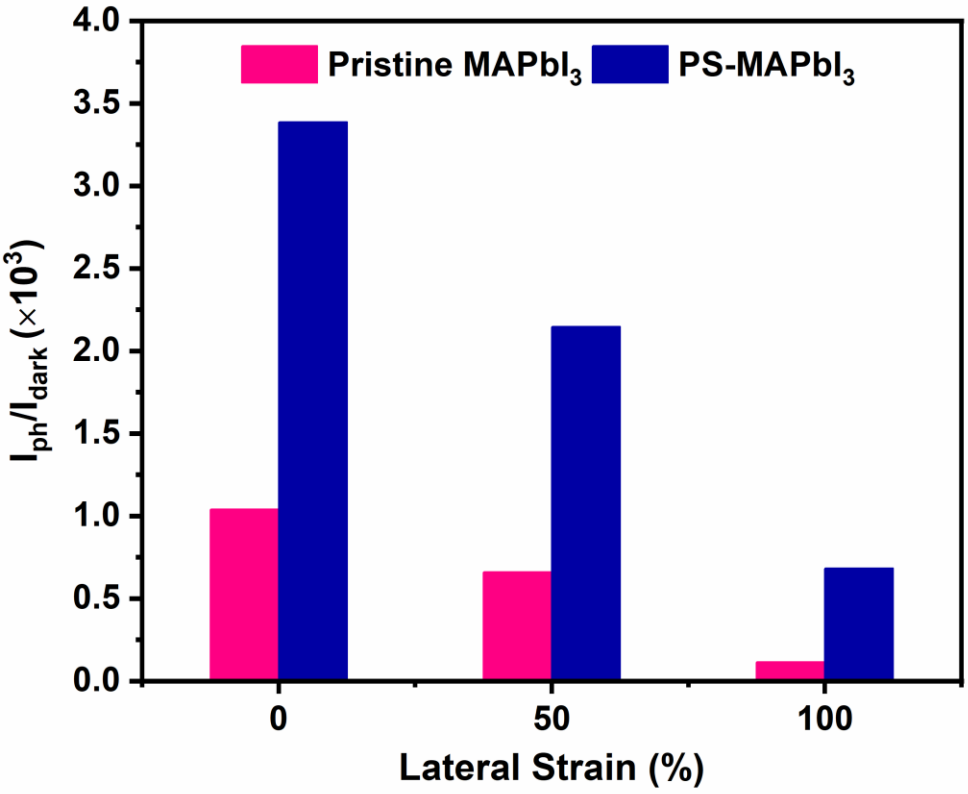

Figure A5.3 Light switching (on/off) ratio of pristine and PS-$MAPbI_3$ photodetectors under variable lateral strain at 3.5 V under 1.0 sun illumination.

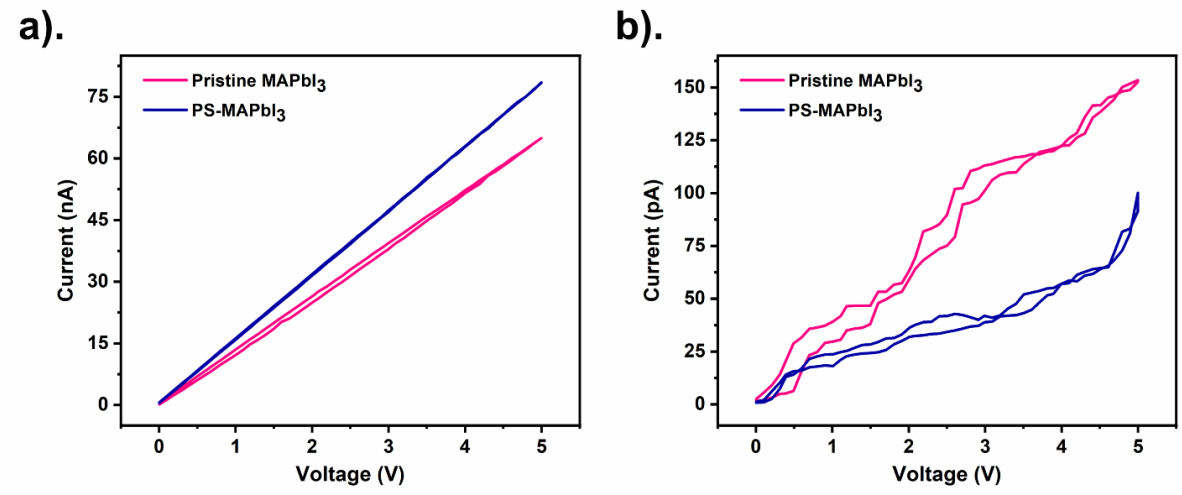

Figure A5.4 *I-V* curves of pristine and PS-$MAPbI_3$ photodetectors at 50% strain under (a) 1.0 sun illumination and in (b) dark.

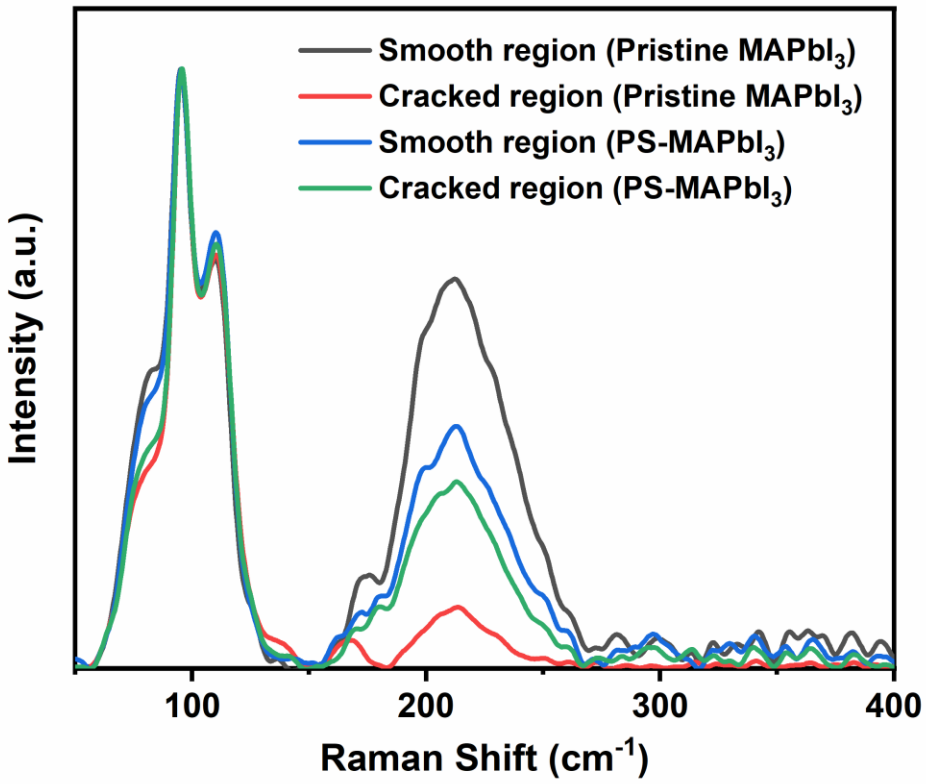

Figure A5.5 Raman spectra of smooth and cracked regions of pristine and PS-$MAPbI_3$ films after 5 stretching cycles.

Table A5.1 Performance comparison with some previously reported stretchable perovskite-based photosensitive devices and our previous work with Au/PS-$MAPbI_3$/Au lateral configuration on a rigid substrate.

Device	Flexible substrate	Device structure	Active device area	Optoelectronic characteristics	Sustainable strain	Stretching cycles and reduction in relative performance	Ref.
Solar cell	PDMS	PDMS/virus-templated Au nanowires/PTAA/$MA_{0.6}FA_{0.4}PbI_{2.9}Br_{0.1}$/$C_{60}$/BCP/Au	0.04 cm^2	Jsc: 13.1 mA cm^{-2}, Voc: 0.86 V, FF: 0.66 and PCE: 9.28%	8%		[232]
Solar cell	PDMS	PDMS/PEDOT:PSS/PEDOT:PSS Al4083/perovskite/PCBM/PEI/ PEDOT:PSS/PDMS	0.16 cm^2	Jsc: 22.34 mA cm^{-2}, Voc: 1.09 V, FF: 0.79 and PCE: 19.15%	20%	PCE drops to 34% after 1000 stretching cycles at 20% strain - recovers back to 88% after annealing	[233]
Solar cell	PDMS	PDMS/PEDOT:PSS (PH 1000)/PEDOT:PSS Al4083/perovskite/PCBM/PEI/PEDOT:PSS/Cu	1.01 - 9.33 cm^2	PCE: 15.01% on stretchable substrate, 13.1% and 11.2% under 10% and 20% stretching	20%	86% and 73% of original PCE maintained after 10% and 20% stretching tests, respectively, for 5000 cycles	[150]

Solar cell	Silk fibroin combined with Ag nanowire (SDE)	SDE/highly conductive PEDOT:PSS(PH1000)/PEDOT:PSS/$CH_3NH_3PbI_3$/PCBM/Ag	0.0625 cm^2	Jsc: 18.47 mA cm^{-2}, Voc: 0.99 V, FF: 56.84% and PCE: 10.40%	50%	PCE reduced to 60% after 50 cycles at 50% strain	[234]
Kirigami Solar cell	Eco-flex	ITO-PET/SnO_2 nanocrystals/$(FAPbI_3)_{0.85}(MAPbBr_3)_{0.15}$/Spiro-OMeTAD/Au sandwiched between Eco-flex	0.10 cm^2	Jsc: 22.41 mA cm^{-2}, Voc: 1.096 V, FF: 71.97% and PCE: 17.68%.	80%	PCE reduced to 87% after 300 cycles at 80% strain	[235]
Photodetector array (6×6)	Cellulose paper	Ag/$MAPbI_3$/Ag on cellulose paper		spectral range: 420-700 nm, working bias: 9V, photocurrent: 240 nm at 700 nm under 100 mW cm^{-2} illumination	85%		[236]
Photodetector	PDMS/PMMA/graphene	Ag/$MAPbBr_3$/Ag on PDMS/PMMA/graphene	100 μm channel length	Operating wavelength: 325 nm, response speed <200 ms, photocurrent: ~2.5 × 10^6 A and responsivity ~6 × 10^5 A W^{-1} under 6 × 10^{-4} W m^{-2} power density, detectivity ~8×10^{12} Jones at 0% strain	100%	Consistent photoresponse maintained after 125 cycles at 100% strain	[238]

Photodetector	VHB/graphene	Au/$MAPbI_3$/Au on VHB/graphene	4.225 × 10^{-5} cm^2	Wavelength: 375-785 nm, 0.01V working bias, response time 0.068 s, responsivity of 2.2 mA W^{-1} and detectivity of 1.78×10^5 Jones at 0% strain under 13.5 mW cm^{-2} irradiance power density	100%	Photocurrent reduced to 6% after 100 cycles at 50% strain	[239]
Kirigami Solar cell	cellophane paper	Cellophane/TiO_2-Ag-TiO_2/CPTA/$MAPbI_3$/Spiro-OMeTAD/Au	0.096 cm^2	Jsc: 17.81 mA cm^{-2}, Voc: 1.04 V, FF: 71.30% and PCE: 13.19%.	200%	PCE reduces by 1.9% after 1000 cycles	[237]
Photodetector	Si/SiO_2	Au/$MAPbI_3$/Au	0.14 × 10^{-3} cm^2	Operating wavelength: 400-710 nm responsivity 0.61 A/W, detectivity of 1.5 × 10^{13} Jones, response time of 10-20 ms and switching ratio >3 × 10^4 in self powered mode	0%		[118]
Photodetector	VHB/PET	Pt-Au nanochains/$MAPbI_3$/Pt-Au nanochains	0.10 cm^2	Operating wavelength: 400-800 nm, response speed <5 ms, responsivity 2.05 mA W^{-1} and detectivity 0.36×10^{12} Jones at 50% strain	100%	PCE reduced to 52% after 10,000 cycles at 50%	This work

PDMS - Polydimethylsiloxane, PTAA - Poly(triarylamine), BCP - Bathocuproine, PEDOT:PSS - Poly(3,4-ethylenedioxythiophene)-poly(styrene sulfonate), PCBM - Phenyl-C61-butyric acid methyl ester, CPTA - 2-(4-Chlorophenylthio)triethylamine hydrochloride, PEI - Polyethylenimine, PMMA - Polymethyl methacrylate, VHB - Very High Bond tape, PET - Polyethylene terephthalate, Jsc – Short-circuit current density, Voc - Open circuit voltage. FF - Fill factor, PCE - Power conversion efficiency

Modeling of amplitude and wavelength of the wrinkled pattern

The basic structure of the device consists of three layers:

I). The base substrate of elastomeric 3M™ VHB™ 4910 tape. Its mechanical parameters are: Poisson's ratio (υ) = 0.49; Elastic modulus (E) = 1.8 MPa; Thickness (h) = 1 mm.

II). The middle layer of PET film: υ = 0.4; E = 2.5 GPa; h = 12.5 μm.

III). The top perovskite layer: υ ~ 0.3; E = 11.7 – 7.1 GPa; h = 400 nm.

During the wrinkle formation, both the perovskite and the PET layer have to be strained, therefore given their adhesion, we assume them to be similar to two springs in parallel. Therefore, we can add their moduli to find the parameters of wrinkling. Due to the significantly lower thickness of the perovskite layer, the thickness of only the PET layer is considered. The basic mechanics of the structure is governed by the base substrate (identified by subscript 's' in equations below) and the PET-Perovskite film (identified by subscript 'f').[248, 249]

The basic equations that govern the profile of the pattern ($w(x)$), its wavelength (λ), the amplitude (A_o), and the peak strain (ε_{peak}) on the material are listed below:

$$w = A_o.Cos\left(\frac{2\pi}{\lambda}x\right) \quad \text{Equation 1}$$

$$\lambda = \frac{\lambda_o}{(1+\epsilon_{pre}).(1+\xi)^{1/3}} \quad \text{Equation 2}$$

$$A = \frac{A_o}{\sqrt{(1+\epsilon_{pre}).(1+\xi)^{1/3}}} \quad \text{Equation 3}$$

$$\lambda_o = 2\Pi h_f \left(\frac{\bar{E}_f}{3.\bar{E}_s}\right)^{1/3} \quad \text{Equation 4}$$

$$\xi = \frac{5.\epsilon_{pre}(1+\epsilon_{pre})}{32} \quad \text{Equation 5}$$

$$\epsilon_{peak} = 2.\sqrt{\epsilon_{pre}\epsilon_c}\frac{(1+\xi)^{1/3}}{(1+\epsilon_{pre})^{1/2}} \quad \text{Equation 6}$$

$$\epsilon_c = \frac{1}{4}\left(\frac{3.\bar{E}_s}{\bar{E}_f}\right)^{2/3} \quad \text{Equation 7}$$

$$A_o = h_f\sqrt{\frac{\epsilon_{pre}}{\epsilon_c} - 1} \quad \text{Equation 8}$$

$$\bar{E}_s = \frac{E_s}{1-\upsilon_s^2}$$ Equation 9

$$\bar{E}_f = \frac{E_f}{1-\upsilon_f^2}$$ Equation 10

Here, ϵ_c represents the critical or minimum strain necessary for the buckling to occur, and $\bar{E}$ signifies plane-strain moduli.

Based on the material parameters and the pre-stretching strain (ϵ_{pre}) of 100 %, we calculate the theoretical values for the pattern: λ = 0.47 mm; ϵ_{peak} = 7.5 % and an amplitude of 120 μm. These values match closely to the observed experimental value for the wavelength ~0.6 mm and amplitude ~350 μm.

The larger value in the actual device could be due to the thickness effect of the perovskite layer and shear displacement.

Appendix for Chapter 6

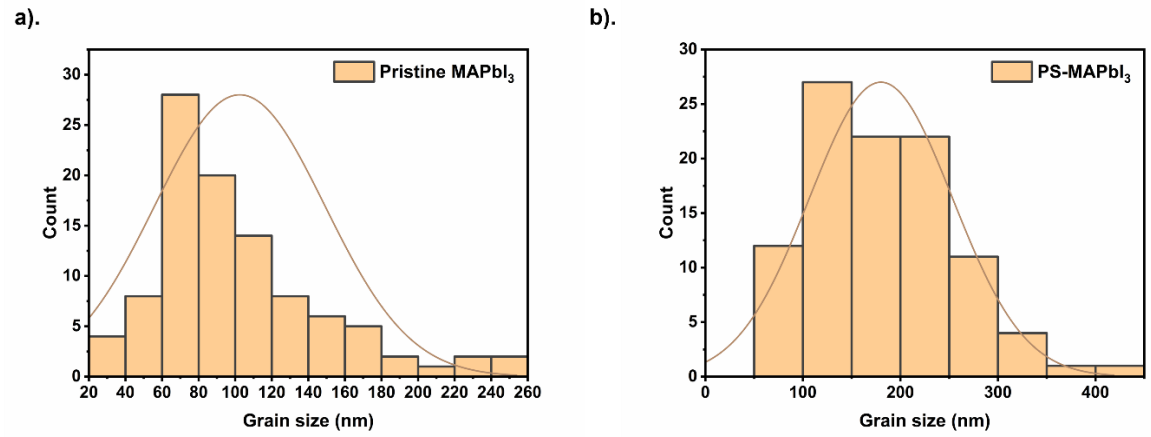

Figure A6.1 Grain size distribution in the room temperature blade coated (s) pristine and (b) PS-$MAPbI_3$ films. The value of average grain size in pristine perovskite film is 103 nm which increases to 180 nm in PS-$MAPbI_3$ film.

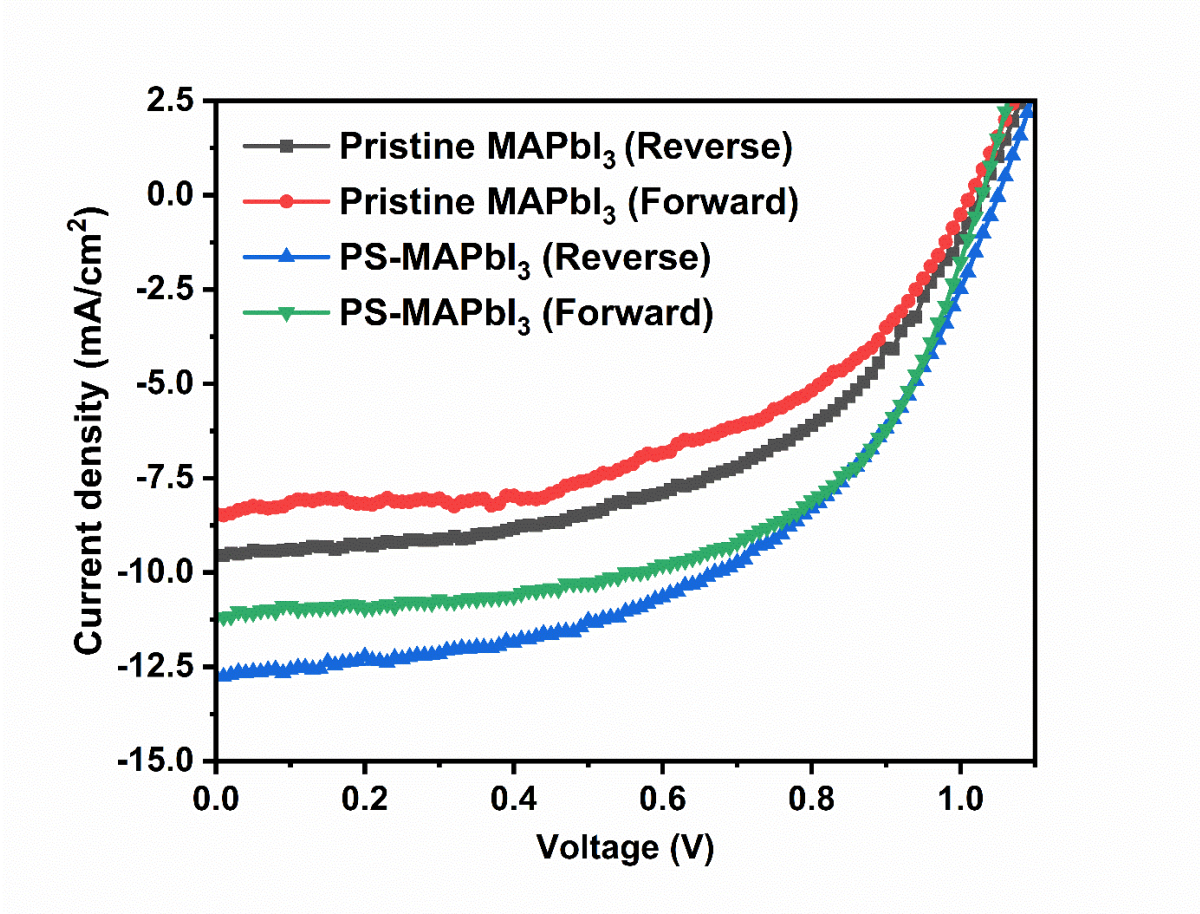

Figure A6.2 *J-V* characteristics of pristine $MAPbI_3$ and PS-$MAPbI_3$ large area solar cells in forward and reverse scanning direction.

Table A6.1 Device parameters for pristine $MAPbI_3$ and 1 wt/v % PS-$MAPbI_3$ devices in reverse and forward scanning directions.

Absorber Material	Scanning direction	Current density (mA/cm^2)	Open circuit voltage (V)	Fill factor	Power conversion efficiency (%)	Hysteresis index
Pristine $MAPbI_3$	Reverse	9.55	1.03	0.49	5.04	0.14
	Forward	8.46	1.01	0.45	4.34	
PS-$MAPbI_3$	Reverse	-12.75	1.05	0.50	6.85	0.04
	Forward	-11.18	1.03	0.54	6.56	